Numerical modelling of rock deformation: conglomerates and mechanical anisotropy

Dissertation

der Mathematisch-Naturwissenschaftlichen Fakultät
der Eberhard Karls Universität Tübingen
zur Erlangung des Grades eines
Doktors der Naturwissenschaften
(Dr. rer. nat.)

vorgelegt von
Hao Ran
aus Liaoning, China

Tübingen
2018

Gedruckt mit Genehmigung der Mathematisch-Naturwissenschaftlichen Fakultät der Eberhard Karls Universität Tübingen.

Tag der mündlichen Qualifikation:	26.07.2018
Dekan:	Prof. Dr. Wolfgang Rosenstiel
1. Berichterstatter:	Prof. Dr. Paul D. Bons
2. Berichterstatter:	Prof. Dr. Genhou Wang

Erklärung

Ich erkläre hiermit, dass ich die zur Promotion eingereichte Arbeit selbständig verfasst, nur die angegebenen Quellen und Hilfsmittel benutzt und wörtlich oder inhaltlich übernommene Stellen als solche gekennzeichnet habe. Ich erkläre, dass die Richtlinien zur Sicherung guter wissenschaftlicher Praxis der Universität Tübingen (Beschluss des Senats vom 25.5.2000) beachtet wurden. Ich versichere an Eides statt, dass diese Angaben wahr sind und dass ich nichts verschwiegen habe. Mir ist bekannt, dass die falsche Abgabe einer Versicherung an Eides statt mit Freiheitsstrafe bis zu drei Jahren oder mit Geldstrafe bestraft wird.

Tübingen, 22 Juni 2018

Abstract

Deformation of conglomerates has received a range of attention in structural geology. Of particular interest is the study of deformation processes, the rock rheology and the tectonic evolution. A range of studies based on field observations, analogue and rock experiments and on numerical modeling have revealed that a variety of parameters, such as the pebble shape, the material properties, the concentration and interaction of pebbles, can affect the deformation of the conglomerate. Despite these efforts it is not yet well understood how the concentration of pebbles and the interaction of neighbouring pebbles affect the deformation of conglomerates. Internal structures of pebbles in deformed conglomerates, such as folds, have been used to recognize the deformation process. Folds in pebbles can either originate in deformation processes of the source rock, prior to the formation of conglomerates, or during the deformation of the conglomerate. It is not clear how and when folds within pebbles develop during conglomerate deformation. Although mechanical anisotropy is a factor that can affect the development of structures, such as folds, only a few studies addressed its influence in numerical modelling. In this study we coupled the Viscoplastic Fast Fourier Transform Method (VPFFT) with the numerical platform ELLE and used it to simulate the deformation of conglomerates, and the development of folds and other structures in an anisotropic matrix.

Our results suggest that pebbles in deformed conglomerates can behave as rigid, deformable and passive inclusions depending on both the viscosity ratio and their concentration. Changing the pebble concentration also changes the transition viscosity ratio between the deformation regimes. The effect of increasing pebble concentration is similar to a decrease of viscosity ratio between pebbles and matrix, and *vice versa*. Clusters of closely spaced pebbles can behave as single objects. A mean R_f-ϕ plot is suggested in order to gain an estimate of the pebble deformation behaviour and the amount of strain in case of permanently stretching pebbles. Deforming layered pebbles may develop internal folds. Internal folding is facilitated by a layering initially at a narrow range of steep angles relative to the shear plane, sufficiently thin internal layers to achieve fold wavelengths smaller than the diameter of the pebble, and a large area fraction of pebbles. It furthermore requires a narrow range of viscosity contrasts between pebble layers and matrix to allow enough strain to develop folds, but still keep the

pebble recognisable as such. Using the mean R_f-ϕ plot, it is suggested that the deformed conglomerates of the Hutuo Group in the Wutai mountains, North China Craton had a viscosity ratio of 5 to 8 in case of a linear rheology (n=1) and of 2 to 5 in case of a power-law rheology (n=3) and underwent a simple shear strain of about six. The difficulty in achieving internal folds within pebbles may explain the scarcity of internally folded BIF-pebbles in deformed conglomerates at the base of the Hutuo Group. Few pebbles with folds do not necessarily indicate a previous deformation event, but may have been formed during deformation of the conglomerate itself. This may change the tectonic interpretation of the rock significantly, as it removes the need for a whole cycle of burial, metamorphism, deformation and exhumation preceding the deposition of the conglomerates.

The results of our numerical simulations indicate that mechanical anisotropy can play a key role on the development of folds, mantled clasts and C' shear bands. Folding in an anisotropic matrix develops in similar-type folds or crenulations that do not decay away from the competent layer. Fold hinges align to form an axial-planar crenulation cleavage. In case of mantled clasts embedded in an anisotropic matrix, rotation of the clast is inhibited and thus a σ-clast forms. C' shear bands forms in all models of anisotropic composite material. Mechanical anisotropy leads to a distinct strain and strain-rate localisation in homogenous, anisotropic materials. The shear rate localizes in narrow shear bands, depending on the magnitude of anisotropy and the stress exponent.

Zusammenfassung

Die Untersuchung der Verformung von Konglomeraten erfährt von Seiten der Strukturgeologie große Aufmerksamkeit. Von Interesse sind die zugrunde liegenden Verformungsprozesse, die Rheologie und die tektonische Entwicklung. Anhand von Geländebeobachtungen, Experimenten an Gesteinen und Gesteinsanalogen sowie mittels numerischer Modellierungen konnten eine Reihe von Untersuchungen bereits zeigen, dass die Verformung von Konglomeraten von einer ganzen Reihe von Parametern kontrolliert wird, z.B. von der Konzentration, den Materialeigenschaften, der Form und der Interaktion der groben Komponenten (Kies). Trotz dieser Untersuchungen ist der Einfluss der Konzentration und der Interaktion benachbarter Grobkomponenten auf die Verformung des Konglomerats bislang noch kaum verstanden. Die Internstrukturen der Grobkomponenten in verformten Konglomeraten, z.B. Falten, wurden hier verwendet, um den Verformungsprozess zu rekonstruieren. Gefaltete Grobkomponenten können bereits vor der Ablagerung und Bildung des Konglomerats verformt worden sein oder während der Verformung des Konglomerates selbst. Es ist unklar, wie die interne Verfaltung der Kieskomponente mit der Verformung des Gesamtgesteins gekoppelt ist. Obwohl mechanische Anisotropie ein Parameter ist, der die Entwicklung von Internstrukturen beeinflussen kann, ist ihr Einfluss nur in wenigen Studien numerisch modelliert worden. Wir koppeln in dieser Studie die 'Viscoplastic Fast Fourier Transform Method' (VPFFT) mit der numerischen Plattform ELLE, um die Deformation von groben Konglomerat-Komponenten inklusive der Entwicklung von Falten und anderer Strukturen in einer anisotropen Matrix zu modellieren.

Unsere In deformierten Konglomeraten können Kiese entweder als starre, als deformierbare oder als passive Inklusionen auftreten, entsprechend des Viskositätskontrastes und der Konzentration grober Komponenten. Mit der Konzentration der Kies-Komponente ändert sich auch der Viskositäts-Kontrast, der den Übergang zwischen den Verformungs-Regimen bestimmt. Eine höhere Konzentration von Kies-Komponenten hat die gleich Wirkung wie eine Abnahme des Viskositäts-Kontrastes zwischen Grobklasten und Matrix, und umgekehrt. Gruppen eng benachbarter grober Komponenten können das gleiche Verhalten aufweisen wie einzelne Objekte. R_f-ϕ Plots haben sich als nützlich erwiesen, um das Deformations-Verhalten

und den Betrag der Verformung im Fall grober Konglomerat-Komponenten unter permanenter Dehnung abzuschätzen. Deformierte geschichtete Grobkomponenten können intern verfaltet werden. Diese interne Verfaltung wird begünstigt wenn (1) Schichtung und Scherfläche innerhalb eines kleinen Bereichs großer Winkel zueinander orientiert sind, (2) die interne Schichtung fein genug ist um Falten-Wellenlängen zu erzielen die kleiner sind als der Klast selbst, und (3) eine hoher Anteil der Kies-Komponente. Darüber hinaus muss sich der Viskositätskontrast zwischen Matrix und Lagen grober Klasten innerhalb einer engen Bandbreite bewegen, um einerseits genügend Verformung zuzulassen um Falten zu entwickeln, aber zugleich auch einzelne Klasten als solche erkennbar zu lassen. Der mittlere R_f-ϕ Plot deformierter Konglomerate der Hutuo Gruppe in den Wutai Bergen (Nord-China Kraton) legt für eine lineare Rheologie (n=1) einen Viskositätskontrast von 5-8 nahe, und einen Viskositätskontrast von 2-5 für eine nicht-lineare Rheologie (n=3). Die Scherverformung beträgt etwa 6. Die große Zahl an Vorbedingungen, die für die interne Verfaltung der Grobklasten notwendig sind, erklärt die Seltenheit intern verfalteter BIF-Kiese in verformten Konglomeraten an der Basis der Hutuo Gruppe. Einige wenige gefaltete Kiese müssen nicht notwendig auf ein vorhergehendes Deformationsereignis hinweisen, sondern können während der Deformation des Konglomerates selbst entstanden sein.

Unsere numerischen Modellierungen zeigen, dass das Vorhandensein einer mechanischen Anisotropie eine Schlüsselrolle in der Entwicklung von Falten, ummantelten Porphyoklasten und C' Scherbändern spielen kann. Faltung in einer anisotropen Matrix resultiert in ähnlichen Falten oder Krenulation, die mit zunehmender Distanz von der kompetenten Lage nicht abnehmen. Faltenscharniere richten sich so aus, das sie ein Achsparalles Krenulationsgefüge bilden. Im Falle eines ummantelten Klasten in einer anisotropen Matrix wird die Rotation des Klasten nun verhindert, so dass sich ein σ-Klast formt. C'-Bänder bilden sich in allen Modellen, die auf anisotropen, Kompositmaterialien basieren. Mechanische Anisotropie führt zu deutlicher Lokalisierung der Verformung und der Verformungsrate in homogenen, anisotropen Materialien. Lokalisierung der Scherverformungsrate in dünnen Scherbändern tritt auf, abhängig von der Stärke der Anisotropie und dem Spannungs-Exponenten (n).

Acknowledgements

A lot of heartfelt thanks are given to everyone who offers me a wonderful time during three years of my PhD career. I would like to give many thanks to my supervisor, Prof. Dr. Paul D. Bons, who not only supervises my PhD research but also helps me in life. He guides me to extend a new research field, numerical modelling, and always offers me his professional supervision, warm help and kindly encouragement. I benefit from his scientific knowledge, experience, as well as attitude. I also would like to thank my second supervisor, Prof. Genhou Wang for his 9-year supervision including my undergraduate and graduate careers. I learn a range of knowledge for structural geology, ability and experience of fieldwork from him. His encouragement pushes me forwards step by step.

I would like to thank Associate Prof. Weijie Zhang, Prof. Changhou Zhang, Prof. Danping Yan, Associate Prof. Weihua Sun, Prof. Guoli Yuan and Dr. Xiao Liang, who gain me fundamental knowledge of geology and give me a lot of help. I also would like to give many thanks to the currently or former members in Prof. Wang's workgroup at China University of Geosciences, Beijing.

Many thanks to my colleagues in structural geology workgroup and my friends in Tuebingen: Florian Steinbach who gives me first lesson of numerical modelling, Tamara de Riess, Till Sachau, Melanie Finch and Catherin Bauer. I really enjoy everything in structural geology workgroup. Many thanks also to Albert Griera, Enrique Gomez-Rivas and Maria-Gema Llorens for their help on my studies of numerical modelling.

I would like to give special thanks to my parents, who bring me up and always support me. I love you!

I have a wonderful experience of PhD and the thesis including my 3-year work, because of all of you! Thank you so much!

Contents

Chapter 1

Introduction

1. Introduction

Structural geology is the subject of geology that mainly focuses on the deformation of rocks in the lithosphere of the Earth or other planets (e.g., Moon and Mars). Understanding rock deformation is one of the keys to gain knowledge of processes of the Earth (from the surface to great depth), such as mountain formation and uplift, plate movements and earthquakes (Ramsay and Huber, 1983; Twiss and Moores, 1992; Davis et al., 2011; Fossen, 2016). It is well known that there are two end-member types of rock-deformation: elastic-brittle and viscoplastic or ductile deformation, but with transitions between them in nature (Ramsay and Huber, 1983; Twiss and Moores, 1992; Passchier and Trouw, 2005; Fossen, 2016). Elastic-brittle deformation occurs at a shallow level of earth's crust where the temperature and pressure are relative low. It leads to the formation of fractures in rocks with minor distortion in between (Ramsay and Huber, 1987; Twiss and Moores, 1992; Fossen, 2016). Ductile deformation occurs commonly at a moderate to deep levels with high temperature and pressure. With ductile deformation or viscous flow strain rate depends on stress. Most rocks exhibit a linear (Newtonian) or power-law relationship (with the stress exponent >1) between strain rate and stress (Carter and Tsenn, 1987; Kirby and Kronenberg, 1987). Such ductile deformation is modelled in this thesis. A large range of structures under viscous deformation are currently preserved in the outcrops, such as folds, porphyroclasts/porphyroblasts and shear zones.

Structural geologists aim to identify the material properties, boundary conditions, deformation processes and tectonic evolution of geological bodies through the studies of ductile

deformation structures at different scales, from the crystal lattice of individual grains to whole continents. Deformed objects such as layers and inclusions, together with their matrix, are widely used to gain insight into deformation processes and rheology. Folds formed by deformed layered structures have been addressed by a range of studies including field observations, rock and analogue deformation experiments, analytical models, as well as numerical simulations (e.g., Biot, 1961; and review of Hudleston and Treagus, 2010). Through these studies we have gained knowledge of deformation histories, such as finite strain, and lithological properties, such as competence contrasts and rheological behaviour (linear or power-law rheology). Deformed inclusions are another important structure in structural geology, such as porphyroclasts/porphyroblasts in deformed metamorphic rocks and pebbles in deformed conglomerates (e.g., Ramsay and Huber, 1987; Passchier and Trouw, 2005). They are usually simplified as a system of inclusion(s) embedded in a matrix. A range of studies have dealt with the rotation and distortion of inclusion(s), the flow pattern of the matrix and effects of rheology (e.g., Flinn, 1956; Eshelby, 1957; Ramsay, 1967; Dunnet, 1969; Bilby et al., 1975; Fry, 1979; Lisle et al., 1983; Treagus and Treagus, 2002; Passchier and Trouw, 2005; Jiang, 2007a,b; and reviews of Marques et al., 2014). Mantled porphyroclasts, including σ- and δ-clasts, form a special, more complex group of inclusions. There is an ongoing debate how σ- and δ-clasts develop (e.g., Bell et al., 1992; Passchier et al., 1992; ten Brink and Passchier, 1995; Bons et al., 1997; Griera et al., 2011; 2013; Ran et al., 2018b, *Chapter 4*). Of the many ductile deformation structures, this study focuses on the deformation of conglomerates.

2. Deformed Conglomerates

Deformed conglomerates have received particular attention in structural geology for studies on strain analysis, deformation process, rheology and tectonic evolution (e.g., Flinn, 1956; Ramsay, 1967; Dunnet, 1969; Fry, 1979; Lisle et al., 1983; Treagus and Treagus, 2002; Passchier and Trouw, 2005). Deformed conglomerates are classical indicators of finite strain, stress orientation, vorticity, and viscosity contrast between pebbles and their matrix (e.g.,

Ramsay, 1967; Lisle et al., 1985; Freeman and Lisle, 1987; Czeck and Hudleston, 2003).

2.1. Finite strain

One of the most widely used methods is the R_f-ϕ method that makes use of aspect ratios (R_f) and long axis orientations (ϕ) of pebbles for the estimation of strain (Ramsay, 1967; Dunnet, 1969; Lisle, 1985). The very basic assumption of this method is passive deformation of pebbles. The assumption is that initially elliptical pebbles with random distribution of their long-axis orientations deform passively, embedded in a matrix with an identical viscosity. It provides a very simple method, only using the measurements of aspect ratios and orientations of pebbles, to determine the bulk strain in planer sections of natural deformed conglomerates. Various ways to determine the value of the ellipticity of the finite strain ellipse (length of long axis divided by that of short axis, R_s) from the R_f-ϕ plot have been proposed, including the calculation of the geometric mean of the minimum and maximum values of R_f. Lisle (1977) systemically compared the arithmetic, geometric and harmonic means of R_f with R_s and showed how they differ from the R_s. He proposed that the harmonic mean of R_f is closest to R_s. However, the estimation based on the R_f-ϕ method ignores the viscosity contrast between pebble and matrix which occurs very commonly in natural conglomerates. The R_f-ϕ method is ideally applied to matrix-supported conglomerates where pebbles do not interact with their neighbours. It is obviously that the bulk strain is usually underestimated as pebbles are more competent than the matrix in most natural cases (Treagus and Treagus, 2002). However, the R_f-ϕ method can provide a good estimation of pebble strain, especially if all pebbles are of the same rock type, rather than the bulk strain (Treagus and Treagus, 2002).

Another well-accepted method for strain estimation is the Fry method (or its modifications) that is widely used to evaluate the bulk finite strain (Fry, 1979; Erslev and Ge, 1990; McNaught, 2002; Treagus and Treagus, 2002; and reviews of Kumar et al., 2014). The strain ellipse is displayed by the central void in scatter plots of center-to-center distances in a two-dimensional section. The Fry method can ideally provide a good strain ellipse when

pebbles have similar sizes and the deformation is homogeneous. Otherwise, the central void is diffuse and thus leads to an uncertain strain ellipse. Some studies have pointed out that the bulk strain evaluated by Fry method (or its modifications) is not completely reliable considering the interactions between pebbles and the effect of brittle-ductile deformation (Czeck et al., 2009), but it is one of the most widely used methods to estimate the bulk strain in natural conglomerates (Treagus and Treagus, 2002; Czeck et al., 2009).

2.2. Rheology—viscosity contrast

Deformed conglomerates can provide a range of rheological information, especially on viscosity contrast. Viscosity contrast is quantified as the ratio of inclusion (pebble) and matrix viscosity. In linear (Newtonian) rheology, the viscosity ratio is a constant. However, it is not a constant and depends on strain rate in power-law rheology. An effective viscosity ratio is therefore sometimes used (e.g., Treagus, 1999). It is commonly used for the viscosity contrast between pebble and matrix in deformed natural conglomerates (e.g., Treagus, 1999; Treagus and Treagus, 2002; Czeck et al., 2009). In fact it is more accepted to use the viscosity ratio of pebble to whole rock instead of to matrix in natural conglomerates since it is easier to estimate the bulk finite strain rather than the matrix strain.

Eshelby (1957; 1959) propose a theory for the motion of deformable ellipsoidal inclusions embedded in an infinite elastic matrix, which assumes that both inclusions and matrix are isotropic but may have different elastic contrasts. It is also pointed out that the general theory can be applied to the viscous deformation of inclusion embedded in the matrix with a different viscosity (Eshelby, 1957; 1959).

Gay (1968) analyses the deformation of circularly or elliptically viscous inclusions embedded in a Newtonian fluid (linear viscous) matrix under pure and simple shear, considering the viscosity ratio between inclusions and matrix. He points out that the viscosity ratio is an important factor that affects the inclusion deformation. The relationship between single inclusion deformation and viscosity ratio under pure shear given by Gay (1968) is:

$$\ln R_f = \ln R_i + \frac{5 \ln R_s}{2R\eta+3}, \quad (1)$$

where R_f, R_i and R_s is the aspect ratio of deformed inclusion, initially elliptical inclusion and strain ellipse, respectively. The equation can be applied to simple-shear deformation, which is considered as a pure shear combined with a rotation. He also considers that the inclusion concentration can affect the bulk rheology of inclusion-matrix system, and thus affect the individual inclusion deformation. Another equation considering the influence of inclusion concentration by Gay (1968) is

$$R\eta_{bulk} = R\eta \Big/ \left[1 + \frac{5AC(R\eta-1)}{2R\eta+3}\right], \quad (2)$$

where $R\eta_{bulk}$ is the viscosity ratio between inclusions and bulk system. *A* is a factor related to the interaction between inclusions. The values of *A* at different pebble concentrations (*C=volume(pebbles)/total volume*) are used from Happel (1957). It should be noted that Gay's (1968) equation is based on Lamb's formulation for spherical surfaces. However, the equation mixes spherical and elliptical coordinates to obtain a solution. It is not considered strictly correct, but obtains a good first approximation of the viscous deformation of an inclusion-matrix system with viscosity contrasts (Bilby et al., 1975; Bilby and Kolbuszewski, 1977; Treagus and Treagus, 2001; 2002; Mulchrone and Walsh, 2006).

Bilby et al. (1975) and Bilby and Kolbuszewski (1977) extend Eshelby's (1957) theory and derive a non-linear expression for the viscous deformation of inclusion-matrix system with viscosity contrast. It is assumed that an initial circular inclusion deforms in an infinite matrix, in the linear viscous rheology under pure shear. There is no slip at the interface between inclusion and matrix. The equation of Bilby et al. (1975) and Bilby and Kolbuszewski (1977) is

$$\ln R_s = \ln R_f + \frac{(R\eta-1)(R_f-1)}{R_f+1}. \quad (3)$$

Both of the equations (Eqs. (1) and (3)) for the deformation of single inclusion discussed above can provide a good prediction for the relation between the bulk finite strain and inclusion strain at different viscosity contrast. It is noted that they have similar solutions for the deformation of competent inclusions (i.e., $R\eta > 1$) (Gay, 1976; Treagus and Treagus, 2002; Fig. 1). It is common that pebbles are more competent than the matrix in natural conglomerates. Both equations give comparable predictions of the bulk strain for a given viscosity ratio. Alternatively, they can be used to estimate the relative viscosity ratio between inclusion and matrix when we know the bulk strain and inclusion strain. For an inclusion-matrix system with an initially circular inclusion, we can rewrite the Eqs. (1) and (3) respectively, in terms of viscosity ratio,

$$R\eta = \frac{5\ln R_s - 3\ln R_f}{2\ln R_f}, \text{ (4a)}$$

and $$R\eta = \frac{(\ln R_s - \ln R_f)(R_f+1)}{R_f-1} + 1. \text{ (4b)}$$

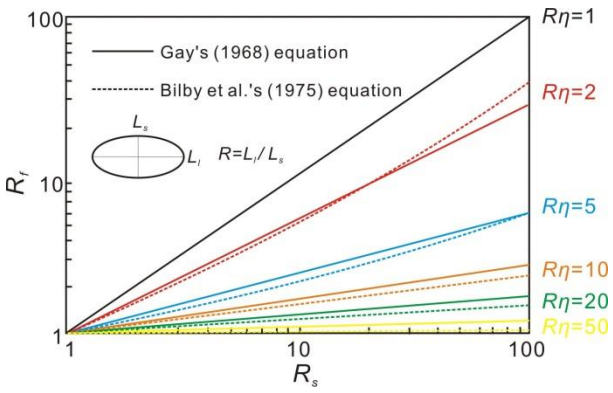

Fig. 1. Comparison between Gay's (1968) equation (solid lines) and Bilby et al. (1975) equation (dashed lines) at viscosity ratios of 2, 5, 10, 20 and 50.They shows similar predicted relationships between R_f and R_s.

A range of studies have dealt with the estimation of viscosity ratio between pebble and matrix in natural deformed conglomerates using either Gay's (1968) or Bilby et al.'s (1975) equation (e.g., Treagus and Treagus, 2002; Vitale and Mazzoli, 2005; Czeck et al., 2009). The R_f-ϕ

method is used to evaluate the finite strain of a particular lithology (i.e., same rock-type pebbles), and the Fry method or the weighted mean of finite strains of different rock types is used to evaluate the matrix (whole rock) finite strain. The viscosity ratio between pebbles and matrix is calculated by pebble strain and matrix or bulk strain, using either Gay's (1968) or Bilby et al.'s (1975) equation. The calculated viscosity ratios among different rock types are found to have a limited range (mostly less than 12; e.g., Lisle et al., 1983; Treagus and Treagus, 2002; Czeck et al., 2009 and references therein). Although minerals are usually assumed to deform with a power-law rheology (by dislocation creep; Carter and Tsenn, 1987; Kirby and Kronenberg, 1987; Hirth and Tullis, 1992), the behaviour of common rock types in natural conglomerates has been approximated with a linear viscous rheology at the outcrop scale (Treagus, 1999; Treagus and Treagus, 2002; Czeck et al., 2009). It has been noted that an increase in pebble concentration can decrease the calculated viscosity ratio in natural conglomerates (Vitale and Mazzoli, 2005), in line with the theoretical analysis of Gay (1968).

2.3. Numerical modelling studies

Numerical modelling provides a good method to investigate and understand the deformation mechanism and rheology of conglomerates in linear and power-law rheology. In numerical models, conglomerates are idealised as polyphase systems formed by inclusion(s) embedded in a (weaker) matrix. A range of numerical modelling studies reveal that there are several key factors that control the deformation (See Ran et al., 2018a, *Chapter 2*):

(1) Initial shape of the inclusion(s) (e.g., Treagus and Lan, 2000; 2004; Treagus, 2002). The distortion of an elliptical or square inclusion is more than that of an initially circular one at a given viscosity contrast to matrix.

(2) Material properties, in particular the viscosity contrast between inclusion and matrix (Treagus and Treagus, 2001; Mandal et al., 2003; Takeda and Griera, 2006; Griera et al., 2013), the matrix anisotropy (Treagus, 2003; Fletcher, 2004; Griera et al., 2011; 2013; Qu et al., 2016) and the linear or power-law rheology (Mancktelow, 2002; 2011; Jiang, 2013;

Qu et al., 2016). An increase in viscosity contrast of inclusion to matrix reduces the distortion of inclusion, but enhances its rotation. The influence of power-law rheology is similar to an increase of linear viscosity contrast. Mechanical anisotropy in matrix slows down the inclusion rotation.

(3) Behaviour of the interface between inclusion and matrix (e.g., Johnson et al., 2009; and reviews of Marques et al., 2014). The slipping on the interface between inclusion and matrix reduces inclusion rotation, and even make it rotate backwards.

(4) Distribution of inclusions (Treagus, 2002; Takeda and Griera, 2006) and the interaction between them (Ildefonse et al., 1992a,b; Tikoff and Teyssier, 1994; Marques and Bose, 2004; Mandal et al., 2005; Jessell et al., 2009; Mancktelow, 2011). An increase in inclusion concentration and interactions between them is similar to a decrease of viscosity contrast in case of an isolated inclusion. The interactions reduce and can even stop inclusion rotation. Clusters can form by several inclusions and behave as a single object with the interactions (Blumenfeld and Bouchez, 1988; Tikoff and Teyssier, 1994; Jessell et al., 2009).

However, most of the studies discussed above deal with the deformation of isolated inclusions and thus ignore the influence of inclusion distribution and interactions between neighbouring inclusions. Natural conglomerates are composed of multiple pebbles, usually resulting in interactions between neighbouring ones, especially in clast-supported conglomerates. A few studies have recognised that the deformation behaviour of inclusions and the bulk viscosity of the system are significantly affected by the concentration inclusions and their interaction (Gay, 1968; Bons and Cox, 1994; Mandal et al., 2003; 2005; Vitale and Mazzoli, 2005; Jessell et al., 2009; Mancktelow, 2011; Dabrowski et al., 2012; Marques et al., 2014).

3. Mechanical anisotropy

Structure geologist have recognized the significant influence of anisotropy on the

development of structures and rheology (e.g., Etchecopar, 1977; Lister et al., 1978; Treagus, 2003; Fletcher, 2004; 2009; Mandal et al., 2005; Griera et al., 2011; 2013; Bons et al., 2016; Ran et al., 2018b, *Chapter 4*). In nature, anisotropy can be "intrinsic" and caused by aligned minerals or lattice preferred orientations (LPO) or "composite" when formed by alignment of different layered rock types, typically bedding. Anisotropy leads to a range of structures at multiple scales, from crystallographic lattice preferred orientations (LPO), folds and boudins, to continental structures (e.g., Etchecopar, 1977; Lister et al., 1978; Bercovici 2014).

A number of studies have been dealt with the influence of anisotropy on folding and clast rotation (e.g., Treagus et al., 2003; Fletcher et al., 2004; 2009; Kocher et al., 2006; Griera et al., 2011; 2013; Ran et al., 2018b, *Chapter 4*). Anisotropy has a first-order effect on growth rate and wavelength (Kocher et al., 2006). Similar-type folds or crenulation cleavages can form in anisotropic matrix while the single competent layer is folded (Kocher et al., 2006; Ran et al., 2018b, *Chapter 4*). The rotation of rigid inclusion is related to the degree of matrix anisotropy. An increase in matrix anisotropy reduces the inclusion rotation rate (e.g., Fletcher et al., 2004; 2009; Griera et al., 2011; 2013). It allows us to consider the potential influence of anisotropy on the development of σ-/δ-clast. Although it is already suggested that anisotropy of the matrix would inhibit rotation, leading to the formation of σ-clasts (Bons et al., 1997), this effect has not been investigated in detail yet (Fig. 2; see Ran et al., 2018b, *Chapter 4*).

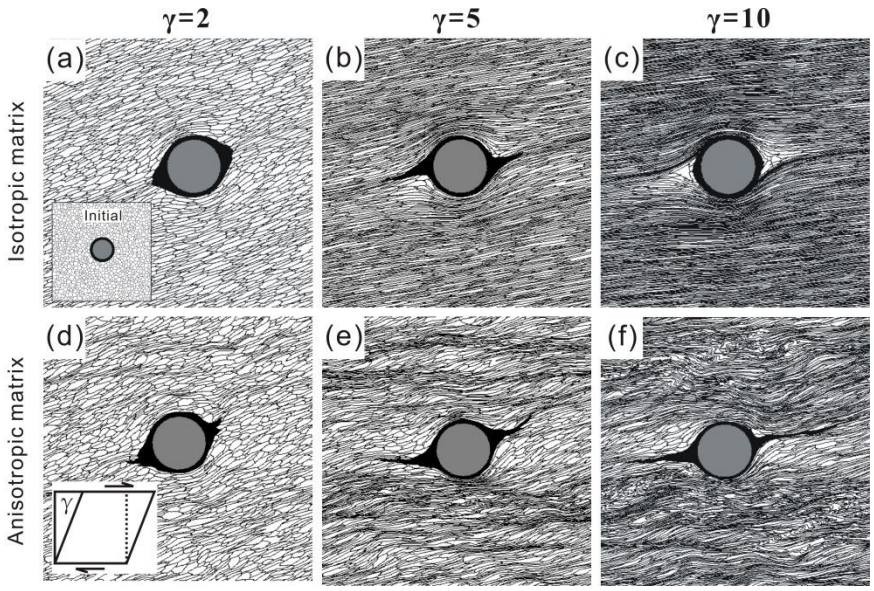

Fig. 2. Mantled clasts embedded in isotropic **(a-c)** and anisotropic **(d-f)** matrix in simple-shear (top-to-right) strain of two (a,d), five (b,e) and ten (c,f). An anisotropic matrix results in strain localisation, leading to the development of σ-clast, instead of δ-clasts that develop in the isotropic matrix. Same initial structure (inset in a) is used in both simulations. More details see Ran et al. (2018b), *Chapter 4*.

Anisotropy that leads to strain softening is one of mechanisms of shear localisation. A lattice-preferred orientation (LPO) or shape-preferred orientation (SPO) as a result of anisotropy can soften the rocks, furthermore leading to shear localisation (see reviews in de Riese et al. (submmited, *Chapter 5*). It is also confirmed by the observation of numerical models of Griera et al. (2011) and Ran et al. (2018b, *Chapter 4*). However, few numerical studies on shear localisation included the effect of anisotropy, especially that of intrinsic anisotropy.

There are two commonly used ways to simulate the deformation with anisotropy: (1) two-phase composites (e.g., layered structures) with alternating viscosity (Fig. 3a; e.g., Treagus, 2003; Fletcher, 2004; 2009; Dabrowski and Schmid, 2011; Griera et al., 2013) and (2) intrinsic anisotropy defined by orientation-dependent mechanical properties, e.g. related to slip systems (Fig. 3b; e.g., Griera et al., 2011; 2013; Bons et al., 2016; Ran et al., 2018b, *Chapter 4*; de Riese et al., submitted, *Chapter 5*). However, the anisotropy modelled by composites is limited by the scale, since the scale of layering or other structures is required to be small relative to the scale of deformation. Alternatively, intrinsic anisotropy is developed at all scales, and thus it can, at least theoretically, be applied to simulate the deformation at all scales. Deformation structures, such as folds, modelled by the two descriptions of anisotropy may appear similar (Fig. 3 c,d), but the distributions of strain rate and stress are quite different in two models (Fig. 3e-h).

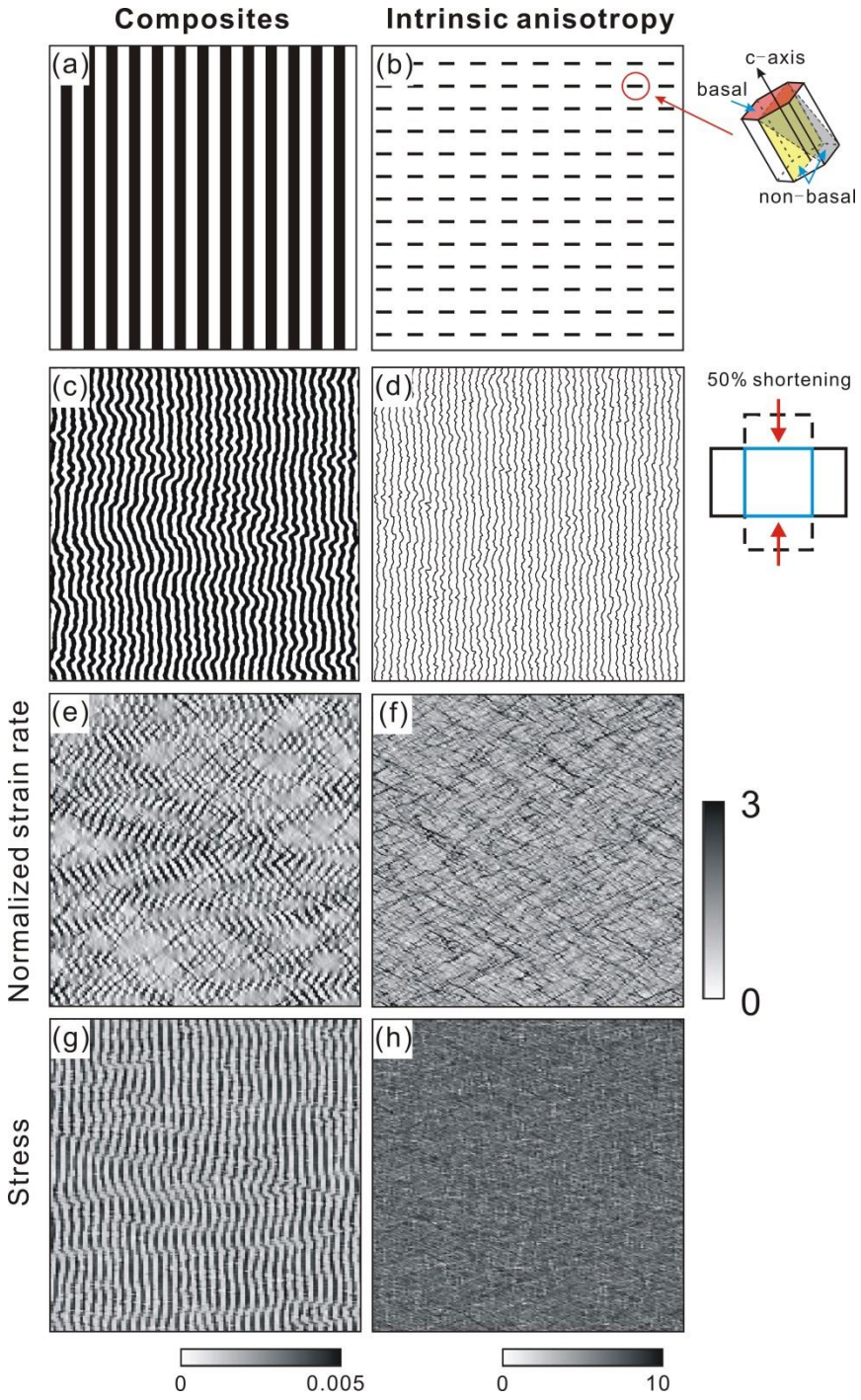

Fig. 3. Two ways to simulate anisotropy in numerical models: **(a)** two-phase layered composite with alternating viscosity and **(b)** intrinsic anisotropy defined by different activities on slip systems. The patterns of folds are similar in composite **(c)** and intrinsic **(d)** anisotropy models, under 50% vertical shortening. Their normalized strain rate and stress, however, show different patterns in composite **(e,g)** and intrinsic **(f,h)** anisotropy models. Intrinsic anisotropy model is unpublished work from de Riese.

4. Motivations of the thesis

This thesis is motivated by ongoing work on deformed conglomerates of the Hutuo Group in the Wutai Mountains, China. The deformed conglomerates at the base of the Hutuo Group provide key information to explain the deformation history and indicate the tectonic evolution of the North China Craton. The North China Craton consists of two continental blocks, named the Eastern and Western Blocks (Fig. 4a). The two blocks collided in the Paleo-proterozoic and formed a large orogenic belt between them: the Trans-North China Orogen (TNCO) (see reviews of Zhao and Zhai, 2013). However, there are ongoing debates of the timing and tectonic processes involved in the amalgamation of the two blocks (e.g., Zhao et al., 2001; Li and Kusky, 2007). The Hutuo Group located in the TNCO is divided into three subgroups: the Doucun, Dongye and Guojiazhai subgroups from base to top and consists of subgreenschist-facies to greenschist-facies sedimentary rocks and minor volcanic rocks (e.g., Bai, 1986). The Hutuo Group overlies the Wutai Group, which consists of metamagmatites and metasedimentary rocks from subgreenschist-facies to amphibolite-facies, intercalated with banded-iron formation (BIF) units. The age of the Wutai Group is estimated at ~2.5 Ga (see reviews of Zhao and Zhai, 2013), but the age of the Hutuo Group remains uncertain (~2.5-2.2 Ga or ~2.1-1.8 Ga) (Kusky and Li, 2003; Wilde et al., 2004; Li and Kusky, 2007; Liu et al., 2011). Pebbles in the Hutuo Group conglomerates consist mostly of Wutai Group lithologies (BIF pebbles dominating in the Yangjiaogou area) (Fig. 4b,d-g). This indicates that erosion of the Wutai Group during deposition of the Hutuo Group and an unconformity between the two groups. Both groups experienced at least one distinct deformation phase (D_1 of Zhang et al., 2012), resulting in a strong foliation in the conglomerate matrix that wraps around stretched and rotated pebbles (Fig. 4c-e).

Deformation (Kusky and Li, 2003; Trap et al., 2012; Zhang et al., 2012) and sedimentary setting (foreland basin or intracontinental basin) (Kusky and Li, 2003; Wilde et al., 2004; Liu et al., 2011; Zhang et al., 2012) of the Hutuo Group are, however, still not understood well. Most pebbles with internal layering show no folding of that layering, even though the

conglomerate is deformed. However, some BIF-pebbles show folding of the internal layering, especially in the Yangjiaogou area (Fig. 4b,f-g). Although the deformed conglomerates have been interpreted as basal conglomerates, which unconformably overlay the lower Wutai Group and Neoarchean granitoids, it is not clear whether the deformation structures of pebbles formed before or after the deposition of the Hutuo Group (Fig. 5a; e.g., Bai, 1986; Zhang et al., 2012; Du et al., 2012). If the pebbles were deformed before deposition, there was a major tectonic event between formation of the Wutai and Hutuo groups (Fig. 5b). Alternatively, if the pebbles were deformed after their deposition, the Hutuo Group may be older and the underlying Wutai Group would not have undergone a full cycle of burial, deformation and erosion (Fig. 5c). It leads to us consider the basic questions of the conglomerate deformation: (1) How do pebbles deform in conglomerates with multiple pebbles? (2) Can deformed conglomerates with a viscosity contrast between pebbles and matrix be used to quantitatively estimate the finite strain and understand the rheology? And (3) When and how can folding within pebbles develop and can folding be used to infer the tectonic evolution. Questions (1) and (2) lead to the studies of *Chapter 2*, and question (3) leads to the studies of *Chapter 3*.

Furthermore, apart from the deformation of conglomerates, folding within pebbles also leads us to consider another question: the mechanism of folding. As mentioned above, a number of studies deal with this issue (e.g., Biot, 1961; and reviews of Hudleston and Treagus, 2010). However, to my knowledge, few studies address the effects of mechanical anisotropy in a matrix. Considering the significant influence of mechanical anisotropy on the development of structures, it is necessary to simulate folding, as well as the development of other structures, in mechanical anisotropic materials. This leads to the studies of *Chapter 4* and *Chapter 5*.

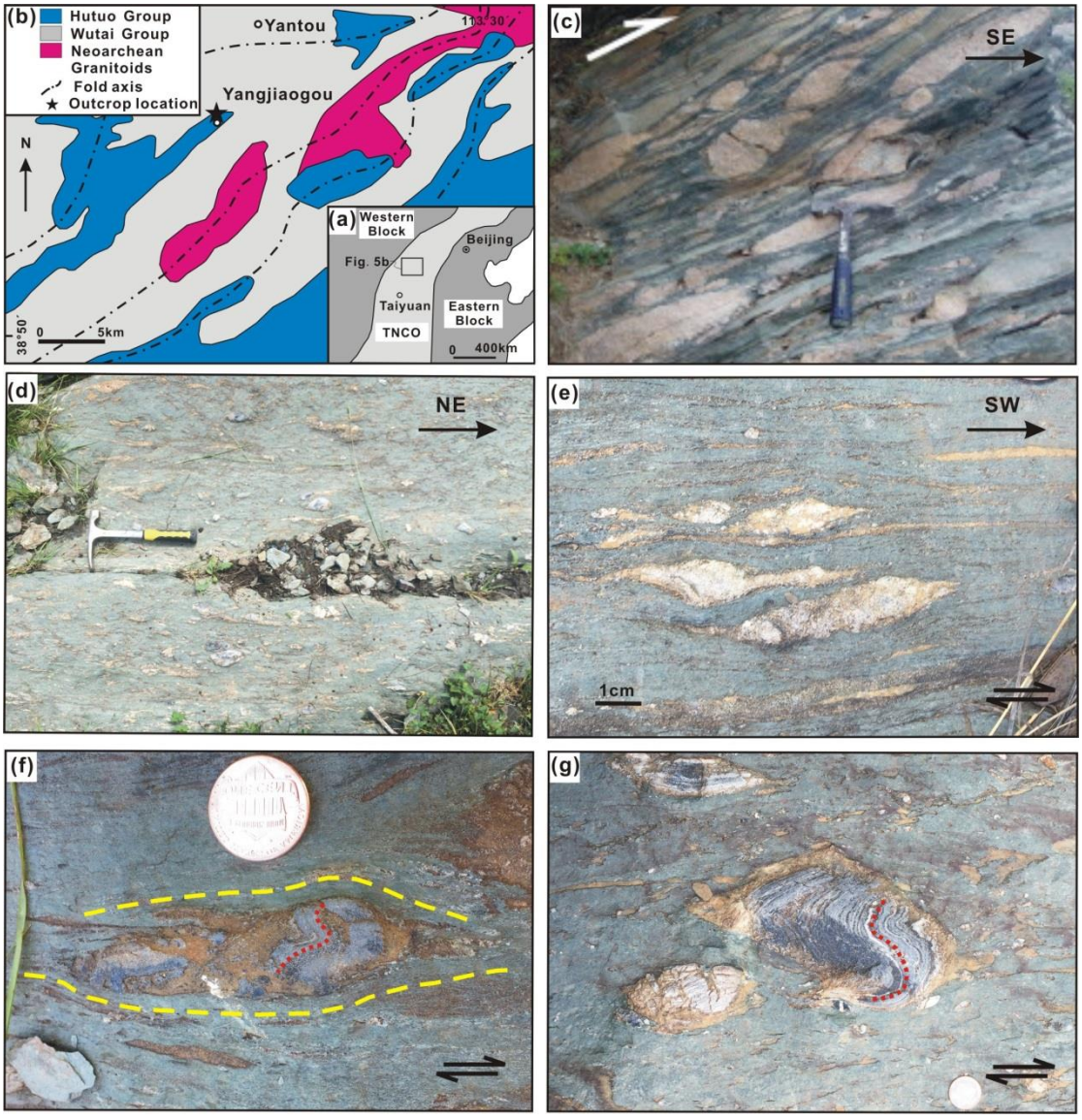

Fig. 4. Deformed conglomerates in the Wutai Mountains, North China Craton. **(a)** Tectonic subdivision of the North China Craton (modified after Zhao et al., 2005). TNCO-Trans-North China Orogen. **(b)** Simplified geological map of the Yangjiaogou area and location of the outcrop with deformed conglomerates. **(c)** Elongated clasts and stretched pebbles in deformed conglomerates of the Hutuo Group (from Zhang et al., 2012). **(d-g)** Deformed conglomerates with BIFs pebbles in the Yangjiaogou area. Folding within BIFs pebbles can identified in (f) and (g). The diameter of the 1 dollar-cent coin is 19mm.

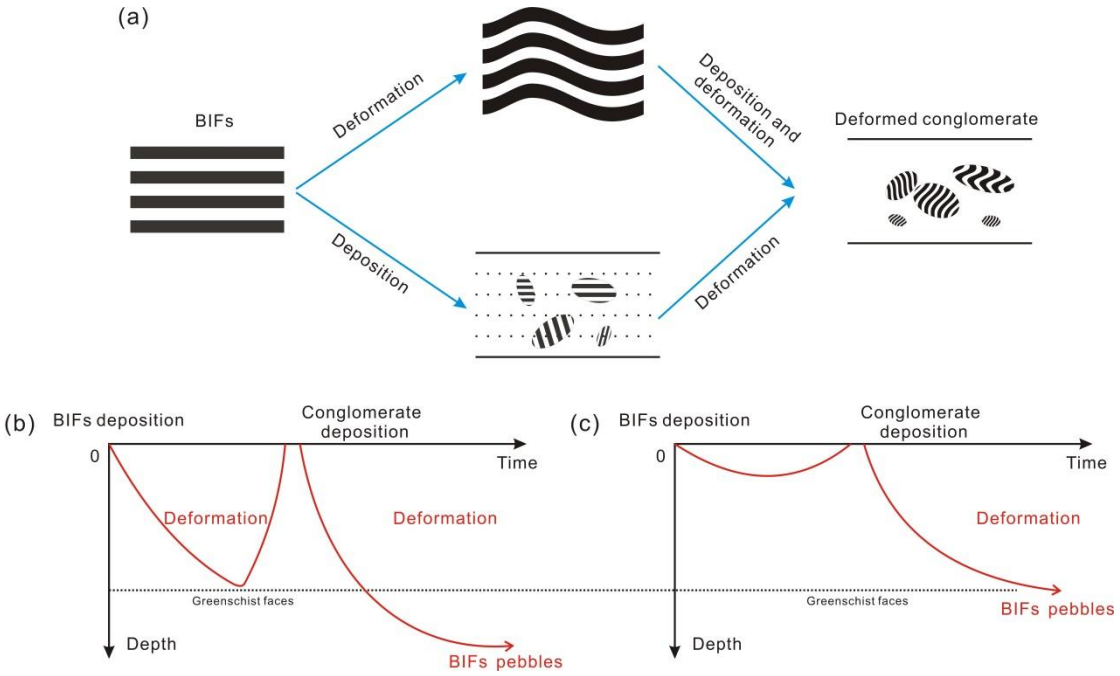

Fig. 5. Two alternative deformation processes of deformed conglomerates in the Wutai Mountains, North China Craton. **(a)** BIFs underwent deformation (folded) before or after deposition of conglomerates. **(b)** BIFs underwent viscous deformation (folded), and then formed the conglomerates. Finally, conglomerates with folded BIFs pebbles underwent deformation and formed deformed conglomerates. There is a major tectonic event between formation of BIFs from the Wutai Group and conglomerates from the Hutuo Group. **(c)** BIFs pebbles were folded with the conglomerate deformation, after its deposition. There is no major tectonic event before the formation of conglomerates from the Hutuo Group. Solid red lines show the evolution of BIFs (pebbles) in (b) and (c).

5. Numerical modelling methods—VPFFT+ELLE approach

The viscoplastic fast Fourier transform method (a full-field approach) (VPFFT; Lebensohn, 2001; Lebensohn et al., 2009; 2011) has been proposed in recent years and applied to a range of deformation simulations, including folding (Ran et al., 2018b, *Chapter 4*), development of porphyroclasts/porphyroblasts and mantled clasts (Griera et al., 2011; 2013; Ran et al., 2018b, *Chaper 4*), halite deformation (Gomez-Rivas et al., 2017) and polar ice and ice-air aggregate deformation (Bons et al., 2016; Llorens et al., 2016a,b; 2017; Jansen et al., 2016; Steinbach et

al., 2016; 2017). In general, the VPFFT approach has a better numerical performance than most FEM (Prakash and Lebensohn, 2009; Roters et al., 2011). For the same geometry and resolution, the FEM computation time tends to exceed that of the VPFFT. The VPFFT allows us to achieve a high finite strain of ≥10 and model the deformation of polycrystalline aggregates with intrinsic anisotropy in linear and power-law viscous rheology. The intrinsic anisotropy can be modelled by defining different critical resolved shear stress (CRSS) on basal and non-basal slip planes. It allows us to investigate the influence of mechanical anisotropy on the development of structures, which is ignored in previous studies as mentioned above. Therefore, the VPFFT approach is used to investigate the conglomerate deformation and the effect of anisotropy in the thesis.

5.1. The ELLE numerical modelling platform

The studies in the thesis utilize the numerical modelling platform ELLE (Jessell et al., 2001; Bons et al., 2008; Piazolo et al., 2010; http://www.elle.ws) in two-dimensional simple- and pure-shear deformation. ELLE is an open-source software, which has been used to simulate a range of geological processes and structures, such as dynamic recrystallization (Piazolo et al., 2002; Gomez-Rivas et al., 2017), grain growth (Jessell et al., 2001; 2003), strain localization (Jessell et al., 2005; Gardner et al., 2017) and deformation of multi-phase rocks (Jessell et al., 2009; Griera et al., 2011; 2013; Llorens et al., 2013a,b; Ran et al, 2018b, *Chapter 4*), and polar ice microstructures (Roessiger et al., 2011; Montagnat et al., 2014; Bons et al., 2016; Llorens et al., 2016a,b; 2017; Jansen et al., 2016; Steinbach et al., 2016; 2017). ELLE simulates the interaction of deformation process and the evolution of structures, and is therefore is ideally suited for the simulations in the thesis.

The two-dimensional data structure of ELLE is defined as two layers: (1) a contiguous set of polygons (termed *flynns*; Fig.6a,c) and (2) a set of unconnected nodes (termed *undoes*) (Fig. 6d). The boundaries of *flynns* consist of straight segments that are connected by boundary nodes (termed *bnodes*) in either double- or triple-junctions (Fig. 6c,d). The phases are defined

and visible by the *flynns* with various material properties in multi-phase simulations. In this study, the *unodes* are mapped on a regular rectangular 128×128, 256×256 or 512×512 grid. They store the material properties and state variables including stress, strain rate and lattice orientation.

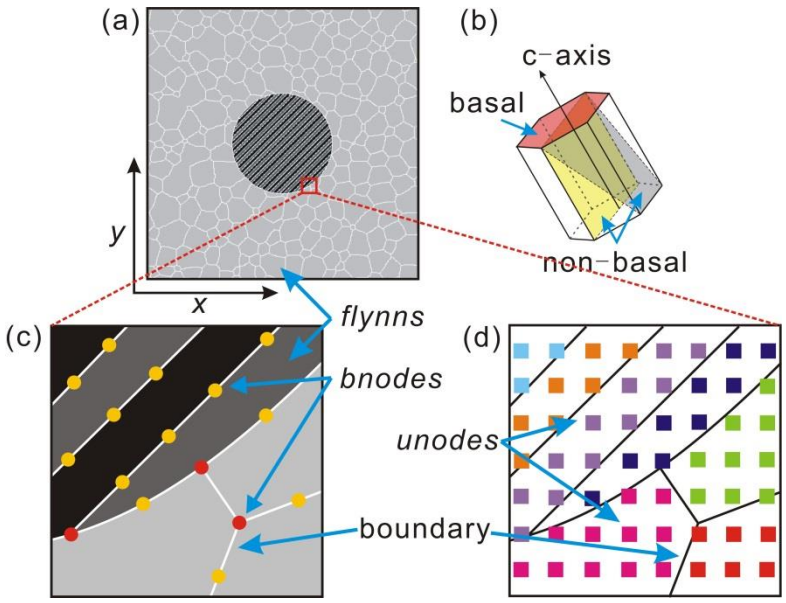

Fig. 6. Data structure. **(a)** The square unit-cell contains multiple phases (black, dark grey and light grey) composed of a set of *flynns* (defined by white solid lines). **(b)** Deformation is assumed to take place by glide of dislocations along the slip systems of a hexagonal mineral. **(c)** *Flynns* are defined by *bnodes* and define the grain boundaries, as well as sub-regions. **(d)** Unconnected nodes (*unodes*) are superimposed on *flynns* and used for storing physical properties and state variables.

5.2. Viscoplastic fast Fourier transform method (VPFFT)

The viscoplastic fast Fourier transform method (VPFFT) is used for the calculation of the deformation field, coupled with ELLE platform (Griera et al., 2013; Llorens et al., 2016b). Griera et al. (2011) summarise the function of the VPFFT code as such *"Briefly, the FFT formulation provides an exact solution of the micromechanical problem by finding a strain rate and stress field, associated with a kinematically admissible velocity field, that minimizes the average local work-rate under the compatibility and equilibrium constraints"*. More

details can be found in Lebensohn, 2001; Lebensohn et al., 2009; 2011; and Montagnat et al., 2014). In the VPFFT code intracrystalline deformation is assumed to be only accommodated by dislocation glide on different slip systems. It makes it possible to simulate the deformation of both isotropic and anisotropic crystalline materials using linear or power-law rheologies. The constitutive equation between the strain rate $\dot{\varepsilon}_{ij}(x)$ and the deviatoric stress $\sigma'(x)$ at each position *x* is given by

$$\dot{\varepsilon}_{ij}(x) = \sum_{s=1}^{N_s} m_{ij}^s(x)\dot{\gamma}^s(x) = \dot{\gamma}_0 \sum_{s=1}^{N_s} m_{ij}^s \left|\frac{m^s(x):\sigma'(x)}{\tau^s(x)}\right|^n sgn(m^s(x):\sigma'(x)), \quad (5)$$

where the sum runs over all N_s slip systems, m^s, $\dot{\gamma}^s$ and τ^s are the symmetric Schmidt tensor defined by the dyadic product of a vector normal to slip plane and slip direction, the shear strain rate and the critical resolved shear stress (CRSS) of the slip system *s*, respectively, $\dot{\gamma}_0$ is reference strain rate and *n* is the stress exponent (from Llorens et al., 2016b). A hexagonal symmetry "mineral" is used to simulate the mechanical properties of the polycrystal, and deformation is allowed to be accommodated by glide along basal-plane and along non-basal systems (i.e. pyramidal and prismatic; Fig. 6b). The resistance to shear of slip systems is simulated by means of the critical resolved shear stress (CRSS). For mechanical isotropic material, all CRSS are identical on basal and non-basal slip planes of a single phase. For mechanical anisotropic material, the grain anisotropy parameter (*A*) is used to accounts for the degree of anisotropy, which is the ratio of the critical resolved stresses of the non-basal basal to basal slip systems (e.g. Lebensohn et al., 2009; Ran et al., 2018b, *Chapter 4*; de Riese et al. (submitted), *Chapter 5*). *A* is comparable to the ratio between normal and shear viscosity as employed by e.g. Mühlhaus et al. (2002) and Kocher et al. (2006; 2008).

To simulate conglomerates, two materials are defined: pebble and matrix, each with its own (non-linear) viscosity. The relative strength of the pebbles is defined by the viscosity ratio $R\eta$. For isotropic simulations, $R\eta$ is the real viscosity ratio in linear rheology (*n*=1). In power-law rheology (in this study typically *n*=3), the meaning of $R\eta$ is more complex, as viscosity is not constant in power-law materials. The viscosity ratio is defined by:

$$R_\eta = \frac{\eta_{pebble}}{\eta_{matrix}} = \frac{\sigma_{pebble} / \dot{\varepsilon}_{pebble}}{\sigma_{matrix} / \dot{\varepsilon}_{matrix}} . \qquad (6)$$

Two end members can be envisaged: (i) stress is identical in both materials and strain rate is partitioned (Reuss bound; Reuss, 1929), and (ii) strain rate is identical in both materials and stress is partitioned (Voigt or Taylor bound; Voigt, 1928). Effective viscosity ratios range between these two extremes:

Reuss: ($\sigma_{pebble} = \sigma_{matrix}$): $$\frac{\eta_{pebble}}{\eta_{matrix}} = \frac{\sigma / \dot{\varepsilon}_{matrix}}{\sigma / \dot{\varepsilon}_{pebble}} = \frac{A\left(\frac{\sigma}{\tau_{matrix}}\right)^n}{A\left(\frac{\sigma}{\tau_{pebble}}\right)^n} = \left(\frac{\tau_{pebble}}{\tau_{matrix}}\right)^n = \left(R_\eta\right)^n \qquad (7a)$$

and Voigt: ($\dot{\varepsilon}_{pebble} = \dot{\varepsilon}_{matrix}$): $$\frac{\eta_{pebble}}{\eta_{matrix}} = \frac{\sigma_{pebble} / \dot{\varepsilon}}{\sigma_{pebble} / \dot{\varepsilon}} = \frac{\tau_{pebble}\left(\frac{\dot{\varepsilon}}{A}\right)^{1/n}}{\tau_{matrix}\left(\frac{\dot{\varepsilon}}{A}\right)^{1/n}} = \frac{\tau_{pebble}}{\tau_{matrix}} = R_\eta \quad . \qquad (7b)$$

The real viscosity ratio for $n>1$ can range from $R\eta$ to $R\eta^n$, depending on the partitioning of stress and strain rate.

5.3. Program flow of the VPFFT+ELLE method

The Fourier points (*unodes*) are used to map critical resolved shear stresses (CRSS), stress exponents (n) and lattice orientations (three Euler angles). The VPFFT code reads information from each *unode* (through *fft2elle* code) and calculates the stress and strain rate field, as well as the velocity for each *unode* (*fft* code; Fig.7). After each calculation step of the VPFFT code, all information is updated in *undoes* (through *fft2elle* code; Fig.7). Velocity boundary conditions with constant strain rate are applied in the model, with top-to-the-right simple shear deformation or vertical shortening. Displacements ($\Delta\boldsymbol{x}$) are derived from a linear integration of velocities ($\boldsymbol{v}$) over a small time increment (Δt): $\Delta\boldsymbol{x}=\boldsymbol{v}\cdot\Delta t$, to achieve strain increments. The numerical simulation is achieved by iterative application of small time steps

of each process in turn. The displacement field is used to incrementally move boundary nodes that define the *flynn* boundaries. The model is repositioned to the initial rectangular unit cell and *unodes* are mapped back on the regular, rectangular grid, if necessary (only for simple shear), as is required by the VPFFT method, before each next deformation step (Fig. 7). More details of codes and program flow see Griera et al. (2013), Llorens et al. (2016b) and Steinbach (2017).

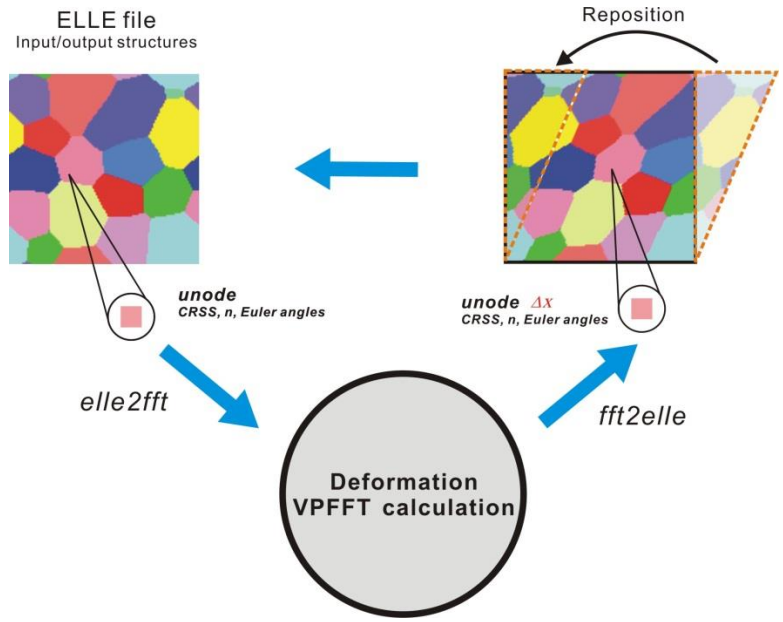

Fig. 7. Program flow of the VPFFT+ELLE methods. The VPFFT code reads information of each *unode*, does calculation and then updates information of each *unode*. For simple shear, reposition function is required before the next deformation step.

5.4. Model resolution

Each model can be mapped with $2^m \times 2^m$ *undoes*, with *m* a positive integer, which results in different resolutions of the models. To test the effect of different resolutions, we performed one multi-phase model with resolutions of 128×128, 256×256 and 512×512 *unodes* (Fig. 8). The models with 256×256 and 512×512 *undoes* show similar patterns of folds within inclusions, whereas the 128×128 model is distinctly different (Fig. 8a-c). The strain rate and stress localisation can be clearly identified in the inclusion layers with alternating viscosity in the

256×256 and 512×512 models, but there is distinctly less strain rate localisation inside the inclusion in the 128×128 model (Fig. 8d-i). This test shows that a resolution of 128×128, where the individual layers are one *unode* wide, is not sufficient. As the results of the 256×256 and 512×512 tests are almost identical, we chose 256×256 for all further runs as a compromise between resolution and calculation time. More details of the resolution effect in homogenous materials see de Riese et al. (submitted, *Chapter 5*).

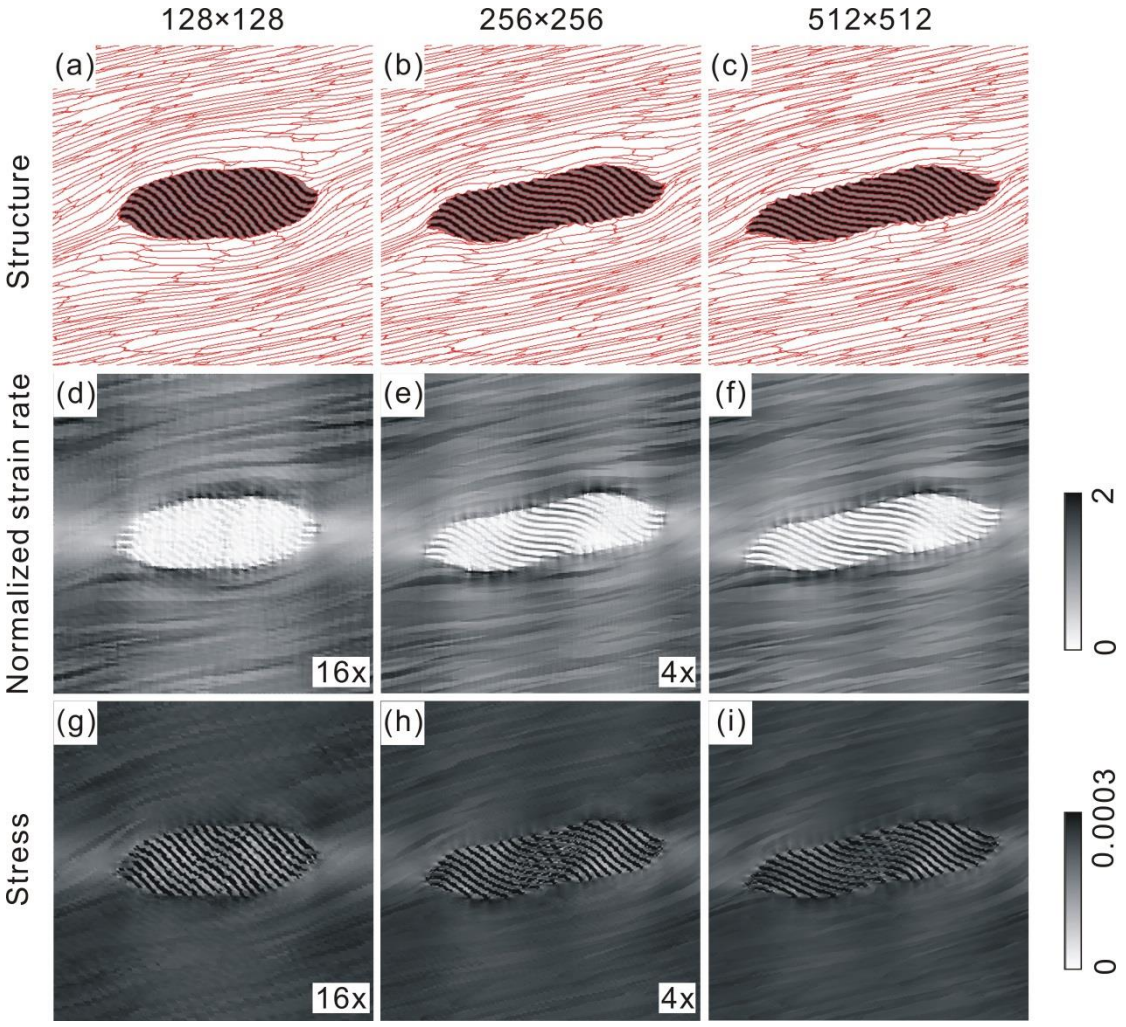

Fig.8. Structures **(a-c)**, normalized strain rate **(d-f)** and stress **(g-i)** in 128×128, 256×256 and 512×512 resolution models, at simple-shear deformation (top-to-right) to a finite strain of four. The models use same initial structure that consists of an inclusion with alternating viscosity layers embedded in an isotropic matrix.

6. Framework and main conclusions of the thesis

6.1 Framework of the thesis and introduction of chapters

This thesis utilizes the numerical modelling method of the VPFFT+ELLE to simulate the viscous deformation of conglomerates with multi-pebbles and internal structures within pebbles, and the development of deformation structures and shear localisation due to mechanical anisotropy.

- ***Chapter 1 Introduction***. The present *chapter 1* introduces the general background, briefly reviews deformation of conglomerates and mechanical anisotropy, the motivation of the thesis, the numerical modelling methods, the framework and main conclusions and the future perspectives.

- ***Chapter 2 High-strain deformation of conglomerates: numerical modelling, strain analysis, and an example from the Wutai Mountains, North China Craton.*** In order to understand the influence of the pebble concentration and the interaction between pebbles, the ductile deformation of conglomerates with multiple pebbles is modelled with various viscosity contrasts between pebbles and matrix and pebble concentrations, in linear (n=1) and power-law (n=3) viscous rheologies, under simple shear conditions up to a shear strain of ten using the VPFFT+ELLE numerical modelling method. A mean R_f -ϕ plot is suggested to gain an estimate of deformed pebble type of behaviour and the amount of strain. A natural example of deformed conglomerates from the Wutai Mountains, North China Craton is provided, whose finite strain and viscosity contrast are estimated with the mean R_f -ϕ plot.

- ***Chapter 3 Folding within pebbles during ductile simple-shear deformation: a numerical approach.*** It is not clear how and when folding within pebbles develops with deformation of conglomerates in nature. The folding within pebbles in the conglomerates with single or multiple pebble(s) are simulated, varying the orientation of pebble layers and the viscosity contrast among soft, hard layers and matrix in power law (n=3) rheology up to a ductile simple-shear strain of eight. Several folding cases are observed in simulations and suggest that the folds within pebbles from the deformed conglomerates in the Wutai Mountains, North China Craton develop with the

conglomerate deformation.

- ***Chapter 4 Time for anisotropy: The significance of mechanical anisotropy for the development of deformation structures.*** Among factors that control deformation and the resulting structures, mechanical anisotropy has proven difficult to tackle. Using the VPFFT+ELLE approach for viscoplastic deformation of crystalline materials, this paper shows how mechanical anisotropy has a profound effect on developing structures, such as crenulation cleavages, porphyroclast geometry and the initiation of shear bands and shear zones.

- ***Chapter 5 Shear localisation in homogeneous, anisotropic materials: a numerical study.*** Of the various mechanisms for localisation, mechanical anisotropy has received relatively little attention, especially in numerical modelling. Simple-shear deformation of a homogeneous, but anisotropic, power-law rheology material is simulated up to shear strains of five, using the VPFFT+ELLE approach. The effects of the mechanical anisotropy are addressed and the numerical simulations are compared with the natural case of the Northern Shear Belt at Cap de Creus, NE Spain.

- ***Appendix numerical model setup.*** The appendix gives the descriptions of the input files and parameters of the VPFFT+ELLE method used in the simulations of the thesis.

6.2 Main conclusions of the thesis

The thesis shows how the viscosity ratio between pebble and matrix and the pebble concentrations affect the deformation of conglomerates, how folds within pebbles can develop as a conglomerate deforms, and how the mechanical anisotropy affects the development of structures and shear localisation.

(1) In deformed conglomerates, pebbles can behave as rigid, deformable and passive inclusions depending on both the viscosity ratio and their concentration. Raising the pebble concentration also raises the transition viscosity ratio between the deformation regimes. The effect of increasing pebble concentration is similar to a decrease of viscosity ratio between pebbles and matrix, and *vice versa*. An increase in concentration and interaction enhances pebble distortion, but reduces the mean rotation of pebbles. Clusters of closely spaced pebbles can behave as single objects. Rigid clusters continue rotating,

but survive for only a short strain interval. Deformable clusters initially rotate rapidly towards the shear direction, and then keep on elongating with minor rotation. The slower rotation facilitates the stability of deformable clusters. A mean R_f-ϕ plot is suggested to gain an estimate of pebble deformation behaviour and the amount of strain in cases of permanently stretching pebbles. Using the mean R_f-ϕ plot, it is suggested that the deformed conglomerates of the Hutuo Group in the Wutai mountains had a viscosity ratio of 5 to 8 for a linear rheology (n=1) and 2 to 5 for a power-law rheology (n=3) and underwent a simple shear strain of about six.

(2) Deforming layered pebbles may develop internal folds. Internal folding is facilitated by a layering initially at around 174 ° to 178 ° relative to the shear plane, sufficiently thin internal layers to achieve fold wavelengths smaller than the diameter of the pebble, and a high area fraction of pebbles. Internal folding furthermore requires a narrow range of viscosity ratios between pebble and matrix to allow enough strain to develop folds, but still keep the pebble recognisable as such. The difficulty in achieving internal folds within pebbles may explain the scarcity of internally folded BIF-pebbles in deformed conglomerates in the Wutai Mountains, North China Craton. Our simulations thus indicate that the few pebbles with folds must not necessarily indicate a previous deformation event, but may have formed during deformation of the conglomerate itself. This alternative interpretation has significant impact on the geotectonic history of the Trans-North China Orogen, as it may "remove" a whole cycle of burial, metamorphism, deformation and exhumation preceding the deposition of the conglomerates.

(3) Mechanical anisotropy can play a key role on the development of folds, mantled clasts and C' shear bands. Under pure and simple shear, the geometry of the folded single layer in the anisotropic matrix is similar to that in isotropic matrix. However, the geometry of microfolds represented by passive gridlines in the anisotropic matrix is very different from those in isotropic cases. The grid lines are folded in similar-type folds or crenulations that do not decay away from the competent layer. Fold hinges align to form an axial-planar crenulation cleavage. In case of the mantled clast embedded in anisotropic matrix, deformation in the matrix is highly heterogeneous with folds and shear bands. Rotation of the clast is now inhibited and the attachment points of the wings do not rotate enough to develop the distinct embayments of δ-clasts. Instead, a σ-clast forms. In contrast, a clast in an isotropic matrix rotates faster, leading to wings developed by smearing out of the mantle. As the points where the wings attach to the object rotate along

with the object, a δ-clast develops. C' shear bands formed in all models of anisotropic composite material with >1% weak phase and were more abundant in models with a higher proportion of weak phase. In nature models C' shear bands are dominantly defined by the weakest phase. It is suggested that anisotropy is required for their development.

(4) Mechanical anisotropy leads to distinct strain and strain-rate localisation in homogenous, anisotropic materials. Localisation of shear rate in narrow shear bands occurs, depending on the magnitude of anisotropy and the stress exponent. At high anisotropy values, strain-rate frequency distributions become approximately log-normal with heavy, exponential tails. Localisation due to anisotropy is scale-independent and thus provides a single mechanism for a self-organised hierarchy of shear bands and zones from the mm- to km-scale.

7. Future perspectives

The studies gain the knowledge of the deformation of conglomerates with multiple pebbles, the development of folding in layered pebbles and the effects of mechanical anisotropy, as mentioned above. However, some questions remain unanswered.

7.1 Linear or power-law rheology in viscous flow?

Rock and mineral experiments support that rocks usually exhibit a power-law rheology, i.e. the stress exponent is larger than one (e.g., Carter and Tsenn, 1987; Kirkby and Kronenberg, 1987). Rocks typically deform by dislocation creep mechanisms, and thus show the power-law relationship between strain rate and stress, with the stress exponent generally between 2 and 8 (Carter and Tsenn, 1987). However, some field studies on deformed conglomerates show similar values of viscosity ratio between pebbles and matrix and suggest common type rocks in conglomerates mostly behave in linear rheology (e.g., Treagus and Treagus, 2002). As mentioned above, a range of analytical theories and numerical models are assume rocks to behave as linear (Newtonian) viscous fluid, i.e. stress exponent is one (e.g., Gay, 1968; Bilby et al, 1975; Treagus and Treagus, 2001). More and more analytical theories and numerical models, as well as the models in this thesis, have extended the field to the

power-law rheology (e.g., Mancktelow, 2011; Griera et al., 2011; 2013; Llorens et al., 2013). However, the term of viscosity ratio that is widely used in models with power-law rheology is essentially applied to linear rheology. In strict terms, there is no constant viscosity ratio in power-law rheology, as the discussion in *Section* 5 *Numerical modelling methods* above. Furthermore, only a stress exponent of three is used in this thesis to model power-law rheology. It is still necessary to consider whether rocks commonly behave in power-law rheology and which value of the stress exponent should be used in simulations.

7.2. Pebble shapes

Pebble shape can affect the deformation of conglomerates (e.g., Gay, 1968; Treagus and Lan, 2000; 2004; Treagus, 2002). In nature, pebble shapes in 2D plane are variable: nearly circular or elliptical shapes in well-rounded conglomerates and angular shapes in poorly rounded conglomerates. Nearly circular or elliptical pebbles deform to other elliptical shapes, whereas angular ones can deform to irregular shapes under pure and simple shear (Treagus, 1996; Treagus and Lan, 2000; 2003). Irregular shapes give more difficulties for understanding the deformation of conglomerates, since it is much easier to develop heterogeneous strain on pebbles than with elliptical ones. The studies in this thesis only consider the deformation of initially circular pebbles in multi-pebble models. Few studies deal with the effect of the pebble concentration and the interaction between pebbles using the multi-pebble model with different pebble shapes, which can be addressed in future.

7.3. Pebbles embedded in an anisotropic matrix

The studies on mechanical anisotropy in this thesis reveal the influence of anisotropy on the development of structures, such as folds, mantled clasts and shear bands. It has been pointed out that the mechanical anisotropy in the matrix develops strain localisation and leads to the inhibition of the rotation of rigid inclusions, as well as the mantled inclusions (Griera et al., 2011; 2013; Ran et al., 2018b, *Chapter 4*). It means we need to consider the influence of mechanical anisotropy in the matrix on the deformation of conglomerates with multiple

pebbles. The strain localisation in an isotropic matrix is controlled by the distribution of pebbles. If the matrix is mechanically anisotropic, the strain localisation can be affected by both pebble distribution and anisotropy. Another effect of anisotropic matrix is the inhibition of the rotation of pebbles. The anisotropy can slow down or even stop the pebble rotation. The viscosity contrast becomes complex if the matrix is anisotropic, even in linear rheology, because the viscosities on different slip planes are not identical. The calculated viscosity contrast only offers the ratio of isotropic pebble viscosity to average matrix viscosity on different slip planes.

References

Bai, J.: The early Precambrian geology of Wutaishan, Tianjin Science and Technology Press, 1986.

Bell, T. H., Johnson, S. E., Davis, B., Forde, A., Hayward, N., and Wilkins, C.: Porphyroblast inclusion-trail orientation data: eppure-non-son-girate, Journal of Metamorphic Geology, 10, 295-307, 1992.

Bercovici, D.: Plate tectonics, damage and inheritance, Nature, 508, 513–516, 2014.

Bilby, B. A., and Kolbuszewski, M. L.: The finite deformation of an inhomogeneous in two-dimensional slow viscous incompressible flow, Proceedings of Royal Society, A355, 335-353, 1977.

Bilby, B. A., Eshelby, J. D., and Kundu, A. K.: The change of shape of a viscous ellipsoidal region embedded in a slowly defomring matrix having a different viscosity, Tectonophysics, 28, 265-274, 1975.

Biot, M. A.: Theory of folding of stratified viscoelastic media and its implications in tectonics and orogenesis, Geological Society of America Bulletin, 72(11), 1595-1620, 1961.

Blumenfeld, P., and Bouchez, J. -L.: Shear criteria in granite and migmatitc deformed in magmatic and solid state, Journal of Structural Geology, 10, 361-372, 1988.

Bons, P. D., and Cox, S. J. D.: Analogue experiments and numerical modelling on the relation between microgeometry and flow properties of polyphase materials, Materials Science and Engineering, A175, 237-245, 1994.

Bons, P. D., Barr, T. D., and ten Brink, C. E.: The development of delta-clasts in non-linear viscous materials: a numerical approach, Tectonophysics, 270, 29-41, 1997.

Bons, P. D., Jansen, D., Mundel, F., Bauer, C. C., Binder, T., Eisen, O., Jessell, M. W., Llorens,

M. -G., Steinbach, F., Steinhage, D., Weikusat, I.: Converging flow and anisotropy cause large-scale folding in Greenland ice sheet, Nature Communications, 7, doi: 10.1038/ncomms11427, 2016.

Bons, P. D., Koehn, D., Jessell, M. W. (Eds.): Microdynamics simulation, In: Lecture Notes in Earth Science 106, Springer, 2008.

Carter, N. L., and Tsenn, M. C.: Flow properties of continental lithosphere, Tectonophysics, 136(1-2), 27-63, 1987.

Czeck, D. M., and Hudleston, P. J.: Testing models for obliquely plunging lineations in transpression: a natural example and theoretical discussion, Journal of Structural Geology, 25(6), 959-982, 2003.

Czeck, D. M., Fissler, D. A., Horsman, E., and Tikoff, B.: Strain analysis and theology contrasts in polymictic conglomerates: An example from the Seine metaconglomerates, Superior Province, Canada, Journal of Structural Geology, 31, 1365-1376, 2009.

Dabrowski, M., and Schmid, D. W.: A rigid circular inclusion in an anisotropic host subject to simple shear, Journal of Structural Geology, 33, 1169-1177, 2011.

Dabrowski, M., Schmid, D. W., and Podladchikov, Y. Y.: A two-phase composite in simple shear: Effective mechanical anisotropy development and localization potential, Journal of Geophysical Research, 117, B08406, 10.1029/2012JB009183, 2012.

Davis, G. H., Reynolds, S. J., and Kluth, C. F.: Structural geology of rocks and regions, John Wiley & Sons, 2011.

Du, L., Yang, C., Wyman, D. A., Nutman, A. P., Zhao, L., Lu, Z., Song, H., Geng, Y., and Ren, L.: Zircon U-Pb ages and Lu-Hf isotope compositions from clastic rocks in the Hutuo Group: Further constraints on Paleoproterozoic tectonic evolution of the Trans-North China Orogen, Precambrian Research, 10.1016/j.precamres.2017.04.007, 2017.

Dunnet, D.: A technique of finite strain analysis using elliptical particle, Tectonophysics, 7 (2), 117-136, 1969.

Erslev, E. A., and Ge, H.: Least-squares center-to-center and mean object ellipse fabric analysis, Journal of Structural Geology, 12(8), 1047-1059, 1990.

Eshelby, J. D.: The determination of the elastic field of an ellipsoidal inclusion, and related problems, Proceedings of the Royal Society, A241, 376-396, 1957.

Eshelby, J. D.: The elastic field outside an ellipsoidal inclusion, Proceedings of the Royal Society,A252, 561-569, 1959.

Etchecopar, A.: A plane kinematic model of progressive deformation in a polycrystalline aggregate, Tectonophysics, 39, 121-139, 1977.

Fletcher, R. C.: Anisotropic viscosity of a dispersion of aligned elliptical cylindrical clasts in

viscous matrix, Journal of Structural Geology, 26, 1977-1987, 2004.

Fletcher, R. C.: Deformable, rigid, and inviscid elliptical inclusions in a homogeneous incompressible anisotropic viscous fluid, Journal of Structural Geology, 31(4), 382-387, 2009.

Flinn, D.: On the deformation of the Funzie conglomerate, Fetlar, Shetland, The Journal of Geology, 64 (5), 480-505, 1956.

Fossen, H.: Structural geology, Cambridge University Press, 2016.

Freeman, B., and Lisle, R. J.: The relationship between tectonic strain and the three-dimensional shape fabrics of pebbles in deformed conglomerates, Journal of the Geological Society, 144(4), 635-639, 1987.

Fry, N.: Random point distributions and strain measurement in rocks, Tectonophysics, 60 (1), 89-105, 1979.

Gardner, R., Piazolo, S., Evans, L., and Daczko, N.: Patterns of strain localization in heterogeneous, polycrystalline rocks–a numerical perspective, Earth and Planetary Science Letters, 463, 253-265, 2017.

Gay, N. C.: Pure shear and simple shear deformation of inhomogeneous viscous fluids. 1. Theory, Tectonophysics, 5, 211-234, 1968.

Gay, N. C.: The change of shape of a viscous ellipsoidal region embedded in a slowly deforming matrix having a different viscosity—a discussion, Tectonophysics, 35(4), 403-407, 1976.

Gomez‐Rivas, E., Griera, A., Llorens, M. G., Bons, P. D., Lebensohn, R. A., and Piazolo, S.: Subgrain Rotation Recrystallization During Shearing: Insights From Full‐Field Numerical Simulations of Halite Polycrystals, Journal of Geophysical Research: Solid Earth, 122(11), 8810-8827, 2017.

Griera, A., Bons, P. D., Jessell, M. W., Lebensohn, R. A., Evans, L., and Gomez-Rivas, E.: Strain localization and porphyrocalst rotation, Geology, 39, 275-278, 2011.

Griera, A., Llorens, M. -G., Gomez-Rivas, E., Bons, P. D., Jessell, M. W., Evans, L. A., and Lebensohn, R.: Numerical modelling of porphyroclast and porphyroblast rotation in anisotropic rocks, Tectonophysics, 587, 4-29, 2013.

Happel, J.: Viscosity of suspensions of uniform spheres, Journal of Applied Physics, 28(11), 1288-1292, 1957.

Hirth, G., and Tullis, J.: Dislocation creep regimes in quartz aggregates, Journal of Structural Geology, 14(2), 145-159, 1992.

Hudleston, P. J., and Treagus, S. H.: Information from folds: a review, Journal of Structural

Geology, 32(12), 2042-2071, 2010.

Ildefonse, B., Launeau, P., Bouchez, J. L., and Fernandez, A.: Effect of mechanical interactions on the development of shape preferred orientations: a two-dimensional experimental approach, Journal of Structural Geology, 14, 73-83, 1992a.

Ildefonse, B., Sokoutis, D., and Mancktelow, N. S.: Mechanical interactions between rigid particles in a deforming ductile matrix. Analogue experiments in simple shear flow, Journal of Structural Geology, 14, 1253-1266, 1992b.

Jansen, D., Llorens, M. -G, Westhoff, J., Steinbach, F., Kipfstuhl, S., Bons, P. D., Griera, A., and Weikusat, I.: Small-scale disturbances in the stratigraphy of the NEEM ice core: observations and numerical model simulations, The Cryosphere, 10, 359-370, 2016.

Jessell, M. W., Bons, P. D., Griera, A., Evans, L. A., and Wilson, C. J. L.: A tale of two viscosities, Journal of Structural Geology, 31, 719-736, 2009.

Jessell, M. W., Kostenko, O., and Jamtveit, B.: The preservation potential of microstructures during static grain growth, Journal of Metamorphic Geology, 21(5), 481-491, 2003.

Jessell, M. W., Siebert, E., Bons, P. D., Evans, L., Piazolo, S.: A new type of numerical experiment on the spatial and temporal patterns of localization of deformation in a material with a coupling of grain size and rheology, Earth and Planetary Science Letters, 239, 309-326, 2005.

Jessell, M., Bons, P., Evans, L., Barr, T., and Stüwe, K.. Elle: the numerical simulation of metamorphic and deformation microstructures, Computers & Geosciences, 27, 17-30, 2001.

Jiang, D.: Numerical modeling of the motion of deformable ellipsoidal objects in slow viscous flows, Journal of Structural Geology, 29, 435-452, 2007a.

Jiang, D.: Numerical modeling of the motion of rigid ellipsoidal objects in slow viscous flows: A new approach, Journal of Structural Geology, 29, 189-200, 2007b.

Jiang, D.: The motion of deformable ellipsoids in power-law viscous materials: Formulation and numerical implementation of a micromechanical approach applicable to flow partitioning and heterogeneous deformation in Earth's lithosphere, Journal of Structural Geology, 50, 22-34, 2013.

Johnson, S. E., Lenferink, H. J., Price, N. A., Marsh, J. H., Koons, P. O., West Jr., D. P., and Beane, R.: Clast-based kinematic vorticity gauges: the effects of slip at matrix/clast interfaces, Journal of Structural Geology, 31, 1322-1339, 2009.

Kirby, S. H., and Kronenberg, A. K.: Rheology of the lithosphere: selected topics, Reviews of Geophysics, 25(6), 1219-1244, 1987.

Kocher, T., Mancktelow, N. S., and Schmalholz, S. M.: Numerical modelling of the effect of

matrix anisotropy orientation on single layer fold development, Journal of Structural Geology, 30, 1013-1023, 2008.

Kocher, T., Schmalholz, S. M., and Mancktelow, N. S.: Impact of mechanical anisotropy and power-law rheology on single layer folding, Tectonophysics, 421(1-2), 71-87, 2006.

Kumar, R., Srivastava, D. C., and Ojha, A. K.: A comparison of the methods for objective strain estimation from the Fry plots. Journal of Structural Geology, 63, 76-90, 2014.

Kusky T. M., and Li J. H.: Paleoproterozoic tectonic evolution of the North China Craton, Journal of Asian Earth Sciences, 22, 23–40, 10.1016/S1367-9120(03)00071-3, 2003.

Lebensohn, R. A., Idiart, M., Castañeda, P. P., and Vincent, P.-G.: Dilatational viscoplasticity of polycrystalline solids with inter-granular cavities, Philos. Maga. 91, 3038–3067, 2011.

Lebensohn, R. A., Montagnat, M., Mansuy, P., Duval, P., Meysonnier, J., and Philip, A.: Modeling viscoplastic behavior and heterogeneous intracrystalline deformation of columnar ice polycrystals, Acta Materialia, 57, 1405–1415, 2009.

Lebensohn, R. A.: N-site modeling of a 3D viscoplastic polycrystal using Fast Fourier Transform, Acta Materialia, 49, 2723-2737, 2001.

Li, J. H., and Kusky, T. M.: A late Archean foreland fold and thrust belt in the North China Craton: Implications for early collisional tectonics, Gondwana Research, 12, 47–66, 2007.

Lisle, R. J., Rondeel, H. E., Doorn, D., Brugge, J., and Van de Gaag, P.: Estimation of viscosity contrast and finite strain from deformed elliptical inclusions, Journal of Structural Geology, 5(6), 603-609, 1983.

Lisle, R. J.: Estimation of the tectonic strain ratio from the mean shape of deformed elliptical markers, Geologie en Mijnbouw, 56(2), 140-144, 1977.

Lisle, R. J.: Geological Strain Analysis. A Manual for R_f- Technique. Pergamon Press, 1985.

Lisle, R. J.: The use of the orientation tensor for the description and statistical testing of fabric, Journal of Structural Geology, 7 (1), 115-117, 1985.

Lister, G. S., Paterson, M. S., and Hobbs, B. E. : The simulation of fabric development during plastic deformation and its application to quartzite: the model, Tectonophysics, 45, 107-158, 1978.

Liu C. H., Zhao G. C., Sun M., Zhang J., He Y. H., Yin C. Q., Wu F. Y., and Yang J. H.: U–Pb and Hf isotopic study of detrital zircons from the Hutuo group in the Trans-North China Orogen and tectonic implications, Gondwana Research, 20, 106–121, 2011.

Llorens, G. -M., Griera, A., Bons, P. D., Lebensohn, R. A., Evans, L. A., Jansen, D., and Weikusat, I.: Full-field predictions of ice dynamic recrystallisation under simple shear

conditions, Earth and Planetary Science Letters, 450, 233-242, 2016a.

Llorens, G. -M., Griera, A., Weikusat, I., Bons, P. D., Roessiger, J., and Lebensohn, R. A.: Dynamic recrystallisation of ice aggregates during co-axial viscoplastic deformation: a numerical approach, Journal of Glaciology, 62, 359-377,2016b.

Llorens, M. -G., Bons, P. D., Griera, A., and Gomez-Rivas, E. : Single layer folding in simple shear, Journal of Structural Geology, 50, 209-220, 2013.

Llorens, M. -G., Griera, A., Steinbach, F., Bons, P. D., Gomez-Rivas, E., Jansen, D., Roessiger, J., Lebensohn, R. A., and Weikusat, I.: Dynamic recrystallization during deformation of polycrystalline ice: insights from numerical simulations, Philosophical Transactions Series A: Mathematical, physical, and engineering sciences, 375, 2086, 10.1098/rsta.2015.0346, 2017.

Mancktelow, N. S.: Deformation of an elliptical inclusion in two-dimensional incompressible power-law viscous flow, Journal of Structural Geology, 33, 1378-1393, 2011.

Mancktelow, N. S.: Finite-element modelling of shear zone development in viscoelastic materials and its implications for localisation of partial melting, Journal of Structural Geology, 24, 1045-1053, 2002.

Mandal, N., Samanta, S. K., Bhattacharyya, G., and Chakraborty, C.: Deformation of ductile inclusions in a multiple inclusion system in pure shear, Journal of Structural Geology, 25, 1359-1370, 2003.

Mandal, N., Samanta, S. K., Bhattacharyya, G., and Chakraborty, C.: Rotation behaviour of rigid inclusions in multiple association: insights from experimental and theoretical models, Journal of Structural Geology, 27, 679-692, 2005.

Mandal, N., Samanta, S.K., Bhattacharyya, G., and Chakraborty, C.: Deformation of ductile inclusions in a multiple inclusion system in pure shear, Journal of Structural Geology, 25, 1359-1370, 2003.

Marques, F. O., and Bose, S.: Influence of a permanent low-friction boundary on rotation and flow in rigid inclusion/viscous matrix systems from an analogue perspective, Tectonophysics, 382, 229-245, 2004.

Marques, F. O., Mandal, N., Taborda, R., Antunes, J. V., and Bose, S.: The behaviour of deformable and non-deformable inculsions in viscous flow, Earth-Science Reviews, 134, 16-69, 2014.

McNaught, M. A.: Estimating uncertainty in normalized Fry plots using a bootstrap approach, Journal of Structural Geology, 24(2), 311-322, 2002.

Montagnat, M., Castelnau, O., Bons, P. D., Faria, S. H., Gagliardini, O., Gillet-Chaulet, F., Grennerat, F., Griera, A., Lebensohn, R. A., Moulinec, H., Roessiger, J., and Suquet, P.:

Multiscale modeling of ice deformation behaviour, Journal of Structural Geology, 61, 78-108, 2014.

Mühlhaus, H. -B., Moresi, L., Hobbs, B., and Dufour, F.: Large amplitude folding in finely layered viscoelastic rock structures, Pure and Applied Geophysics, 159, 2311–2333, 2002.

Mulchrone, K. F., and Walsh, K.: The motion of a non-rigid ellipse in a general 2D deformation, Journal of Structural Geology, 28(3), 392-407, 2006.

Passchier , C. W., and Trouw, R. A. J.: Microtectonics. Springer, 2005.

Passchier, C. W., Trouw, R. A. J., Zwart, H. J., and Vissers, R. L. M.: Porphyroblast rotation - Eppur-Si-Muove, Journal of Metamorphic Geology, 10, 283-294, 1992.

Piazolo, S., and Passchier, C. W.: Experimental modeling of vicous inclusions in a circular high strain shear rig: Implications for the interpretation of shape fabrics and deformed enclaves, Journal of Geophysical Research, 107, B10242, 10.1029/2000JB000030, 2002.

Piazolo, S., Jessell, M. W., Bons, P. D., Evans, L., and Becker, J. K.: Numerical simulations of microstructures using the Elle platform: A modern research and teaching tool, Journal of the Geological Society of India, 75, 110-127, 2010.

Prakash, A., and Lebensohn, R. A.: Simulation of micromechanical behavior of polycrystals: finite elements versus fast Fourier transforms, Modelling and Simulation in Materials Science and Engineering, 17(6), 064010, 2009.

Qu, M., Jiang, D., and Lu, L. X.: An optimal scheme for numerical evaluation of Eshelby tensors and its implementation in a MATLAB package for simulating the motion of viscous ellipsoids in slow flows, Computers & Geosciences, 96, 98-108, 2016.

Ramsay, J. G., and Huber, M. I.: The techniques of modern structural geology, Volume 1: Folds and Fractures, Academic Press, 1983.

Ramsay, J. G., and Huber, M.I.: The techniques of modern structural geology, Volume 1: Strain Analysis, Academic Press, 1983.

Ramsay, J.: Folding and Fracturing of Rocks, McGraw-Hill, 1967.

Ran, H., Bons, P.D., Wang, G., Steinbach, F., Finch, M. Griera, A., Gomez-Rivas, E., Llorens, M.-G., Ran, S., Liang, X., Zhou, J., High-strain deformation of conglomerates: numerical modelling, strain analysis, and an example from the Wutai Mountains, North China Craton, Journal of Structural Geology, accepted, 2018a.

Ran, H., de Riese, T., Llorens, M. G., Finch, M. A., Evans, L. A., Gomez-Rivas, E., Griera, A., Jessell, M. W., Lebensohn, R. A., Piazolo, S., and Bons, P. D.: Time for anisotropy: The significance of mechanical anisotropy for the development of deformation structures, Journal of Structural Geology, 10.1016/j.jsg.2018.04.019, 2018b.

Reuss, A.: Berechnung der Fliessgrenzc von Mischkristallen auf Grund der

Plastizitätsbedingung fiir Einkristalle, Z. Angew. Math. Mech., 9, 49-58, 1929.

Roessiger, J., Bons, P. D., Griera, A., Jessell, M. W., Evans, L., Montagnat, M., Kipfstuhl, S., Faria, S. H., and Weikusat, I.: Competition between grain growth and grain-size reduction in polar ice, Journal of Glaciology, 57(205), 942-948, 2011.

Roters, F., Eisenlohr, P., Bieler, T. R., and Raabe, D.: Crystal plasticity finite element methods: in materials science and engineering, John Wiley & Sons, 2011.

Steinbach, F., Bons, P. D., Griera, A., Jansen, D., Llorens Verde, M. G., Roessiger, J., and Weikusat, I.: Strain localization and dynamic recrystallization in the ice–air aggregate: a numerical study, The Cryosphere, 10, 3071-3089, 2016.

Steinbach, F., Kuiper, E. J. N., Eichler, J., Bons, P. D., Drury, M. R., Griera, A., Pennock, G. M., and Weikusat, I.: The Relevance of Grain Dissection for Grain Size Reduction in Polar Ice: Insights from Numerical Models and Ice Core Microstructure Analysis, Frontiers in Earth Science, 5, 66, 2017.

Takeda, Y. T., and Griera, A.: Rheological and kinematical responses to flow of two-phase rocks, Tectonophysics, 427, 95-113, 2006.

ten Brink, C. E., and Passchier, C. W.: Modelling of mantled porphyroclasts using non-Newtonian rock analogue materials, Journal of Structural Geology, 17(1), 131-146, 1995.

Tikoff, B., and Teyssier, C.: Strain and fabric analysis based on porphyrocalst interaction, Journal of Structural Geology, 16, 477-491, 1994.

Trap, P., Faure, M., Lin, W., Le Breton, N., and Monié, P.: Paleoproterozoic tectonic evolution of the Trans-North China Orogen: toward a comprehensive model, Precambrian Research, 222, 191-211, 2012.

Treagus, S. H., and Lan, L.: Deformation of square objects and boudins, Journal of Structural Geology, 26, 1361-1376, 2004.

Treagus, S. H., and Lan, L.: Pure shear deformation of square objects, and applications to geological strain analysis, Journal of Structural Geology, 22, 105-122, 2000.

Treagus, S. H., and Treagus, J. E.: Studies of strain and rheology of conglomerates, Journal of Structural Geology, 24, 1541-1567, 2002.

Treagus, S. H., Treagus, J. E.: Effects of object ellipticity on strain, and implications for clast-matrix rocks, Journal of Structural Geology, 23, 601-608, 2001.

Treagus, S. H.: Are viscosity ratios of rocks measurable from cleavage refraction?, Journal of Structural Geology, 21, 895-901, 1999.

Treagus, S. H.: Modelling the bulk viscosity of two-phase mixtures in terms of clast shape, Journal of Structural Geology, 24, 57-76, 2002.

Treagus, S. H.: Viscous anisotropy of two-phase composites, and application to rocks and structures, Tectonophysics, 372, 121-133, 2003.

Twiss, R. J., and Moores, E. M.: Structural geology, Macmillan, 1992.

Vitale, S., and Mazzoli, S.: Influence of object concentration on finite strain and effective viscosity contrast: insights from naturally deformed packstones, Journal of Structural Geology, 27, 2135-2149, 2005.

Voigt, W.: l.ehrbuch der Kristallphysik, Teubner, 1928.

Wilde S. A., Zhao G. C., Wang K. Y., and Sun M.: First precise SHRIMP U–Pb zircon ages for the Hutuo Group, Wutaishan: further evidence for the Palaeoproterozoic amalgamation of the North China Craton, Chinese Science Bulletin, 49, 83–90, 2004.

Zhang, J., Zhao, G., Li, S., Sun, M., Chan, L. S., Shen, W., and Liu, S.: Structural pattern of the Wutai Complex and its constraints on the tectonic framework of the Trans-North China Orogen, Precambrian Research, 222, 212-229, 2012.

Zhao, G. C., Sun, M., Wilde, S. A., and Li, S. Z.: Late Archean to Paleoproterzoic evolution of the North China Craton: key issues revisited, Precambrian Research, 136, 177-202, 2005.

Zhao, G. C., Wilde, S. A., Cawood, P. A., and Sun, M.: Archean blocks and their boundaries in the North China Craton: lithological, geochemical, structural and P–T path constraints and tectonic evolution, Precambrian Research, 107, 45–73, 2001.

Zhao, G., and Zhai, M.: Lithotectonic elements of Precambrian basement in the North China Craton: review and tectonic implications, Gondwana Research, 23(4), 1207-1240, 2013.

Scientific contributions

Chapter 2

Ran, H., Bons, P.D., Wang, G., Steinbach, F., Finch, M. Griera, A., Gomez-Rivas, E., Llorens, M.-G., Ran, S., Liang, X., Zhou, J.. High-strain deformation of conglomerates: numerical modelling, strain analysis, and an example from the Wutai Mountains, North China Craton. Accepted in *Journal of Structural Geology*.

The paper is fully based on numerical simulations and field analyses of Ran. The general idea for this paper comes from the original PhD-project proposal by supervisors Bons and Wang. Authors Steinbach, Finch, Griera, Gomez-Rivas, and Llorens helped in setting up the numerical simulations and their analysis, while authors Ran S., Liang and Zhou took part in the field component in China. Ran wrote the manuscript, which was edited and commented by the other authors.

Chapter 3

Ran, H., Bons, P.D., Wang, G., Griera, A., de Riese, T., Gomez-Rivas, E., Llorens, M.-G., Ran, S., Wang, S., Wang, Y.. Folding within pebbles during ductile simple-shear deformation of conglomerates: a numerical approach. In preparation for submission to *Tectonophysics*.

This paper is fully based on numerical simulations and field analyses of Ran. The general idea for this paper comes from the original PhD-project proposal by supervisors Bons and Wang, G.. Authors Griera, de Riese, Gomez-Rivas and Llorens helped in setting up the numerical simulations and their analysis, while authors Ran S., Wang S. and Wang Y. took part in the field component in China and discussed the regional geology in the Wutai mountains, China. Ran wrote the manuscript, which was edited and commented by Bons at this stage.

Chapter 4

Ran, H., de Riese, T., Llorens, M.-G., Finch, M.A., Evans, L.A., Gomez-Rivas, E., Griera, A., Jessell, M.W., Lebensohn, R.A., Piazolo, S., Bons, P.D. Time for anisotropy: The significance of mechanical anisotropy for the development of deformation structures. Available online in *Journal of Structural Geology*. Doi: 10.1016/j.jsg.2018.04.019.

The paper was inspired by the numerical simulations carried out by Ran, which appear in 2 out 4 of the figures, which is why Ran is first author. The paper was mostly written by senior author Bons, who appears as last author. All other authors are listed in alphabetical order, not according to their contributions. Llorens, Finch and de Riese provide data and interpretations. Other authors contributed to the numerical method and all authors provided input to the

manuscript text.

Chapter 5

de Riese, T., Evans, L.A., Gomez-Rivas, E., Griera, A., Lebensohn, R.A., Llorens, M.-G., **Ran, H**., Sachau, T., Bons, P.D. Shear localisation in homogeneous, anisotropic materials: a numerical study. Submitted to *Journal of Structural Geology*.

This paper is first-authored by de Riese. The manuscript is written by de Riese, who carried out all the numerical simulations and data interpretation, under supervision of the senior author and supervisor, Bons. Ran assisted in setting up the simulations. Other authors also contributed to the numerical code and editing of the manuscript. Authors are listed alphabetically, except de Riese and Bons.

Chapter 2

High-strain deformation of conglomerates: numerical modelling, strain analysis, and an example from the Wutai Mountains, North China Craton

Hao Ran [a, b], Paul D. Bons [a,*], Genhou Wang [b], Florian Steinbach [a], Melanie Finch [a], Albert Griera [c], Enrique Gomez-Rivas [d,e], Maria-Gema Llorens [a], Shuming Ran [f], Xiao Liang [b], Jie Zhou [g]

[a] Department of Geosciences, Eberhard Karls University Tübingen, Tübingen 72074, Germany

[b] School of Earth Sciences and Resources, China University of Geosciences, Beijing 100083, China

[c] Departament de Geologia, Universitat Autònoma de Barcelona, Bellaterra (Cerdanyola del V.) 08193, Spain

[d] Departament de Mineralogia, Petrologia i Geologia Aplicada, Universitat de Barcelona, Barcelona 08028, Spain

[e] School of Geosciences, University of Aberdeen, AB24 3UE Aberdeen, United Kingdom

[f] Tianjin Center, China Geological Survey, Tianjin 300170, China

[g] Key Laboratory of Submarine Geosciences and Prospecting Techniques, Ministry of Education; College of Marine Geosciences, Ocean University of China, Qingdao 266100, China

Accepted in *Journal of Structural Geology*, 20 June 2018.

Abstract

Conglomerates have been widely used to investigate deformation history and rheology, strain, vorticity and viscosity. Previous studies reveal that several factors, such as pebble shapes and concentrations, as well as material properties, affect conglomerate deformation. However, how pebble concentration and interaction between pebbles affect deformation is not understood very well. We use the 2D numerical modelling platform ELLE coupled to the full field crystal visco-plasticity code (VPFFT) to simulate the deformation of conglomerates with various viscosity contrasts between pebbles and matrix and different pebble concentrations, with both linear (stress exponent n=1) and power-law (n=3) viscous rheologies, under simple shear conditions up to a shear strain of ten. Pebbles can behave as effectively passive, deformable or effectively rigid. An increase in pebble concentrations/viscosity contrasts enhances pebble deformation, but reduces their rotation. A mean aspect ratio (R_f) - orientation (ϕ) plot is proposed to gain an estimate of pebble deformation behaviour and the amount of bulk strain. Closely spaced rigid or deformable pebbles can form clusters that mechanically act as single inclusions. Rigid clusters rotate and survive for only short strain increments, whereas the more stable deformable ones keep on elongating with minor rotation. We provide a natural example of deformed conglomerates from the Wutai Mountains, North China Craton. These consist of banded-iron-formation (BIF) pebbles embedded in a schistose matrix. Using the mean R_f-ϕ plot, a finite strain of ~6 under simple shear could be determined. The viscosity of the pebbles is estimated at about 5 to 8 times that of the matrix for a linear rheology (n=1), or 2 to 5 times if a power-law rheology with n=3 is assumed.

Keywords: Conglomerates, numerical modelling, strain analysis, North China Craton

1. Introduction

Conglomerates have received particular attention in structural geology for studies on strain analysis, deformation process, rheology and tectonic evolution (e.g., Flinn, 1956; Ramsay, 1967; Dunnet, 1969; Fry, 1979; Lisle et al., 1983; Yin et al., 1999; Treagus and Treagus, 2002; Passchier and Trouw, 2005; Czeck et al., 2009). Deformed conglomerates are classical indicators of finite strain, stress orientation, vorticity, and viscosity contrast between pebbles and their matrix (e.g., Ramsay, 1967; Lisle et al., 1985; Freeman and Lisle, 1987; Czeck and Hudleston, 2003). Conglomerates are polyphase rocks formed by pebbles (inclusions) embedded in a matrix that is usually assumed weaker (e.g., Gay, 1968; Fletcher, 2004; Jiang, 2007a,b, 2013; Marques et al., 2014). A range of rock and analogue deformation experiments, analytical models, as well as numerical simulations have been applied to study the viscous deformation of single or multiple inclusion-matrix systems aiming to quantify their behaviour (e.g., Jeffery, 1922; Rosenberg, 2001; Treagus, 2002; Treagus and Treagus, 2002; Mancktelow, 2002, 2011; Mandal et al., 2003, 2005; Takeda and Griera, 2006; Jiang, 2007a,b, 2013; Jiang and Bentley, 2012; Johnson et al., 2009a,b; Griera et al., 2011, 2013; Dabrowski et al., 2012; Räss et al., 2016; Ran et al., 2018). These studies reveal that there are several key factors that control their deformation behaviour: (1) the initial shape of inclusion(s) (Lisle, 1979; Treagus, 2002; Treagus and Lan, 2004), (2) the material properties, in particular the viscosity contrast between inclusion and matrix (Treagus and Treagus, 2001; Mandal et al., 2003; Vitale and Mazzoli, 2005; Takeda and Griera, 2006; Griera et al., 2013), the matrix anisotropy (Treagus, 2003; Fletcher, 2004; Griera et al., 2011, 2013; Qu et al., 2016) and the linear or power-law rheology (Mancktelow, 2002, 2011; Jiang, 2013; Qu et al., 2016), (3) the behaviour of the interface between inclusion and matrix (Marques and Bose, 2004; Johnson et al., 2009b), and (4) the distribution of inclusions (Treagus, 2002; Takeda and Griera, 2006) and the interaction between them (Ildefonse et al., 1992a,b; Tikoff and Teyssier, 1994; Marques and Bose, 2004; Mandal et al., 2005; Jessell et al., 2009; Mancktelow, 2011).

Pebbles in a ductile viscous conglomerate can behave as effectively passive, deformable or

rigid inclusions, depending on the viscosity contrast between pebbles and matrix. The first analytical solutions, proposed by Eshelby (1957) and Gay (1968) and further developed by Bilby et al. (1975), Bilby and Kolbuszewski (1977) and Treagus and Treagus (2001), indicate that inclusions in linear viscous systems deformed in pure shear behave passively (i.e., their deformation rate approximately equals that of the matrix) when the viscosity (η) ratio ($R\eta=\eta_{inclusion}/\eta_{matrix}$) between inclusion and matrix is less than two (see Table 1 for a list of symbols and abbreviations). Initially circular inclusions remain effectively rigid (i.e., inclusions only undergo very minor deformation) when $R\eta$ is larger than ca. 20 to 50. In between these two end members we define "deformable inclusions" as those that deform significantly, but distinctly less than their surrounding matrix. Pulsating behaviour, with cyclical rotation of inclusions and changes in their ellipticity, can occur in non-coaxial shearing at moderate $R\eta$ (Bilby and Kolbuszewski, 1977). Based on analogue experiments, Piazolo and Passchier (2002) estimated the transitions between rigid and pulsating behaviour at $R\eta\approx$1200, and between pulsating and passive behaviour at $R\eta\approx$5 to100. Mancktelow (2011) extended the solution of Bilby and Kolbuszewski (1977) to systems with power-law rheology and proposed that the effect of power-law viscous rheology is similar to an increase of the linear viscosity contrast between the competent and soft phase. This was also observed by Llorens et al. (2013b) from modelling of single-layer folding.

Most of the studies discussed above deal with the deformation of isolated inclusions and thus ignore the influence of inclusion distribution and interactions between neighbouring inclusions. However, natural conglomerates are composed of multiple pebbles, usually resulting in interactions between neighbouring ones, especially in clast-supported conglomerates. A few studies have recognised that the deformation behaviour of inclusions and the bulk viscosity of the system are significantly affected by the concentration of inclusions and their interaction (Gay, 1968; Bons and Cox, 1994; Mandal et al., 2003, 2005; Vitale and Mazzoli, 2005; Jessell et al., 2009; Mancktelow, 2011; Dabrowski et al., 2012; Marques et al., 2014). One effect of interaction between inclusions is that they behave as if they are softer than when they are isolated in the matrix (Mandal et al., 2003; Vitale and

Mazzoli, 2005; Jessell et al., 2009). Therefore, the distribution of inclusions and their interactions are likely to affect the $R\eta$-boundaries between passive, deformable and rigid behaviour regimes. A further effect of increasing inclusion concentration and thus their interaction is that their rotation rate can be slowed down or inclusions may even stop rotating. This effect is associated with inclusion collisions or flow disturbances in the matrix (Ildefonse et al., 1992a,b; Samanta et al., 2003; Marques et al., 2014). Closely spaced inclusions can also form clusters or trains that mechanically act as single inclusions (Blumenfeld and Bouchez, 1988; Tikoff and Teyssier, 1994; Jessell et al., 2009). According to Tikoff and Teyssier (1994), clusters of rigid inclusions are short-lived, while those composed of deformable inclusions with slipping boundaries remain coherent for longer times. However, it is still not entirely clear how the pebble concentration affects the $R\eta$-boundaries between different behaviour regimes and how rigid and deformable clusters form and develop, respectively.

Numerical simulations of the deformation of inclusion-matrix systems were until recently limited to relatively low finite strains (e.g., Treagus et al., 2002; Treagus and Lan, 2003; Takeda and Griera, 2006; Jessell et al., 2009). Only recently have codes such as ELLE+VPFFT (Lebensohn, 2001; Lebensohn et al., 2009, 2011; Griera et al., 2013) and Milamin/MVEP2 (Dabrowski et al., 2008; Kaus, 2010) reached high shear strains (e.g., Dabrowski et al., 2012; Griera et al., 2013; Pouryazdan et al., 2017). In this study, we use the ELLE+VPFFT code to simulate viscous deformation of conglomerates with interactions between pebbles, varying the concentration of pebbles and viscosity ratio between pebbles and matrix, in both linear and power-law viscous rheologies, and up to a simple-shear strain of ten. Our simulations produce a range of structures, depending on the various parameters. We use conglomerates in the Wutai mountains, North China Craton, to illustrate how a proposed R_f-ϕ plot can be used to estimate the viscosity contrast between pebbles and matrix in naturally deformed conglomerates.

2. Methods

We numerically model the viscous deformation of conglomerates in two-dimensional simple shear. This study utilizes the open-source numerical modelling platform ELLE (Jessell et al., 2001; Bons et al., 2008; Piazolo et al., 2010; http://www.elle.ws), which has been applied to simulate a range of geological processes, such as strain localisation (Jessell et al., 2005; Llorens et al., 2016a,b; Gardner et al., 2017), folding (Llorens et al., 2013a,b; Jansen et al., 2016), and deformation of two-phase rocks and ice (Jessell et al., 2009; Steinbach et al., 2018), including those containing porphyroclasts and porphyroblasts (Griera et al., 2011, 2013), among many other studies. The deformation field is calculated using the VPFFT code, coupled with the ELLE software (Griera et al., 2013; Llorens et al., 2016b) for handling the data structure, re-meshing and pre- and post-processing of modelling results. Using a spectral solver, the VPFFT method finds a strain rate and stress field, associated with a kinematically admissible velocity field, which minimizes the average local work-rate under the compatibility and equilibrium constraints (Lebensohn, 2001; Griera et al., 2011). The VPFFT code requires discretisation of the system into a regular grid and periodic boundary conditions, of which the latter has the advantage that high-strain deformation in simple shear can be achieved without modifying the square model shape (a feature employed by, e.g., Jessell et al., 2009).

As we use the same numerical approach as Griera et al. (2011, 2013) we refer to them for details of the numerical procedure and to Lebensohn (2001), Lebensohn et al. (2009, 2011), Montagnat et al. (2014), and Llorens et al. (2016b) for details of the VPFFT method. A model mineral with a hexagonal symmetry is used here (similar to Griera et al., 2011, 2013) to simulate the mechanical properties of the material, and deformation is allowed to be accommodated by glide along basal plane and along non-basal systems (i.e., pyramidal and prismatic; Fig. 1e). The resistance to shear of slip systems is simulated by means of the critical resolved shear stress (CRSS; τ), which is set to the same value for the different slip systems, but is different for pebbles and matrix. This way, the materials are effectively isotropic and the lattice orientation of grid elements makes no discernible difference to the result and is assigned randomly at the beginning of the simulation. Griera et al. (2011) showed

that with this VPFFT approach the rotation rate of a circular rigid inclusion embedded in a viscous isotropic matrix successfully follows the analytical solution of Jeffery (1922), thus validating this approach for the modelling of inclusion behaviour.

In our simulations with isotropic material properties (meaning that all slip systems have the same τ), the relation between differential stress (σ) and strain rate ($\dot{\varepsilon}$) of the material is defined by:

$$\dot{\varepsilon} = A\left(\frac{\sigma}{\tau}\right)^n, \qquad (1)$$

where n is the stress exponent and A is a pre-exponential (scaling) factor, identical for all materials used in these simulations. The critical resolved shear stress (τ) of the matrix was set to unity (τ_{matrix}=1) in all cases. Pebbles are more competent than the matrix (τ_{pebble}>1). The stress exponents (n) of pebble and matrix are always identical in one simulation, being either one or three (see Table 1). We define the viscosity ratio $R\eta$ between pebble and matrix using as a proxy the CRSS ratio ($R\eta=\tau_{pebble}/\tau_{matrix}$). For linear rheology models (n=1), $R\eta$ is the real viscosity ratio. For n=3, the meaning of $R\eta$ is more complex, as viscosity is not constant in power-law materials. The effective viscosity ratio is defined by:

$$R_\eta = \frac{\eta_{pebble}}{\eta_{matrix}} = \frac{\sigma_{pebble}/\dot{\varepsilon}_{pebble}}{\sigma_{matrix}/\dot{\varepsilon}_{matrix}}. \qquad (2)$$

The 2-D description of the model conglomerate is defined in the ELLE data structure as a contiguous set of polygons (termed *flynns*; Fig. 1a,b) and a set of unconnected nodes or Fourier points (termed *unodes*; Fig. 1f). The boundaries of *flynns* consist of straight segments that connect boundary nodes (termed *bnodes*; Fig. 1c,f) in either double- or triple-junctions. In this study, *flynns* define single-phase regions, with either matrix or pebble properties. State variables, such as stress, strain rate and lattice orientation, which can vary within *flynns*, are stored in the *unodes* that are distributed on a regular, rectangular 256×256 grid.

Table 1. List of abbreviations and symbols used in the text.

A	Pre-exponential (scaling) factor
BIF	Banded Iron Formation
C	Pebble concentration
Δt	Time increment
$\Delta \boldsymbol{x}$	Displacement
n	Stress exponent
R_f	Ratio between long and short axes of inclusions (pebbles)
R_s	Aspect ratio of strain ellipse
$R\eta$	Viscosity ratio between inclusion(pebble) and matrix
$R\eta_{Gay}$	Calculated viscosity ratio by Gay's equation (1968)
VPFFT	Full field crystal visco-plasticity code
$\boldsymbol{v}$	Velocity
W	Vorticity
$\dot{\varepsilon}$	Strain rate
$\gamma, \Delta\gamma$	Finite shear strain, shear strain increment
ϕ	Orientation of the inclusion (pebble) long axis
σ	Differential stress
τ	Critical resolved shear stress (CRSS)

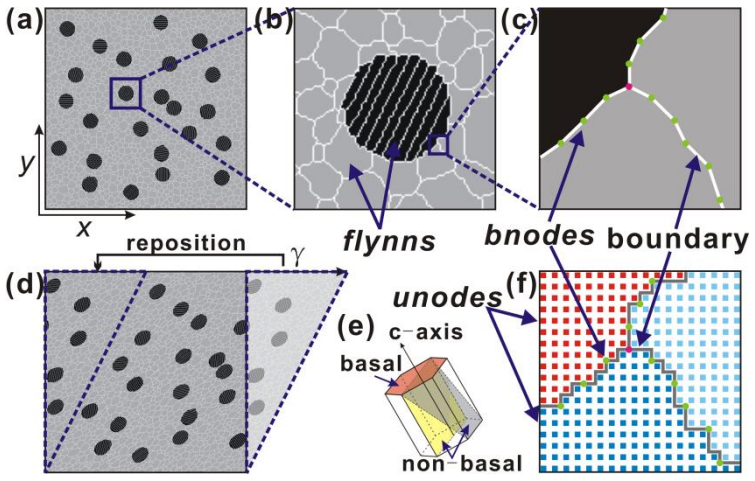

Fig. 1. Data structure. **(a)** The square unit-cell contains circular pebbles (black) embedded in a homogeneous matrix (grey) composed of a set of *flynns* (defined by white solid lines). **(b)** and **(c)** *Flynns* are defined by *bnodes* and define the pebble-matrix boundaries, as well as sub-regions. **(d)** The model is repositioned into the initial square unit cell after each step of dextral simple-shear deformation. **(e)** Deformation is assumed to take place by glide of dislocations along the slip systems of a hexagonal

mineral. **(f)** Unconnected nodes (*unodes*) are superimposed on *flynns* and used for storing physical properties and state variables. (c) and (f) show the difference of region boundaries defined by *flynns* and *unodes* that are used for the VPFFT code.

Starting models are square with a unit-cell size of 1×1 and contain approximately circular pebbles with a diameter of 0.075 times the unit-cell size. We use 24, 70 and 100 randomly-placed pebbles, corresponding to pebble concentrations (C) of 10%, 30% and 45%, respectively. Velocity boundary conditions with constant strain rate are applied in the model, with top-to-the-right simple shear deformation. Displacements ($\Delta \boldsymbol{x}$) are derived from a linear integration of velocities ($\boldsymbol{v}$) over a small time increment (Δt): $\Delta \boldsymbol{x}=\boldsymbol{v}\cdot\Delta t$, to achieve shear-strain increments of $\Delta\gamma$=0.02 /step. The velocity field is used to incrementally move boundary nodes that define the *flynn* boundaries and, hence, the pebble-matrix boundaries. The model is repositioned to the initial square unit cell and material properties (pebble or matrix) are mapped back on the regular, square grid, as is required by the VPFFT method, before each next deformation step (Fig. 1d).

Three input parameters are systematically varied in the simulations (Table 2): (1) the concentration (C) of pebbles, (2) the stress exponent for linear or power-law viscous rheology ($n=1$ *or* 3), and (3) the viscosity ratio ($R\eta$). To visualise the distribution of the strain rate intensity, we plot the von Mises strain rate (or equivalent strain rate) normalized to the bulk von Mises strain rate for each *unode*. The von Mises strain rate is the second invariant of the symmetric strain rate tensor. The distribution of the accumulated finite vorticity (W) and strain (R_s) for a strain increment are visualized by integrating the incremental stain rate tensor of each *unode* from each simulation step (Steinbach, 2017). Vorticity is the mean rotation angle (in radians) of material lines in a deforming material (e.g. Means et al., 1980). Considering the minor deformation of rigid pebbles in some simulations, we here use vorticity to visualize and discuss pebble rotation instead of the vorticity number (Means et al., 1980). We measure the ratios (R_f) between long and short axes of pebbles and the orientations of the long axes (ϕ) from the shear plane at different finite strains, using the particle analysis routine of the

freeware ImageJ software (Schneider et al., 2012; http://imagej.nih.gov/ij). The arithmetic means of R_f and ϕ are used for the statistical analysis of pebble deformation and rotation (cf. Lisle, 1977).

Table 2. Settings for the simulations presented here.

Experiment	Pebble concentration (C)	Stress exponent (*n*)	$R\eta$	Supplementary movie
$10\%^{n1}_{R\eta2}$	10%	1	2	
$10\%^{n1}_{R\eta5}$	10%	1	5	Movie 1
$10\%^{n1}_{R\eta15}$	10%	1	15	
$10\%^{n1}_{R\eta45}$	10%	1	45	
$30\%^{n1}_{R\eta2}$	30%	1	2	
$30\%^{n1}_{R\eta5}$	30%	1	5	
$30\%^{n1}_{R\eta15}$	30%	1	15	
$30\%^{n1}_{R\eta45}$	30%	1	45	
$45\%^{n1}_{R\eta2}$	45%	1	2	
$45\%^{n1}_{R\eta5}$	45%	1	5	Movie 2
$45\%^{n1}_{R\eta15}$	45%	1	15	
$45\%^{n1}_{R\eta45}$	45%	1	45	
$10\%^{n3}_{R\eta2}$	10%	3	2	
$10\%^{n3}_{R\eta5}$	10%	3	5	
$10\%^{n3}_{R\eta10}$	10%	3	10	
$30\%^{n3}_{R\eta2}$	30%	3	2	Movie 3
$30\%^{n3}_{R\eta5}$	30%	3	5	
$30\%^{n3}_{R\eta10}$	30%	3	10	Movie 4
$45\%^{n3}_{R\eta2}$	45%	3	2	Movie 5
$45\%^{n3}_{R\eta5}$	45%	3	5	
$45\%^{n3}_{R\eta10}$	45%	3	10	

3. Results

The geometries of deformed conglomerates for different $R\eta$ and values of the stress exponent (*n*) are shown in Fig. 2 for a finite strain of ten (γ=10). Selected movies (Table 2) showing the evolution of the structure and normalised strain rate can be found in appendix A.

Our simulations cover the three types of deformation behaviour of pebbles in deformed

conglomerates: (i) passive, (ii) deformable and (iii) rigid (Fig. 2). For a power-law viscous rheology (n=3), passive deformation of pebbles is observed at $R\eta$=2 and high pebble concentrations (C=45%). The same passive behaviour can be observed in systems with linear viscosity (n=1), in simulations with $R\eta$=2 (all range of pebble concentrations) and with $R\eta$=5 with high pebble concentration (C= 45%). Rigid pebble behaviour, with minor distortion and only rotation, is observed at high $R\eta$. For n=3, pebbles behave rigidly when $R\eta \geq 5$ at C=10% and 30%, and at C=45% for $R\eta$=10 only. The same pattern is observed for models with n=1, with pebbles behaving rigidly at $R\eta \geq 15$ at C=10%, and at C=30% only at $R\eta$=45. In between the end-member cases of passive and rigid behaviour, pebbles deform significantly, but distinctly less than their matrix. The deformation behaviour of pebbles in the simulations with $R\eta$=2-10 for n=3 is approximately similar to that in the simulations with $R\eta$=5-45 for n=1, in terms of amount of stretching and rotation. Pebbles in the deformable regime show elongate mica fish and σ-clast shapes (Fig. 2a,b; Passchier and Trouw, 2005). The deformed *flynn* boundaries in the matrix serve as a proxy for the expected trend that a foliation would develop by wrapping around rotating pebbles (Fig. 2a,b).

With increasing finite strain, passive and deformable pebbles keep stretching (increasing their R_f) and their long axes rotate towards the shear plane (ϕ=0) (Fig. 3). Some of deformable and rigid pebbles show pulsating behaviour. In this case their long axes rotate towards and beyond the shear plane, while their R_f values remain low (<3). The R_f-ϕ graph (Fig. 3) thus shows two types of paths. In the first ϕ consistently decreases towards ϕ=0 and R_f increases towards R_f=∞ with progressive strain. In the second case, pebbles remain "trapped" at R_f smaller than about three and variable .

At a low pebble concentration of C=10%, the mean rotation of rigid pebbles is similar to the ideal rotation of the single rigid inclusion calculated by Jeffery's (1922) solution (Fig. 4). With increasing concentration, the mean rotation of rigid pebbles decreases (Fig. 4). However, the variation in rotation rate between pebbles increases and some pebbles actually rotate faster than the prediction by Jeffery (1922).

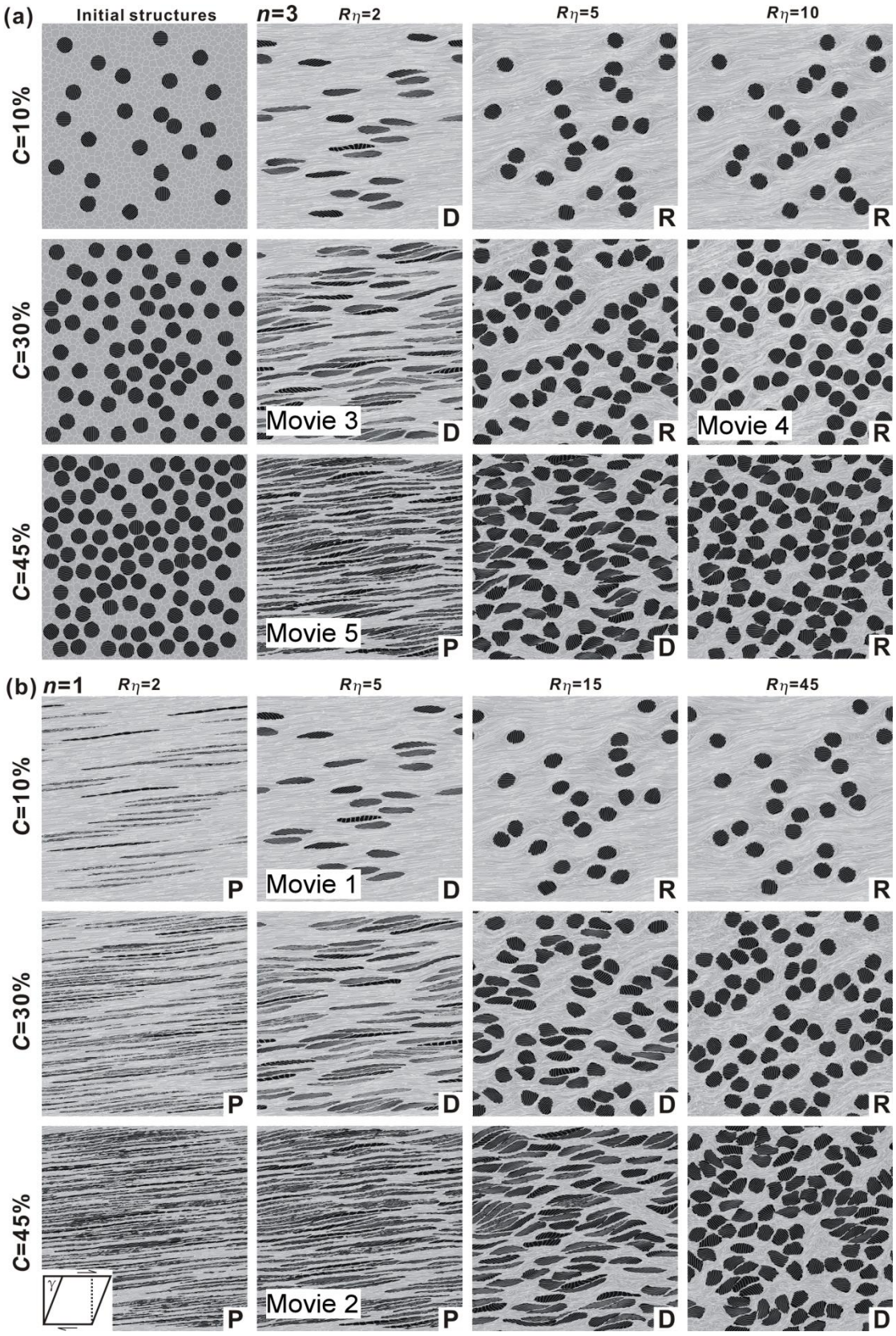

Fig. 2. Results of simulations with different $R\eta$-settings with a stress exponent of n=1 **(a)** and n=3 **(b)**

for simple-shear deformation (top to the right) up to a shear strain of γ=10. Pebbles are black, matrix light grey and *flynn* boundaries white. Initial structures of conglomerates with pebble concentrations of C=10%, 30% and 45% are shown as the first column of (a). The pebble behaviour is labelled as passive (P), deformable (D) or rigid (R). Movies 1-5 can be found in Appendix A.

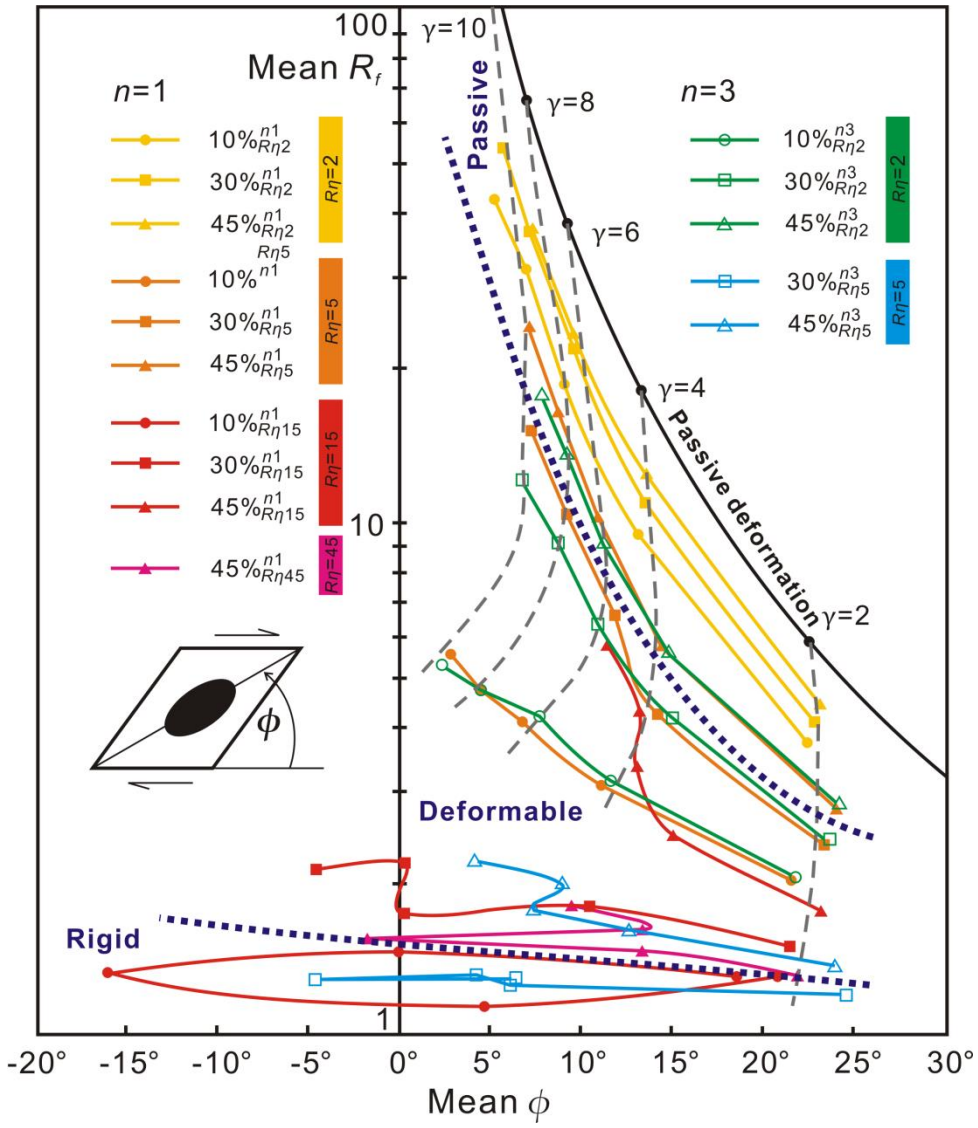

Fig. 3. Mean R_f-ϕ graph showing the trajectories of the mean pebble shape (R_f) and long axis orientation (ϕ) for the different simulations as a function of strain. All the data displayed correspond to the arithmetic mean of the R_f or ϕ of all individual pebbles in a model. Sub-vertical dashed lines indicate finite strain contours. Dark blue dashed lines separate passive, deformable and rigid pebble behaviour.

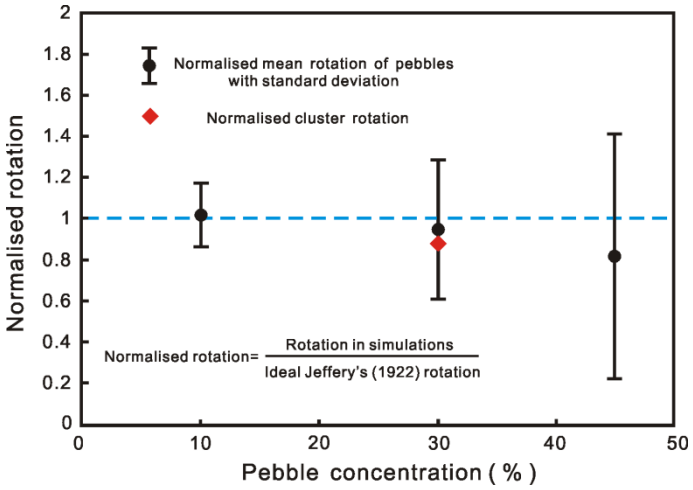

Fig. 4. Normalised mean rotation (vorticity) of all individual pebbles (with one standard deviation error bars) at different pebble concentrations of C=10%, 30% and 45% and viscosity ratio of $R\eta$=10 in power-law (n=3) viscous rheology, for a strain increment of $\Delta\gamma$=0.5. Normalised mean rotation is defined as the ratio between mean rotation angle in the simulation and the ideal Jeffery (1922) rotation of 14.3 ° for $\Delta\gamma$=0.5. Each mean rotation angle with standard deviation is calculated from all rotation data at finite strains of γ=3.5-4, 4-4.5, 4.5-5, 5-5.5 and 5.5-6 in simulations $10\%^{n3}_{R\eta10}$, $30\%^{n3}_{R\eta10}$ and $45\%^{n3}_{R\eta10}$. The rotation angle of one cluster is selected from the simulation $30\%^{n3}_{R\eta10}$ for $\Delta\gamma$=0.5 (γ=4-4.5).

As expected, strain rate and vorticity are highly variable in the matrix, especially at high $R\eta$ (Fig. 5). An increase in $R\eta$ and C enhances strain rate partitioning. The vorticity maps (Fig. 5, columns IV-VI) illustrate the sense of rotation of local deformation. Some of the highest strain rates (red tones in Fig. 5, columns II-III) are associated with a clockwise rotation (dextral shear, red tones in Fig. 5, columns V-VI) and develop in nearly horizontal zones, thus indicating the activity of synthetic C-type shear bands. At high $R\eta$ and C, vertical, C"-type shear bands with significantly elevated strain rates and negative vorticity (i.e., sinistral shear-sense) also form.

Clusters formed by the association of several closely spaced deformable or rigid pebbles can behave as effectively single objects. They form with increasing finite strain in simulations

with high pebble concentrations such as $30\%_{R\eta 10}^{n3}$ and $30\%_{R\eta 2}^{n3}$ (Figs. 6, 7). In the simulations with rigid pebbles such as $30\%_{R\eta 10}^{n3}$, antithetic shear zones initially form perpendicular to the shear plane and progressively rotate toward it (Figs. 6, 7). The cluster formed by rigid pebbles rotate less than the mean rotation of individual pebbles and Jeffery's (1922) rotation model in simulation $30\%_{R\eta 10}^{n3}$ (Fig. 4).

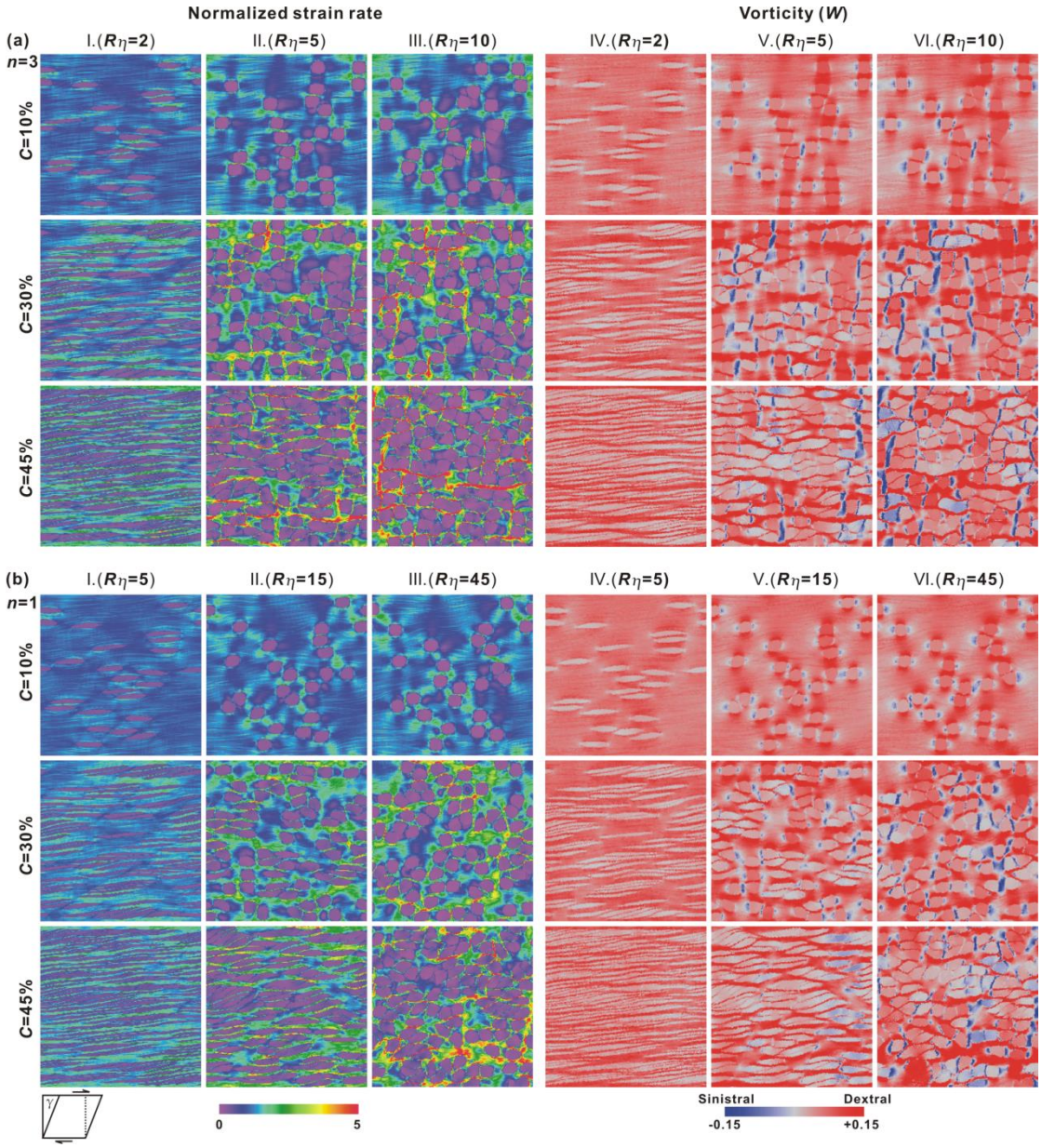

Fig. 5. Maps of the von Mises strain-rate field normalised to the bulk von Mises strain rate at different viscosity ratios ($R\eta$) (column I-III) and vorticity (for $\Delta\gamma$=0.02) at different viscosity ratios ($R\eta$)

(column IV-VI) for **(a)** power-law (n=3) and **(b)** linear (n=1) viscous rheology at finite strain of 10. The bulk sense of shear is top to right.

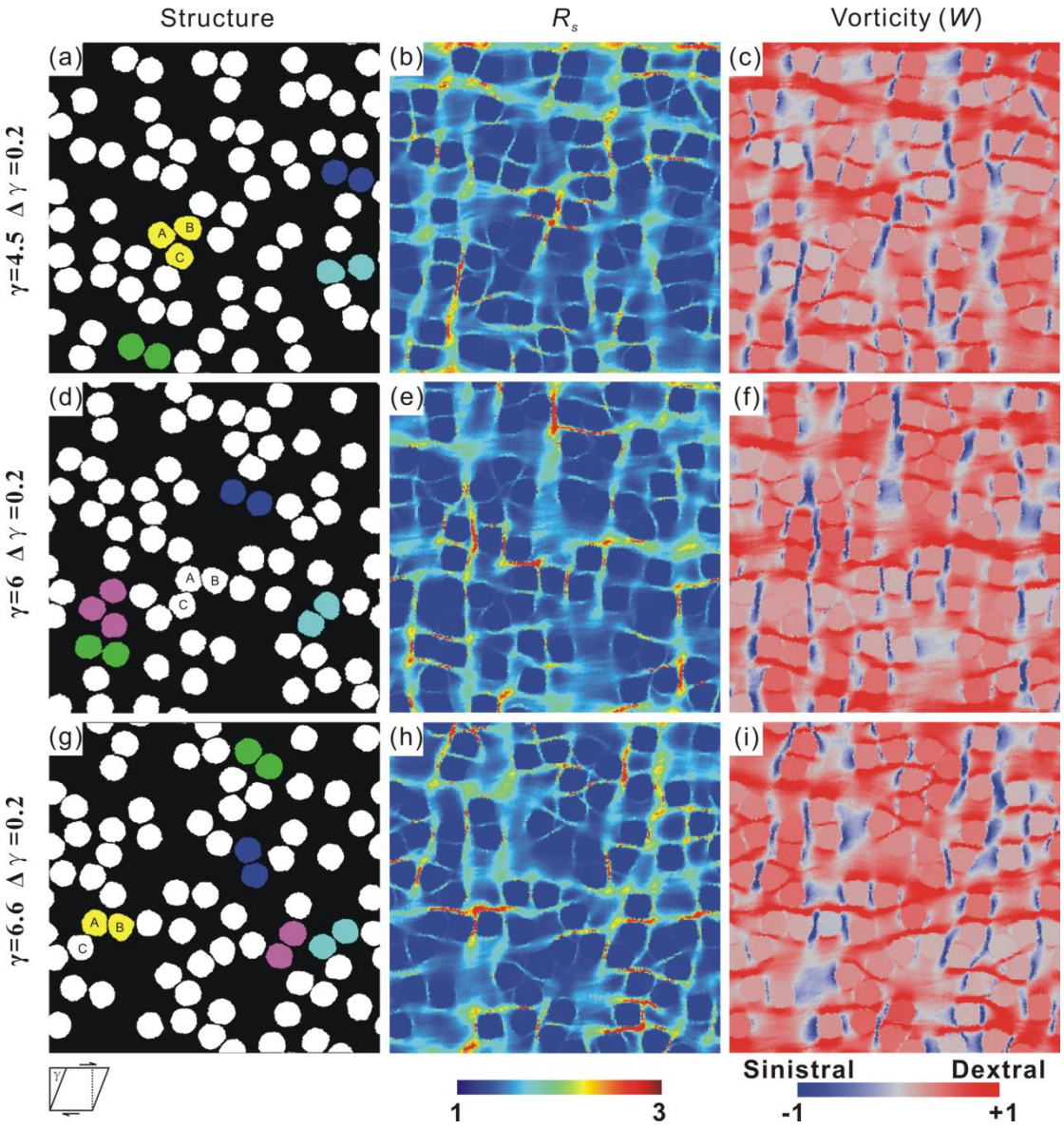

Fig. 6. Evolution of rigid clusters in the simulation $30\%^{n3}_{R\eta 10}$ (Appendix A, Movie 4). Pebble (white and coloured) and matrix (black) distribution is shown at shear strains of **(a)** γ=4.5, **(d)** at γ=6.0 and **(g)** γ=6.6. Pebbles belonging to a cluster are coloured. Incremental strain (R_s; **b, e, h**) and vorticity (W; **c, f, i**) distributions are shown for the preceding strain increment of $\Delta\gamma$=0.2. Three pebbles are labelled A to C. At γ=4.5 they form a cluster, which has disintegrated at γ=6. Pebbles A and B form a cluster again at γ=6.6. The sense of shear is top to the right.

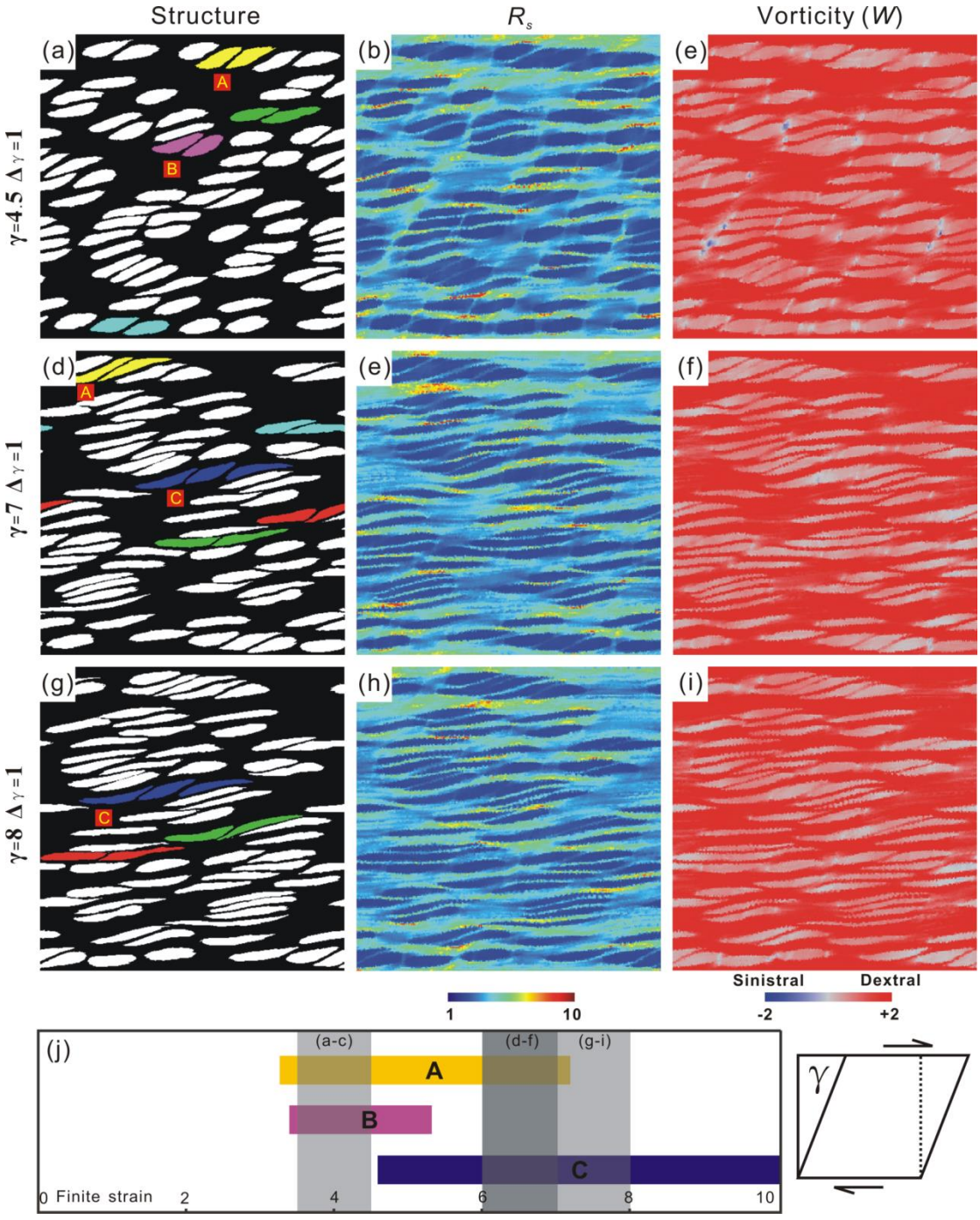

Fig.7. Evolution of deformable clusters in simulation $30\%^{n3}_{R\eta 2}$ (Appendix A, Movie 3). Pebble and matrix (black) distribution is shown at **(a)** γ=4.5, **(d)** at γ=7 and **(g)** γ=8. Pebbles belonging to a cluster are coloured. Incremental strain (R_s; **b, e, h**) and vorticity (W; **c, f, i**) distributions are shown for the preceding strain increment of $\Delta\gamma$=1. Three clusters are labelled A to C. The life span of these clusters with increasing finite strain is shown in **(j)**. The sense of shear is top to the right.

4. Discussion

4.1 Pebble deformation

Passive, deformable and rigid behaviour of pebbles are observed in our simulations with different $R\eta$ and for different C (Fig. 2). For a given C value, decreasing $R\eta$ enhances pebble deformation (Figs. 2, 3). This is consistent with previous studies, which suggest that the deformation behaviour of inclusions is strongly influenced by $R\eta$ (e.g., Gay, 1968; Bilby and Kolbuszewski, 1977; Lisle et al., 1983; Treagus and Treagus, 2001; Mandal et al., 2003; Takeda and Griera, 2006; Jiang, 2013; Qu et al., 2016). In our simulations, pebble concentration (C) is another important factor. In models with high C closely spaced pebbles interact with their neighbours, thus enhancing their deformation (Figs. 2, 3). In both cases of linear and power-law viscous rheologies, the effect of increasing C is similar to a decrease of $R\eta$, and *vice versa*. The pebbles deform as if they are "softer" in models with higher C. An increase in C and pebble interaction slightly reduce the mean rotation rate of rigid pebbles, which is consistent with previous studies (Fig. 4; Ildefonse et al., 1992a,b; Samanta et al., 2003; Marques et al., 2014). However, variation in pebble rotation rate increases with increasing C (Fig. 4).

Previous studies have suggested that an isolated inclusion at $R\eta >$ ca. 20-50 deforms rigidly if rheology is linear viscous, even at high finite strain (Gay, 1968; Bilby et al., 1975; Weijermars, 1993; Treagus and Treagus, 2001). Our simulations with n=1 show that pebbles in simulations with high viscosity ratios ($R\eta \geq 15$) behave rigidly when the inclusion concentration is low (C=10%) with minor interactions between neighbour pebbles. However, at a high C of 45%, pebbles interact with their neighbours and are deformable even at $R\eta$=45. The reported boundary between deformable and rigid from $R\eta$=10-50 is thus confirmed by our simulations, with the lower end representing isolated inclusions and the higher end closely packed inclusions. According to Bilby and Kolbuszewski (1977), a single inclusion behaves passively at $R\eta \leq 2$ for a linear viscous rheology. This is supported by our results for C=10%. Again,

raising the pebble concentration also raises the transition $R\eta$, here up to about 5 for C=45% (Fig. 2b). Similar trends are found for a power-law rheology with n=3 (Fig. 2a).

The range of $R\eta$ for deformable pebbles is quite narrow, between 2 and 15 for n=1 and C=10%, and at higher C still within one or two orders of magnitude. However, in the strict definition, all inclusions are deformable when not perfectly rigid. In practice, it is difficult to determine whether natural pebbles exhibited perfectly passive or rigid behaviour. We therefore use three fields in the mean R_f-ϕ plot (Fig. 8) based on the structures shown in Fig. 2 and the data in Fig. 3: (i) effectively passive, (ii) deformable and (iii) effectively rigid. Effectively passive pebbles stretch significantly and achieve an average aspect ratio (R_f) of $\geq$ 20 at high finite strain ($\gamma \geq 10$). Because of the strong stretching, there is no discernable deflection or wrapping of a foliation (if present) around the pebbles. Effectively rigid pebbles maintain an average aspect ratio (R_f) of less than about two, even at high finite strains. Any developing foliation would show strong deflections around the nearly equidimensional pebbles. Deformable pebbles occupy the field in between the previous two in Fig. 8. Pebbles are visible stretched, but a foliation would still be deflected around the pebbles, indicating even higher strains in the matrix. The field for deformable pebbles can be divided into two: pulsating behaviour (cyclical stretching and ongoing rotation at high $R\eta$ and/or low C) and permanently stretching (low $R\eta$ and/or high C).

In simple shear, initially approximately equidimensional pebbles follow trajectories in R_f -ϕ space, starting from around R_f=1 and ϕ=45 ° and moving towards one of the two fabric attractors with increasing strain. R_f and ϕ values can be measured in naturally deformed pebbles and their means can be plotted in the R_f -ϕ graph to gain an estimate of their type of behaviour and the amount of strain, in case of permanently stretching pebbles. An example is given further below.

Effectively passive and deformable pebbles in deformed conglomerates are the most important and thus most widely investigated, as their shape fabrics can be used for strain

analysis and rheology studies (e.g., Gay, 1968; Lisle et al., 1985; Treagus and Treagus, 2002; Czeck et al., 2009). In our simulations, for a given $R\eta$, an increasing C enhances the aspect ratios (R_f) of pebbles but reduces their rotation (Figs. 3, 4; Ildefonse et al., 1992a,b; Samanta et al., 2003; Mandal et al., 2004; Marques et al., 2014). Our simulations allow comparison with existing models for the evolution of mean R_f as a function of strain (R_s), such as the equation proposed by Gay (1968):

$$\ln(R_f) = \frac{5\cdot\ln(R_s)}{2R\eta_{Gay}+3} \Leftrightarrow R\eta_{Gay} = \frac{2.5\cdot\ln(R_s)}{\ln(R_f)} - 1.5, \qquad (3)$$

where $R\eta_{Gay}$ is the calculated apparent viscosity ratio.

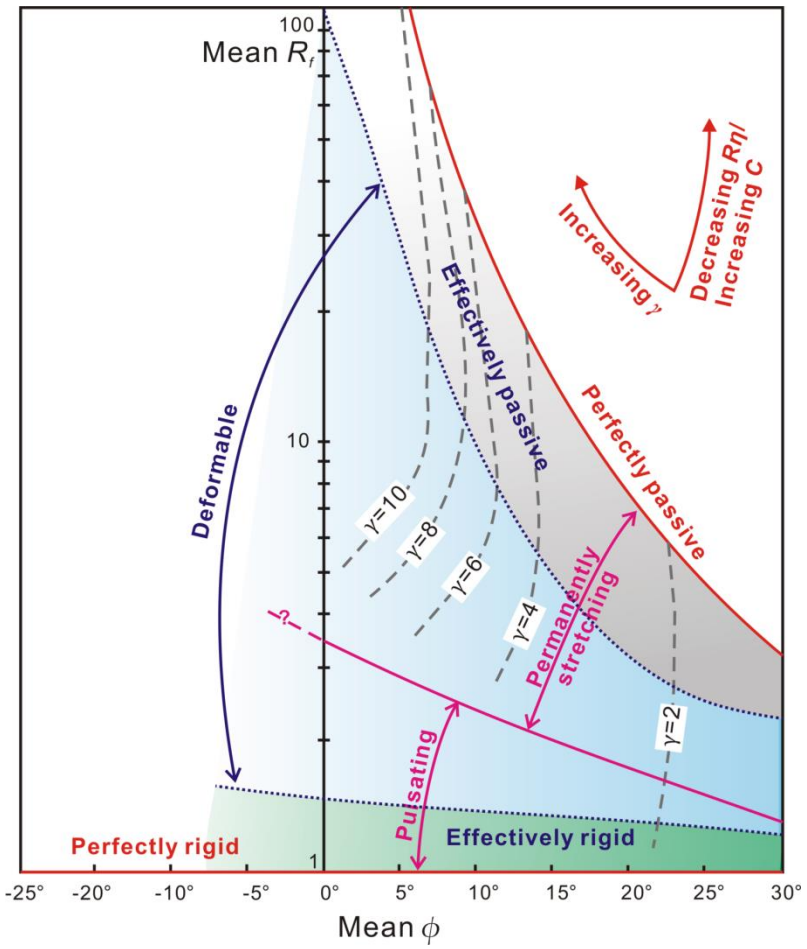

Fig. 8. Mean R_f-ϕ plot for deformed conglomerates with different viscosity ratios ($R\eta$) and concentrations (C). Perfectly passive and rigid behaviours are shown as solid red lines. The solid pink

line separates the pulsating and permanently stretching deformation behaviour. Dark blue dashed lines separate effectively passive, deformable and effectively rigid behaviours. Sub-vertical dashed lines are contours of the bulk finite strain (γ).

Another solution proposed by Bilby et al. (1975) is also widely accepted for the calculation of strain and viscosity ratio. However, Treagus and Treagus (2002) showed no distinct difference between the equations of Gay (1968) and Bilby et al. (1975) and suggested to use Gay's (1968) equation for practical geological applications, which we also use here. It should be noted that Eq. (3) applies to a linear viscosity only. However, it may also serve to gain insight in the apparent viscosity contrast for cases where $n \neq 1$.

Figure 9a compares our simulations with the R_f-strain curves from Gay (1968). The development of shape fabrics of pebbles is different from the predictions using Gay's (1968) theory for single inclusion in linear viscous rheology. Most of our results show larger R_f-values with increasing finite strain than predicted with Eq. (3). Pebble concentration has a critical effect on shape fabrics in our simulations, especially at high finite strain. For low C=10%, the shape development is similar to that in Gay's (1968) theory at low finite strain ($R_s < 10$). However, the simulations show an increasing deviation from the corresponding theoretical solution at middle to high finite strain ($R_s > 10$), even for a very low C (10%).

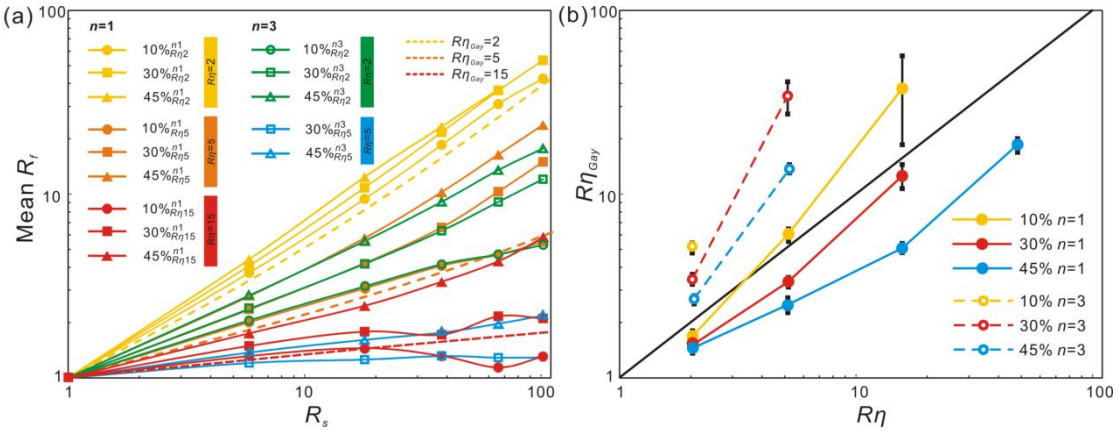

Fig. 9. (a) Variation of mean aspect ratios (R_f) with increasing finite strain (R_s) for simulations with

different pebble concentrations and $R\eta$ for both linear (n=1, red to orange) and power-law (n=3, blue to green) rheologies. Our simulations are represented by the solid lines with data points and Gay's (1968) prediction as dashed lines. **(b)** Comparison of viscosity ratios ($R\eta$) and calculated viscosity ratios ($R\eta_{Gay}$) using Eq. (3). Most n=1 data lie below the black $R\eta$=$R\eta_{Gay}$-line, indicating that Eq. (3) tends to underestimate the viscosity contrast, especially at higher pebble concentrations.

We use Eq. (3) to calculate apparent viscosity ratios ($R\eta_{Gay}$) and compare these with the known $R\eta$ in our simulations (Fig. 9b). For n=1 and C=10%, $R\eta_{Gay}\approx R\eta$ within error. However, at higher C, but same $R\eta$, pebbles deform more with the result that Gay's (1968) solution tends to underestimate the true viscosity ratio ($R\eta$). The concept of an apparent viscosity ratio could potentially be used for power-law rheologies, where Fig. 9b gives $R\eta_{Gay}>R\eta$ for n=3. However, we did not find a consistent relationship between $R\eta$ and $R\eta_{Gay}$.

4.2 Nature of pebble clusters

In some simulations with rigid and deformable pebble behaviour, closely spaced pebbles form a cluster that behaves as a single pebble, resulting in low strain rate and consistent vorticity within the cluster (Figs. 6, 7). There are two types of clusters depending on their deformation behaviour: rigid and deformable clusters.

In rigid clusters, the pebbles rotate together and not relative to each other (Fig. 6). However, they do not survive long, as after a short deformation increment, strain begins to localise in the matrix between pebble clusters until the clusters break up. Figure 6 gives an example of the formation and disintegration of rigid clusters in the simulation $30\%^{n3}_{R\eta 10}$. Pebbles A, B and C form a cluster from a finite strain of γ=4 (Fig. 6a-c). There is no shearing of the matrix between them (Fig. 6b) and the pebbles and matrix in between together rotate at the same rate (Fig. 6c), which is similar to that of other individual pebbles in the model. This cluster survives until a finite strain of γ=4.6 is reached, at which point the cluster disintegrates and each pebble behaves independently (Fig. 6d-f). Pebbles A and B move towards each other again until they form a new cluster during the finite strain interval between γ=6.3 and 6.7 (Fig.

6g-i).

In Fig. 6, single pebbles rotate on average ca. 13.6 °over a finite strain increment of $\Delta\gamma$=0.5, whereas the cluster formed by pebbles A, B and C rotates over ca. 12.6 °from γ=4 to 4.5 ($\Delta\gamma$=0.5; Fig. 4). The rotation of the cluster is less than that of individual pebbles as well as the finite rotation according to Jeffery's (1922) analytical solution (14.3°). This is consistent with previous studies suggesting that clusters rotate more slowly than single pebbles (Ildefonse et al., 1992a; Jessell et al., 2009). However, cluster rotation is still within the range of individual pebble rotations. Considering the short-lived character of rigid clusters, our results suggest that the formation of rigid clusters does not strongly affect the rotation of pebbles at large finite strains.

Figure 7 gives an example of evolution of deformable clusters in the simulation $30\%^{n3}_{R\eta 2}$. Contrary to rigid clusters, clusters of deformable pebbles deform into shapes similar to those of isolated individual pebbles (Fig. 7). The strain distribution in some deformable clusters is heterogeneous, as is the case for isolated pebbles. Deformable clusters survive for longer strain increments, and some even persist until the end of the simulations (Fig. 7j). In Fig. 7, clusters A and B form at γ=3.2 and 3.4, and collapse at γ=5.4 and 7.2, respectively (Fig. 7.a-f,j). There is no shearing of the matrix between them (Fig. 7b,c) and the pebbles and matrix in between deform jointly at the same rate (Fig. 7b). However, cluster C forms at γ=4.6 and remains up to γ=10 (Fig. 7g-j). Deformable isolated pebbles and clusters rotate rapidly towards the shear direction and then keep on elongating with minor further rotation in response to progressive deformation. The slow rotation facilitates the stability of deformable clusters, as opposed to rigid-pebble clusters.

Our observations can be compared with the models proposed by Tikoff and Teyssier (1994). They suggested three models of trains (clusters) based on Jeffery's (1922) and March's (1932) theories: (1) Jeffery-rotating train model, (2) March-rotating train model and (3) March-fixed train model. In the Jeffery-rotating train model, both inclusions and trains rotate rigidly

according to Jeffery's (1922) theory, and trains are short-lived (cf. Fig. 6). In the March-rotating train and the March-fixed train models, it is assumed that there is slip at the interface between inclusions and matrix and the shear localisation takes place around the inclusions. Inclusions rotate according to March's (1922) theory for passive markers and are not allowed to rotate past the shear plane. Trains persist for longer deformation increments in the March-rotating train model, whereas trains remain fixed in the March-fixed train model. The behaviour of rigid clusters (Fig. 6) in our simulations is consistent with the Jeffery-rotating train model. Our deformable clusters are present for longer deformation increments (Fig. 7), which is similar to the March-rotating and the March-fixed train models, even though our simulations do not allow slip along the pebble boundaries.

5. A natural example from the North China Craton

Our simulation results are compared with deformed Proterozoic conglomerates in the Hutuo Group, North China Craton. The Hutuo group is exposed in the Wutai Mountains area, in the Trans-North China Orogen (TNCO), where the Eastern and Western Blocks of the North China Craton collided at ~2.5 or ~1.85 Ga (e.g., Zhao et al., 2001; Li and Kusky, 2007; Fig. 10a,b). The group is divided into three subgroups: the Doucun, Dongye and Guojiazhai subgroups from base to top (Bai, 1986). The deformed conglomerates have been interpreted as basal conglomerates at the base of Doucun Subgroups, which unconformably overlay the Wutai Group and Neoarchean granitoids and were deposited after ~ 2.2 or ~1.9 Ga (e.g., Bai, 1986; Zhang et al., 2012; Du et al., 2017).

In the Yangjiaogou area, the deformed conglomerates mainly consist of pebbles composed of deformed banded-iron formations (BIFs) embedded in a foliated greenschist matrix (Fig. 10c,d). Matrix-supported conglomerates with a pebble concentration of about 7% appear strongly deformed with limited interactions between pebbles. Pebbles are visible stretched, but the foliation in the matrix is deflected around the pebbles. We therefore classify the pebbles as deformable. Asymmetric structures, such as sigmoidal pebbles and

delta-clast-shaped rolling structures indicate top-to-SW shearing (Fig. 10c). The stretching direction of boudinage quartz veins, which is oblique to the shear plane, also suggests a top-to-SW shearing (Fig. 10c). Although the exact kinematic vorticity of deformation could not be determined, we assume here that deformation was approximately simple shear because of the consistent asymmetry and sense of shear of all structures.

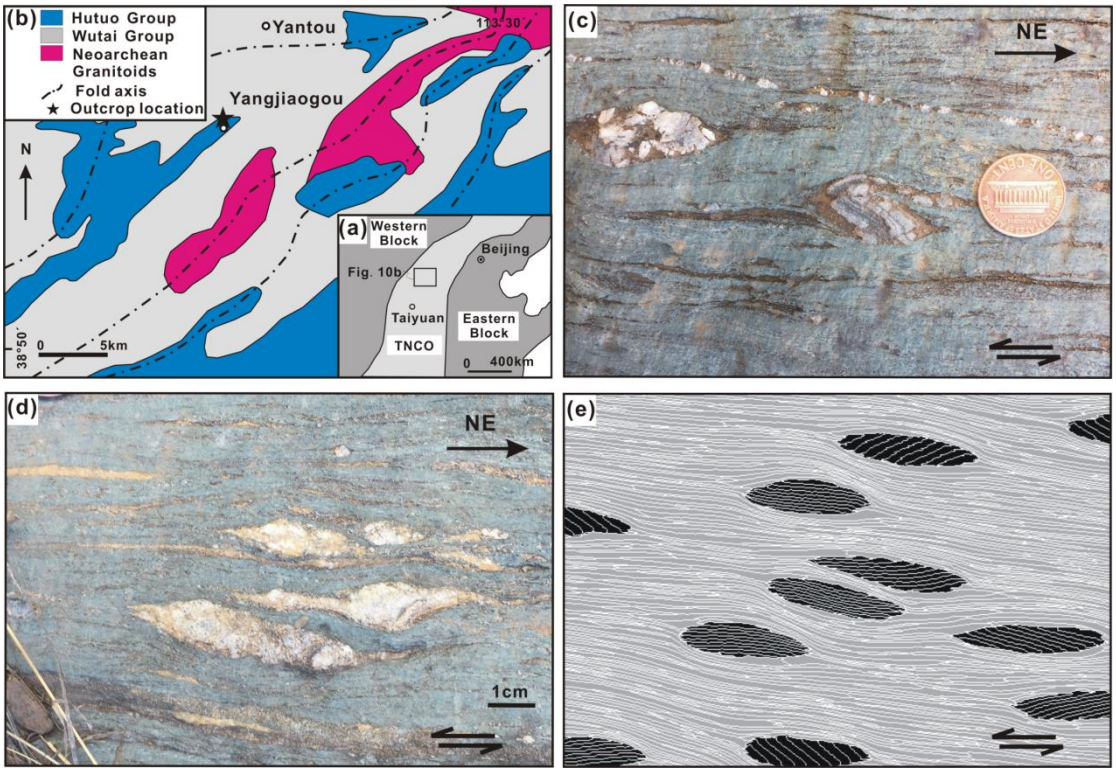

Fig. 10. Deformed conglomerates in the North China Craton compared with our simulation. **(a)** Tectonic subdivision of the North China Craton (modified after Zhao et al., 2005). TNCO is the Trans-North China Orogen. **(b)** Simplified geological map of the Yangjiaogou area and location of the outcrop with deformed Hutuo Group conglomerates. **(c)** Rolling structure and a boudinaged quartz vein indicating top-to-the-left sinistral simple shear. The ratio between final and initial length of boudinage quartz vein is estimated at ca. 2.3. The diameter of the 1 dollar-cent coin is 19mm. **(d)** and **(e)** Interactions between pebbles in outcrop compared with our simulation $10\%^{n1}_{vr5}$ at a finite strain of eight.

We use the geometries of boudinaged quartz veins to estimate the amount of shear strain,

using equations B.12 and 13b' of Ramsay and Huber (1987). The calculated finite strain is either 3.7 or 8.7 depending on the initial orientation of the vein (ca. 22 ° or −22 °) (see Appendix B for more details of the calculation). The formation of rolling structures (Fig. 10c) requires a significant rotation of pebbles of ≥150 ° at high finite strain. Together with the deflection of the foliation around the pebbles, this suggests that the finite strain is ca. 8.7, and not ca. 3.7. A low R_f of ~3.4 and an orientation of long-axes (ϕ) nearly parallel to the shear plane (ϕ≈2.9°) was obtained from an analysis of 82 pebbles. The measurements and structures can be compared with our simulations with 10% pebble concentration characterized by minor interactions and the deflected foliation around pebbles (Fig. 10d,e). The mean of ϕ is consistent with that in simulation $10\%^{n1}_{R\eta5}$ (Appendix A, Movie 1) at a finite strain of 8 to 10, whereas the mean of aspect ratios (R_f) is lower than that in simulation $10\%^{n1}_{R\eta5}$ at a finite strain of 8 to 10, thus suggesting a higher viscosity ratio (Fig. 11). An additional simulation, ($10\%^{n1}_{R\eta8}$) with C=10% pebbles and a lower viscosity ratio ($R\eta$=8) in linear rheology (n=1), was run for comparison with the deformed conglomerates in the Yangjiaogou area (Fig. 11). According to our R_f-ϕ plot (Fig. 8), we suggest that the viscosity ratio of deformed conglomerates in the Yangjiaogou area is 5 to 8 for a linear rheology (n=1) and 2 to 5 for a power-law rheology (n=3). The plot also suggests a finite strain of γ≈6, close to the γ≈8.7 derived from the strain analysis on the boudinaged vein.

The example from the Wutai Mountains shows that the graphs obtained from our simulations may aid to quantify the amount of deformation with relatively simple R_f and ϕ measurements. Not only does one obtain an estimate of the finite strain, but also insight in the relative rheological properties of the lithologies involved.

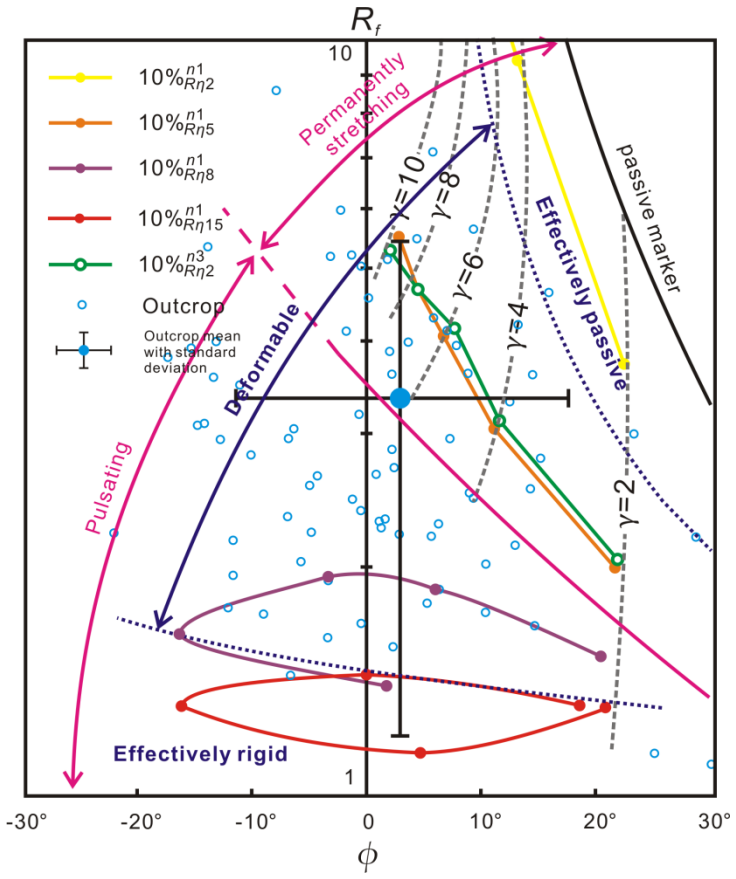

Fig. 11. Mean R_f-ϕ plot for comparing the outcrop data (with one standard deviation error bars) of deformed conglomerates in the Yangjiaogou area compared with our simulations at different finite strains (γ) plotted on the graph of Fig. 8.

6. Conclusions

We use numerical simulations to model the viscous simple-shear deformation of conglomerates with different degrees of interaction between pebbles, by varying the concentration of pebbles and viscosity ratio between pebbles and matrix, in both linear and power-law viscous rheologies. Our results lead to the following conclusions:

1. Pebbles can behave as rigid, deformable and passive inclusions depending on both the viscosity ratio and their concentration (volume fraction of pebbles).

2. The effect of increasing pebble concentration is similar to a decrease of viscosity ratio

between pebbles and matrix, and *vice versa*. An increase in concentration and interaction enhances the pebble distortion, but reduces the mean rotation of rigid pebbles.

3. Clusters of closely spaced pebbles can behave as single objects. Rigid clusters continue rotating, but survive for only a short strain interval. Deformable clusters initially rotate rapidly towards the shear direction, and then keep on elongating with minor rotation. The slower rotation facilitates the stability of deformable clusters.

4. A mean R_f -ϕ plot is suggested to gain an estimate of pebble deformation behaviour and the amount of strain in cases of permanently stretching pebbles.

5. A case study on deformed conglomerates of the Hutuo Group, North China Craton, illustrates the use of the mean R_f -ϕ plot, giving an estimate of the finite strain and viscosity contrast between pebbles and matrix.

Acknowledgments

Fieldwork in the Wutai Mountains area, China was supported by the China Geological Survey (grant No. 12120114076401). We appreciate the help for the field work from Zhongbao Zhao, Changshun Wen, Chao Li and Gongyao Xu and the constructive suggestions from Guoli Yuan, Zhongbao Zhao and Changshun Wen. HR thanks the financially support by the China Scholarship Council (CSC; No. 201506400014). EGR acknowledges the support of the Beatriu de Pinós programme of the Government of Catalonia's Secretariat for Universities and Research of the Department of Economy and Knowledge (2016 BP 00208). We thank two anonymous reviewers for their constructive comments.

References

Bai, J., 1986. The early Precambrian geology of Wutaishan. Tianjin Science and Technology Press, Tianjin.

Bilby, B.A., Eshelby, J.D., Kundu, A.K., 1975. The change of shape of a viscous ellipsoidal region embedded in a slowly defomring matrix having a different viscosity. Tectonophysics 28, 265-274.

Bilby, B.A., Kolbuszewsk, M.L., 1977. The finite deformation of an inhomogeneous in two-dimensional slow viscous incompressible flow. Proceedings of the Royal Society A355, 335-353.

Blumenfeld, P., Bouchez, J.-L., 1988. Shear criteria in granite and migmatitc deformed in magmatic and solid state. Journal of Structural Geology 10, 361-372.

Bons, P.D., Cox, S.J.D. 1994. Analogue experiments and numerical modelling on the relation between microgeometry and flow properties of polyphase materials. Materials Science and Engineering A175, 237-245.

Bons, P.D., Koehn, D., Jessell, M.W. (Eds), 2008. Microdynamics Simulation. In: Lecture Notes in Earth Sciences 106. Springer, Berlin.

Czeck, D.M., Fissler, D.A., Horsman, E., Tikoff, B., 2009. Strain analysis and theology contrasts in polymictic conglomerates: An example from the Seine metaconglomerates, Superior Province, Canada. Journal of Structural Geology 31, 1365-1376.

Czeck, D.M., Hudleston, P.J., 2003. Testing models for obliquely plunging lineations in transpression: a natural example and theoretical discussion. Journal of Structural Geology 25, 959-982.

Dabrowski, M., Krotkiewski, M., Schmid, D.W., 2008. MILAMIN: MATLAB-based finite element method solver for large problems. Geochem. Geophys. Geosyst. 9, Q04030, doi:10.1029/2007GC001719.

Dabrowski, M., Schmid, D.W., Podladchikov, Y.Y., 2012. A two-phase composite in simple shear: Effective mechanical anisotropy development and localization potential. Journal of Geophysical Research 117, B08406, doi:10.1029/2012JB009183.

Du, L., Yang, C., Wyman, D.A., Nutman, A.P., Zhao, L., Lu, Z., Song, H., Geng, Y., Ren, L., 2017. Zircon U-Pb ages and Lu-Hf isotope compositions from clastic rocks in the Hutuo Group: Further constraints on Paleoproterozoic tectonic evolution of the Trans-North

China Orogen. Precambrian Research 303, 291-314.

Dunnet, D., 1969. A technique of finite strain analysis using elliptical particles. Tectonophysics 7, 117-136.

Eshelby, J.D., 1957. The determination of the elastic field of an ellipsoidal inclusion, and related problems. Proceedings of the Royal Society A241, 376-396.

Fletcher, R.C., 2004. Anisotropic viscosity of a dispersion of aligned elliptical cylindrical clasts in viscous matrix. Journal of Structural Geology 26, 1977-1987.

Flinn, D., 1956. On the deformation of the Funzie conglomerate, Fetlar, Shetland. The Journal of Geology 64, 480-505.

Freeman, B., Lisle, R.J., 1987. The relationship between tectonic strain and the three-dimensional shape fabrics of pebbles in deformed conglomerates. Journal of the Geological Society 144, 635-639.

Fry, N., 1979. Random point distributions and strain measurement in rocks. Tectonophysics 60, 89-105.

Gardner, R., Piazolo, S., Evans, L., Daczko, N., 2017. Patterns of strain localization in heterogeneous, polycrystalline rocks–a numerical perspective. Earth and Planetary Science Letters 463, 253-265.

Gay, N.C., 1968. Pure shear and simple shear deformation of inhomogeneous viscous fluids. 1. Theory. Tectonophysics 5, 211-234.

Griera, A., Bons, P. D., Jessell, M. W., Lebensohn, R. A., Evans, L., Gomez-Rivas, E., 2011. Strain localization and porphyrocalst rotation. Geology 39, 275-278.

Griera, A., Llorens, M.-G., Gomez-Rivas, E., Bons, P. D., Jessell, M. W., Evans, L. A., Lebensohn, R., 2013. Numerical modelling of porphyroclast and porphyroblast rotation in anisotropic rocks. Tectonophysics 587, 4-29.

Ildefonse, B., Launeau, P., Bouchez, J.L., Fernandez, A., 1992a. Effect of mechanical interactions on the development of shape preferred orientations: a two-dimensional experimental approach. Journal of Structural Geology 14, 73-83.

Ildefonse, B., Sokoutis, D., Mancktelow, N.S., 1992b. Mechanical interactions between rigid particles in a deforming ductile matrix. Analogue experiments in simple shear flow. Journal of Structural Geology 14, 1253-1266.

Jansen, D., Llorens Verde, M.-G., Westhoff, J., Steinbach, F., Kipfstuhl, S., Bons, P.D., Griera, A., Weikusat, I., 2016. Small-scale disturbances in the stratigraphy of the NEEM ice core: observations and numerical model simulations. The Cryosphere 10, 359-370.

Jeffery, J.B., 1922. The motion of ellipsoidal particles immersed in viscous fluid. Proceedings of Royal Society London A102, 161-179.

Jessell, M., Bons, P.D., Evans, L., Barr, T., Stüwe, K., 2001. Elle: the numerical simulation of metamorphic and deformation microstructures, Computers & Geosciences 27, 17-30.

Jessell, M.W., Bons, P.D., Griera, A., Evans, L.A., Wilson, C.J.L., 2009. A tale of two viscosities. Journal of Structural Geology 31, 719-736.

Jessell, M.W., Siebert, E., Bons, P.D., Evans, L., Piazolo, S., 2005. A new type of numerical experiment on the spatial and temporal patterns of localization of deformation in a material with a coupling of grain size and rheology. Earth and Planetary Science Letters 239, 309-326.

Jiang, D., 2007a. Numerical modeling of the motion of deformable ellipsoidal objects in slow viscous flows. Journal of Structural Geology 29, 435-452.

Jiang, D., 2007b. Numerical modeling of the motion of rigid ellipsoidal objects in slow viscous flows: A new approach. Journal of Structural Geology 29, 189-200.

Jiang, D., 2013. The motion of deformable ellipsoids in power-law viscous materials: Formulation and numerical implementation of a micromechanical approach applicable to flow partitioning and heterogeneous deformation in Earth's lithosphere. Journal of Structural Geology 50, 22-34.

Jiang, D., Bentley, C., 2012. A micromechanical approach for simulating multiscale fabrics in large-scale high-strain zones: Theory and application. Journal of Geophysical Research 117, B12201, doi:10.1029/2012JB009327.

Johnson, S.E., Lenferink, H.J., Marsh, J.H., Price, N.A., Koons, P.O., West Jr., D.P., 2009a.

Kinematic vorticity analysis and evolving strength of mylonitic shear zones: New data and numerical results. Geology 37, 1075-1078.

Johnson, S.E., Lenferink, H.J., Price, N.A., Marsh, J.H., Koons, P.O., West Jr., D.P., Beane, R., 2009b. Clast-based kinematic vorticity gauges: the effects of slip at matrix/clast interfaces. Journal of Structural Geology 31, 1322-1339.

Kaus, B., 2010. Factors that control the angle of shear bands in geodynamic numerical models of brittle deformation. Tectonophysics 484, 36-47.

Lebensohn, R.A., 2001. N-site modeling of a 3D viscoplastic polycrystal using Fast Fourier Transform. Acta Materialia 49, 2723-2737.

Lebensohn, R.A., Idiart, M., Castañeda, P.P., Vincent, P.-G., 2011. Dilatational viscoplasticity of polycrystalline solids with inter-granular cavities. Philosophical Magazine 91, 3038-3067.

Lebensohn, R.A., Montagnat, M., Mansuy, P., Duval, P., Meysonnier, J., Philip, A., 2009. Modeling viscoplastic behavior and heterogeneous intracrystalline deformation of columnar ice polycrystals. Acta Materialia 57, 1405-1415.

Li, J.H., Kusky, T.M., 2007. A late Archean foreland fold and thrust belt in the North China Craton: Implications for early collisional tectonics. Gondwana Research 12, 47-66.

Lisle, R.J., 1977. Estimation of the tectonic strain ratio from the mean shape of deformed elliptical markers. Geologie en Mijnbouw 56, 140-144.

Lisle, R.J., 1979. Strain analysis using deformed pebbles: the influence of initial pebble shape. Tectonophysics 60, 263-277.

Lisle, R.J., 1985. The use of the orientation tensor for the description and statistical testing of fabric. Journal of Structural Geology 7, 115-117.

Lisle, R.J., Rondeel, H.E., Doorn, D., Brugge, J., Van de Gaag, P., 1983. Estimation of viscosity contrast and finite strain from deformed elliptical inclusions. Journal of Structural Geology 5, 603-609.

Llorens, M.-G., Bons, P. D., Griera, A., Gomez-Rivas, E., 2013a. When do folds unfold during progressive shear?. Geology 41, 563-566.

Llorens, M.-G., Bons, P. D., Griera, A., Gomez-Rivas, E., Evans, L. A., 2013b. Single layer folding in simple shear. Journal of Structural Geology 50, 209-220.

Llorens, M.-G., Griera, A., Bons, P. D., Lebensohn, R., Evans, L., Jansen, D., Weikusat, I, 2016a. Full-field prediction of ice dynamic recrystallisation under simple shear conditions, Earth and Planetary Science Letters 450, 233-242.

Llorens, M.-G., Griera, A., Bons, P.D., Roessiger, J., Lebensohn, R., Evans, L., Weikusat, I., 2016b. Dynamic recrystallisation of ice aggregates during co-axial viscoplastic deformation: a numerical approach. Journal of Glaciology 62, 359-377.

Mancktelow, N.S., 2002. Finite-element modelling of shear zone development in viscoelastic materials and its implications for localisation of partial melting. Journal of Structural Geology 24, 1045-1053.

Mancktelow, N.S., 2011. Deformation of an elliptical inclusion in two-dimensional incompressible power-law viscous flow. Journal of Structural Geology 33, 1378-1393.

Mandal, N., Misra, S., Samanta, S.K., 2004. Role of weak flaws in nucleation of shear zones: an experimental and theoretical study. Journal of Structural Geology 26, 1391-1400.

Mandal, N., Samanta, S.K., Bhattacharyya, G., Chakraborty, C., 2003. Deformation of ductile inclusions in a multiple inclusion system in pure shear. Journal of Structural Geology 25, 1359-1370.

Mandal, N., Samanta, S.K., Bhattacharyya, G., Chakraborty, C., 2005. Rotation behaviour of rigid inclusions in multiple association: insights from experimental and theoretical models. Journal of Structural Geology 27, 679-692.

March, A., 1932. Mathematische Theorie der Regelung nach der Korngestalt bei affiner Deformation. Zeitschrift für Kristallographie 81, 285-297.

Marques, F.O., Bose, S., 2004. Influence of a permanent low-friction boundary on rotation and flow in rigid inclusion/viscous matrix systems from an analogue perspective. Tectonophysics 382, 229-245.

Marques, F.O., Mandal, N., Taborda, R., Antunes, J.V., Bose, S., 2014. The behaviour of deformable and non-deformable inculsions in viscous flow. Earth-Science Reviews 134,

16-69.

Means, W.D., Hobbs,B.E., Lister, G.S., Williams, P.F., 1980. Vorticity and non-coaxiality in progressive deformations. Journal of Structural Geology 2, 371-378.

Montagnat, M., Castelnau, O., Bons, P.D., Faria, S.H., Gagliardini, O., Gillet-Chaulet, F., Grennerat, F., Griera, A., Lebensohn, R.A., Moulinec, H., Roessiger, J., Suquet, P., 2014. Multiscale modeling of ice deformation behavior. Journal of Structural Geology 61, 78-108.s

Passchier, C.W., Trouw, R.A.J., 2005. Microtectonics. Springer, Berlin.

Piazolo, S., Jessell, M.W., Bons, P.D., Evans, L., Becker, J.K. 2010. Numerical simulations of microstructures using the Elle platform: A modern research and teaching tool. Journal of the Geological Society of India 75, 110-127.

Piazolo, S., Passchier, C.W., 2002. Experimental modeling of vicous inclusions in a circular high strain shear rig: Implications for the interpretation of shape fabrics and deformed enclaves. Journal of Geophysical Research 107, B10242, doi: 10.1029/2000JB000030.

Pouryazdan, M., Kaus, B.J.P., Rack, A., Ershov, A., Hahn, H., 2017. Mixing instabilities during shearing of metals. Nature Communications 8, 1611, doi: 10.1038/s41467-017-01879-5.

Qu, M., Jiang, D., Lu, L.X., 2016. An optimal scheme for numerical evaluation of Eshelby tensors and its implementation in a MATLAB package for simulating the motion of viscous ellipsoids in slow flows. Computers & Geosciences 96, 98-108.

Ramsay, J.G., Huber, M.I., 1983. The techniques of modern structural geology, Volume 1: Strain Analysis. Academic Press, London.

Ramsay, J.G., 1967. Folding and Fracturing of Rocks. McGraw-Hill, New York.

Ran, H., de Riese, T., Llorens, M.-G., Finch, M.A., Evans, L.A., Gomez-Rivas, E., Griera, A., Jessell, M.W., Lebensohn, R.A., Piazolo, S., Bons, P.D., 2018. Time for anisotropy: The significance of mechanical anisotropy for the development of deformation structures. Journal of Structural Geology. Doi: 10.1016/j.jsg.2018.04.019.

Räss, L., Duretz, T., Podladchikov Y. Y., Schmalholz S. M., 2016. M2Di: Concise and efficient MATLAB 2-D Stokes solvers using the Finite Difference Method. Geochemistry, Geophysics and Geosystems 18, 755-768.

Rosenberg, C.L., 2001. Deformation of partially molten granite: a review and comparison of experimental and natural case studies. International Journal of Earth Sciences 90, 60-76.

Samanta, S.K., Bhattacharyya, G., 2003. Modes of detachment at the inclusion-matrix interface. Journal of Structural Geology 25, 1107-1120.

Schneider C.A., Rasband W.S., Eliceiri K.W., 2012. NIH Image to ImageJ: 25 years of image analysis. Nature Methods 9, 671-675.

Steinbach F., 2017. Numerical modelling of deformation and recrystallisation mechanics in ice and ice-air aggregates. Unpublished Ph.D. thesis, Eberhard Karls University Tübingen.

Steinbach F., Bons, P.D., Griera A., Jansen, D., Llorens M.-G., Roessiger, J., Weikusat I., 2016. Strain localization and dynamics recrystallisation in the ice-air aggregate: A numerical study. The Cryosphere 10, 3071-3089.

Takeda, Y.T., Griera, A., 2006. Rheological and kinematical responses to flow of two-phase rocks. Tectonophysics 427, 95-113.

Tikoff, B., Teyssier, C., 1994. Strain and fabric analysis based on porphyrocalst interaction. Journal of Structural Geology 16, 477-491.

Treagus, S.H., 2002. Modelling the bulk viscosity of two-phase mixtures in terms of clast shape. Journal of Structural Geology 24, 57-76.

Treagus, S.H., 2003. Viscous anisotropy of two-phase composites, and application to rocks and structures. Tectonophysics 372, 121-133.

Treagus, S.H., Lan, L., 2003. Simple shear of deformable square objects. Journal of Structural Geology 25, 1993-2003.

Treagus, S.H., Lan, L., 2004. Deformation of square objects and boudins. Journal of Structural Geology 26, 1361-1376.

Treagus, S.H., Treagus, J.E., 2001. Effects of object ellipticity on strain, and implications for

clast-matrix rocks. Journal of Structural Geology 23, 601-608.

Treagus, S.H., Treagus, J.E., 2002. Studies of strain and rheology of conglomerates. Journal of Structural Geology 24, 1541-1567.

Vitale, S., Mazzoli, S., 2005. Influence of object concentration on finite strain and effective viscosity contrast: insights from naturally deformed packstones. Journal of Structural Geology 27, 2135-2149.

Weijermars, R., 1993. Pulsating strains. Tectonophysics 220, 51-67.

Yin, A., Harrison, T.M., Murphy, M.A., Grove, M., Nie, S., Ryerson, F.J., Wang, X.F., Chen, Z.L., 1999. Tertiary deformation history of southeastern and southwestern Tibet during the Indo-Asian collision. Geological Society of America Bulletin 111, 1644-1664.

Zhang, J., Zhao, G., Li, S., Sun, M., Chan, L. S., Shen, W., Liu, S., 2012. Structural pattern of the Wutai Complex and its constraints on the tectonic framework of the Trans-North China Orogen. Precambrian Research 222, 212-229.

Zhao, G.C., Sun, M., Wilde, S.A., Li, S.Z., 2005. Late Archean to Paleoproterzoic evolution of the North China Craton: key issues revisited. Precambrian Research 136, 177-202.

Zhao, G.C., Wilde, S.A., Cawood, P.A., Sun, M., 2001. Archean blocks and their boundaries in the North China Craton: lithological, geochemical, structural and P–T path constraints and tectonic evolution. Precambrian Research 107, 45-73.

Appendix A

Movies of selected simulations, showing pebble and strain-rate distributions. Movie 1: $10\%_{R\eta5}^{n1}$, Movie 2: $45\%_{R\eta5}^{n1}$, Movie 3: $30\%_{R\eta2}^{n3}$, Movie 4: $30\%_{R\eta10}^{n3}$, Movie 5: $45\%_{R\eta2}^{n3}$.

Appendix B

The expression for the deformation of a linear marker under simple and pure shear in 2-D plane is given by Ramsay and Huber (1987; pp.283-286). We consider a line of unit length that joins coordinates (0, 0) and (*x*, *y*) and which has an angle α with the *x*-direction. After deformation, (*x*, *y*) is positioned at (*x'*, *y'*) and the line now has an angle α' with the axis and its length is now 1+*e*. We assume homogeneous finite strain, described with:

$$x' = ax + by$$

$$y' = cx + dy \qquad \text{(B1)}$$

where *a*, *b*, *c* and *d* are the elements of the position gradient tensor. For simple shear, the tensor is

$$\begin{vmatrix} a & b \\ c & d \end{vmatrix} = \begin{vmatrix} 1 & \gamma \\ 0 & 1 \end{vmatrix} \qquad \text{(B2)}$$

The equation for the reciprocal quadratic extension ($\lambda' = 1/(1+e)^2$) is given as:

$$\lambda' = \frac{\frac{1}{2}(d^2+c^2-a^2-b^2)\cos 2\alpha' - (ac-bd)\sin 2\alpha' + \frac{1}{2}(a^2+b^2+c^2+d^2)}{(ad-bc)^2}. \qquad \text{(B2)}$$

The relationship between α and α' is:

$$\tan\alpha = \frac{c - a\tan\alpha'}{b\tan\alpha' - d} \qquad \text{(B3)}$$

The ratio between stretching and initial length (*e*) of the boudinage quartz vein in Yangjiaogou area (Fig. 10c) is estimated at ca. 2.3 and the angle (α') between boudinage quartz vein and shear plane is ca. 9.1 °. Inserting these values into Eqs. (B2) and (B3) gives two solutions: γ=3.7 and α=22 °or γ=8.7 and α=-22 °.

Chapter 3

Folding within pebbles during ductile simple-shear deformation of conglomerates: a numerical approach

Hao Ran [a,b], Paul D. Bons [a], Genhou Wang [b], Albert Griera [c], Tamara de Riese [a], Gomez-Rivas Enrique [d,e], Maria-Gema Llorens [a,c], Shuming Ran [f], Yao Wang [g], Shubiao Wang [g]

[a] Department of Geosciences, Eberhard Karls University Tübingen, Tübingen, Germany

[b] School of Earth Sciences and Resources, China University of Geosciences, Beijing, China

[c] Departament de Geologia, Universitat Autònoma de Barcelona, Barcelona, Spain

[d] Department of Mineralogy, Petrology and Applied Geology, University of Barcelona, Barcelona, Spain

[e] School of Geosciences, King's College, University of Aberdeen, Aberdeen, UK

[f] Tianjin Center, China Geological Survey, Tianjin, China

[g] Liaoning GEO-Engineering Group Corporation, Shenyang, China

In preparation for submission to *Tectonophysics*.

Abstract

Folds within pebbles in conglomerates have been used to infer possible folding events before deposition of the conglomerate. However, it is not clear whether folds can develop within pebbles during deformation of conglomerates. We use the numerical modelling to investigate folding within internally layered pebbles in a ductile deformation up to a strain of eight in simple shear. We vary initial orientation and rheology of the layers, as well as the relative rheology of the conglomerate matrix, for single isolated pebbles and multiple, interacting pebbles in a power-law rheology. Folding within pebbles can occur, but is expected to be uncommon, as it only occurs within a narrow range of initial layer orientations and viscosity contrasts. Strongly deformed conglomerates from the Proterozoic Hutuo Group in the Wutai Mountains, North China Craton, contain a small percentage of pebbles with internal folds. We suggest that these formed during deformation of the conglomerate and do not represent inclusion into the unit of previously folded lithologies.

Keywords: Folding; conglomerate deformation; Hutuo Group; North China Craton

1. Introduction

Conglomerate deformation has been a subject of many studies in structural geology, in particular regarding tectonic evolution, strain determination and kinematics, deformation processes and rheology (Flinn, 1956; Ramsay, 1967; Lisle, 1985; Ramsay and Huber, 1983; Twiss and Moores, 1992; Treagus and Treagus, 2002; Vitale and Mazzoli, 2005; Czeck et al., 2009; Fossen, 2016). Pebbles can deform passively (i.e. their deformation rate approximately equals that of the matrix) and rigidly (i.e. they only undergo very minor deformation). In between these two end members, deformable behaviour is defined as those that deform significantly, but distinctly less than their surrounding matrix (Ran et al., 2018a). Deformed pebbles record both the deformation history of a conglomerate and that of the source rock from which the pebbles were derived. The internal structures of layered or foliated pebbles can provide information on deformation process (Druguet and Hutton, 1998; Xu et al., 2003; Du et al., 2012). Druguet and Hutton (1998) provided a case of crenulated foliations within xenoliths in deformed magmatic bodies at Cap de Creus, Spain, which is similar to folded layers within pebbles. They used these crenulations to infer that the xenoliths were incorporated into the magma during syntectonic intrusion of that magma. Du et al. (2012) suggested that the folds within banded-iron-formation (BIF) pebbles in deformed conglomerates of the Hutuo Group, North China Craton, indicate a D_1 deformation before the conglomerate was deposited. However, Zhang et al. (2012) argued that this D_1 event affected the conglomerate and produced the folds inside the pebbles. The different interpretations have profound consequences for the inferred tectonic history. In the first scenario, the BIFs of the Wutai Group underneath the Hutuo Group would have been buried and subjected to a folding event before erosion and sedimentation of the Hutuo Group conglomerates. In the second scenario, the Wutai Group BIFs would have been undeformed when incorporated as pebbles in the conglomerate, thus removing a whole burial and exhumation cycle and deformation event between the two groups. Therefore, it is necessary to understand correctly if, when and how folds within pebbles in deforming conglomerates form.

Many studies have addressed the deformation of inclusion-matrix systems, such as

conglomerates, investigating factors such as initial shape and concentration of inclusions, material properties, the behaviour of the interface between inclusion and matrix, etc. (Jeffery, 1922; Lisle, 1979; Rosenberg, 2001; Treagus and Treagus, 2001, 2002; Treagus, 2002; Mancktelow, 2002, 2011; Mandal et al., 2003, 2005; Marques and Bose, 2004; Takeda and Griera, 2006; Jiang, 2007a,b, 2013; Jiang and Bentley, 2012; Johnson et al., 2009a,b; Griera et al., 2011, 2013; Dabrowski et al., 2012; Räss et al., 2016). However, to our knowledge, little is still known of the development of internal structures, such as folds, within inclusions during deformation.

It is common that layered structures fold under ductile deformation. The development of folding is controlled by the viscosity contrast between layer(s) and matrix, mechanical anisotropy, thermal effects and other factors (e.g., Biot, 1961; Schmalholz and Podladchikov, 2001; Hobbs, et al., 2008; Llorens et al., 2013a,b; Ran et al., 2018b). Biot (1961) predicted that the fold wavelength increases with increasing viscosity contrast between the layer and matrix. Schmalholz and Podladchikov (2001) investigated the influence of viscosity contrast on single layer folding under pure shear in linear and power-law rheologies, based on analogue and numerical experiments. Llorens et al. (2013a,b) extended the pure-shear deformation to simple shear using a finite-element method. Folding in non-coaxial shear is more complicated in coaxial shear, as the developing fold train rotates relative to the applied stress field (Treagus, 1973; Ramsay and Hubber, 1983; Viola and Mancktelow, 2005; Llorens et al., 2013a,b). In simple shear, fold trains rotate towards the extensional field and stretch again, possibly straightening out again completely (Llorens et al., 2013a). This aspect of folding is expected to be even more important in deforming conglomerates as layer orientation inside pebbles would vary from pebble to pebble and pebbles rotate themselves depending on their shape, orientation and the kinematics of deformation.

Numerical modelling provides a method to simulate the viscous deformation of layered pebbles embedded in a matrix. The full-field, crystal-plasticity code VPFFT (Visco-Plastic Fast Fourier Transform) of Lebensohn (2001) and Lebensohn et al. (2009, 2011) coupled with

the ELLE software platform (Jessell et al., 2001; Bons et al., 2008; Piazolo et al., 2010; http://www.elle.ws) allows us to simulate geological processes achieving a high finite strain in linear or power-law rheology (Griera et al., 2011, 2013; Llorens et al., 2016a,b, 2017; Jansen et al., 2016; Steinbach et al., 2016, 2017; Gomez-Rivas et al., 2017; Ran et al., 2018a,b). In this study, we use the VPFFT+ELLE code to simulate high-strain viscous deformation of conglomerates with layered pebbles, varying the initial orientation of layers inside pebbles and the relative power-law viscous rheology of the hard and soft pebble layers, as well as that of the matrix. This study is restricted to simple-shear deformation, which we simulate up to a shear strain of eight. In addition, we provide a series of simulations of folding of a stack of alternating hard and soft layers to investigate the wavelength and amplitude as a function of viscosity ratio between the layers. Finally, we compare our numerical simulations with deformed conglomerates of the Hutuo Group in the North China Craton discussed above and provide an interpretation of folding within BIF pebbles.

2. Methods

2.1 The VPFFT+ELLE method

We use the open-source numerical modelling platform ELLE (Jessell et al., 2001; Bons et al., 2008; Piazolo et al., 2010; http://www.elle.ws), coupled with VPFFT code to calculate the stress, strain rate and resulting velocity field (Lebensohn, 2001; Lebensohn et al. 2009, 2011; Llorens et al. (2016b). The ELLE software handles the data structure, input and output and data visualisation (Bons et al., 2008). Most relevant previous studies that used this simulation software combination are Griera et al. (2011, 2013) and Ran et al. (2018a,b). The numerical approach we use here is as same as in Griera et al. (2011, 2013). We use a hexagonal symmetry model mineral to simulate the mechanical properties of the material, of which deformations by dislocation glide on the basal, pyramidal and prismatic planes. The resistance to shear of slip systems is calculated by means of the critical resolved shear stress (CRSS; τ). The same value is set for the different slip planes and, hence, all materials are effectively

isotropic (see Griera et al., 2013). The relation between differential stress (σ) and strain rate ($\dot{\varepsilon}$) of the material is defined by:

$$\dot{\varepsilon} = A\left(\frac{\sigma}{\tau}\right)^n, \qquad (1)$$

where A is a pre-exponential (scaling) factor, identical for all materials used in these simulations and n the stress exponent, set to n=3 here. We use the critical resolved shear stress (τ) to define the viscosity (η) of each phase. In all cases τ_{matrix}, and hence η_{matrix}, is set to unity. Hard and soft layers inside pebbles are equal to or more competent than the matrix by assigning them τ-values with $\eta_{hard}(\tau_{hard}) > \eta_{hard}(\tau_{soft}) \geq \eta_{matrix}(\tau_{matrix})$. We define the viscosity ratio $R\eta$ between soft and hard layers as $R\eta = \tau_{hard}/\tau_{soft}$. The meaning of viscosity ratio is not strictly the same as viscosity contrast for a linear, Newtonian rheology, as viscosity is not constant in power-law materials, depending on the partitioning of stress and strain rate.

The data structure of the models defined in ELLE consists of a contiguous set of polygons (termed *flynns*; Fig. 1a, c) and a set of unconnected nodes or Fourier points (termed *unodes*; Fig. 1b). The boundaries of *flynns* consist of straight segments connected by boundary nodes (termed *bnodes*; Fig. 1a, b) in either double- or triple-junctions. We use *flynns* to define single-phase regions, with the properties of either matrix, soft or hard layers within pebbles. A resolution of rectangular 256×256 *unodes* is used to store stress, strain rate and lattice orientation. The VPFFT code uses the *unodes* for calculation of viscoplastic deformation.

In this study, three series of simulations are presented, i.e. (i) multi-layer folding, and deformation of (ii) a single and (iii) multiple pebbles. Starting models are square with a unit-cell size of 1×2 for multi-layer folding model and a unit-cell size of 1×1 for single- and multi-pebble models. Layers in the pebbles have a width of 0.0078× the unit-cell size. Multi-layer models consist of 64 competent layers and 64 soft layers, the same as the layered pebbles. Single-pebble models contain a circular inclusion with a diameter of 0.375× the unit-cell size embedded in matrix. Multi-pebble model contain multiple circular inclusions

with diameters of 0.125×, 0.1875× and 0.25× the unit-cell size. We use 6 and 21 randomly placed inclusions, corresponding to 18% and 47% concentrations of inclusions, respectively.

Velocity boundary conditions with constant strain rate are applied in that velocities at the boundaries on average comply with pure shear deformation in multi-layer folding models and simple shear deformation in single- and multi-pebble models. Displacements ($\Delta\boldsymbol{x}$) are derived from a linear integration of velocities ($\boldsymbol{v}$) over a time increment (Δt): $\Delta\boldsymbol{x}=\boldsymbol{v}\cdot\Delta t$, to achieve strain increments for a vertical coaxial compression of $\Delta\gamma$=0.01 /step and simple shear of $\Delta\gamma$=0.02 /step. The velocity field is used to incrementally move *bnodes* that define the *flynn* boundaries. The model is repositioned to the initial square unit cell and material properties are mapped back on the regular, square grid, as is required by the VPFFT method, before each next deformation step (Fig. 1d).

Several parameters are systematically varied in the simulations (Table 1): (1) the viscosity ratio ($R\eta$) between hard and soft layers for multi-layer folding simulations, (2) the initial orientation (α) of layers for single- and multi-pebble models, (3) the layer viscosities of η_{hard} and η_{soft} for single- and multi-pebble models, and (4) the concentration (C) of pebbles for multi-pebble models.

The von Mises strain rate (or equivalent strain rate) normalized to the bulk von Mises strain rate for each *unode* is plotted to visualise the distribution of the strain rate intensity. The von Mises strain rate is the second invariant of the symmetric strain rate tensor.

Table 1. Settings for simulations

Experiments name	Hard layer viscosity η_{hard}	Soft layer viscosity η_{soft}	Viscosity ratio $R\eta = \eta_{hard}/\eta_{soft}$	Matrix viscosity η_{matrix}	Stress exponent n	Initial layer orientation α (°)
Multi-layer folding						
$R\eta 2$	2	1	2	1	3	
$R\eta 5$	5	1	5	1	3	
$R\eta 10$	10	1	1	1	3	
Single pebbble varing α						
$\alpha 0$	5	1		1	3	0
$\alpha 45$	5	1		1	3	45
$\alpha 90$	5	1		1	3	90
$\alpha 135$	5	1		1	3	135
$\alpha 170$	5	1		1	3	170
$\alpha 174$	5	1		1	3	174
$\alpha 175$*	5	1		1	3	175
$\alpha 176$	5	1		1	3	176
$\alpha 178$	5	1		1	3	178
Single pebbble varing η						
$\eta 1$	1.5	1.5		1	3	175
$\eta 2$	2	1.25		1	3	175
$\eta 3$	3	1		1	3	175
$\eta 4$	3	1.2		1	3	175
$\eta 5$	4	1		1	3	175
$\eta 6$	4	1.25		1	3	175
$\eta 7$*	5	1		1	3	175
$\eta 8$	5	1.25		1	3	175
$\eta 9$	6	1		1	3	175

*Simulation $\alpha 175$ is identical to simulation $\eta 7$.

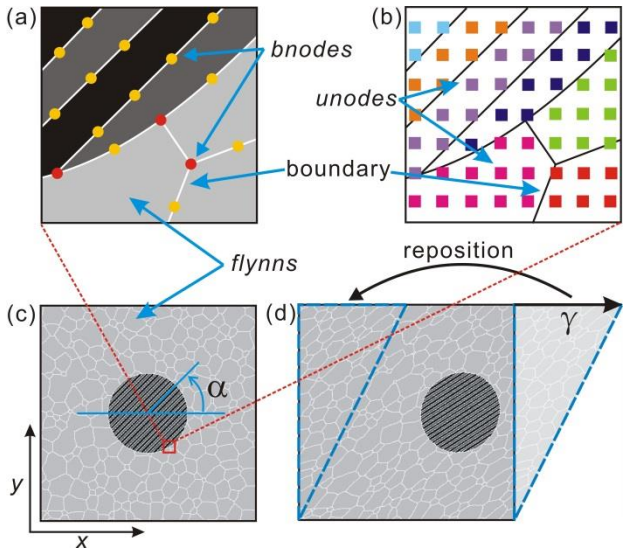

Fig. 1. Data structure. **(a)** Boundary nodes (*bnodes*) define *Flynns* that define the phase boundaries and

sub-regions. **(b)** Unconnected nodes (*unodes*) are superimposed on these *flynns* and store physical properties and state variables. **(c)** The square unit-cell contains circular pebbles, with layers with alternating viscosity (dark grey and black), embedded in a homogeneous matrix (light grey) composed of a set of *flynns* that are visualised by white solid lines. **(d)** The model is repositioned into the initial square unit cell after each step for dextral simple-shear deformation.

2.2 Model resolution

Each model can be mapped with $2^m \times 2^m$ *undoes*, with *m* a positive integer, which results in different resolutions of the models. To test the effect of different resolutions, we performed one multi-phase model with resolutions of 128×128, 256×256 and 512×512 *unodes* (Fig. 2). The models with 256×256 and 512×512 *undoes* show similar patterns of folds within inclusions, whereas the 128×128 model is distinctly different (Fig. 2a-c). The strain rate and stress localisation can be clearly identified in the inclusion layers with alternating viscosity in the 256×256 and 512×512 models, but there is distinctly less strain rate localisation inside the inclusion in the 128×128 model (Fig. 2d-i). This test shows that a resolution of 128×128, where the individual layers are one *unode* wide, is not sufficient. As the results of the 256×256 and 512×512 tests are almost identical, we chose 256×256 for all further runs as a compromise between resolution and calculation time.

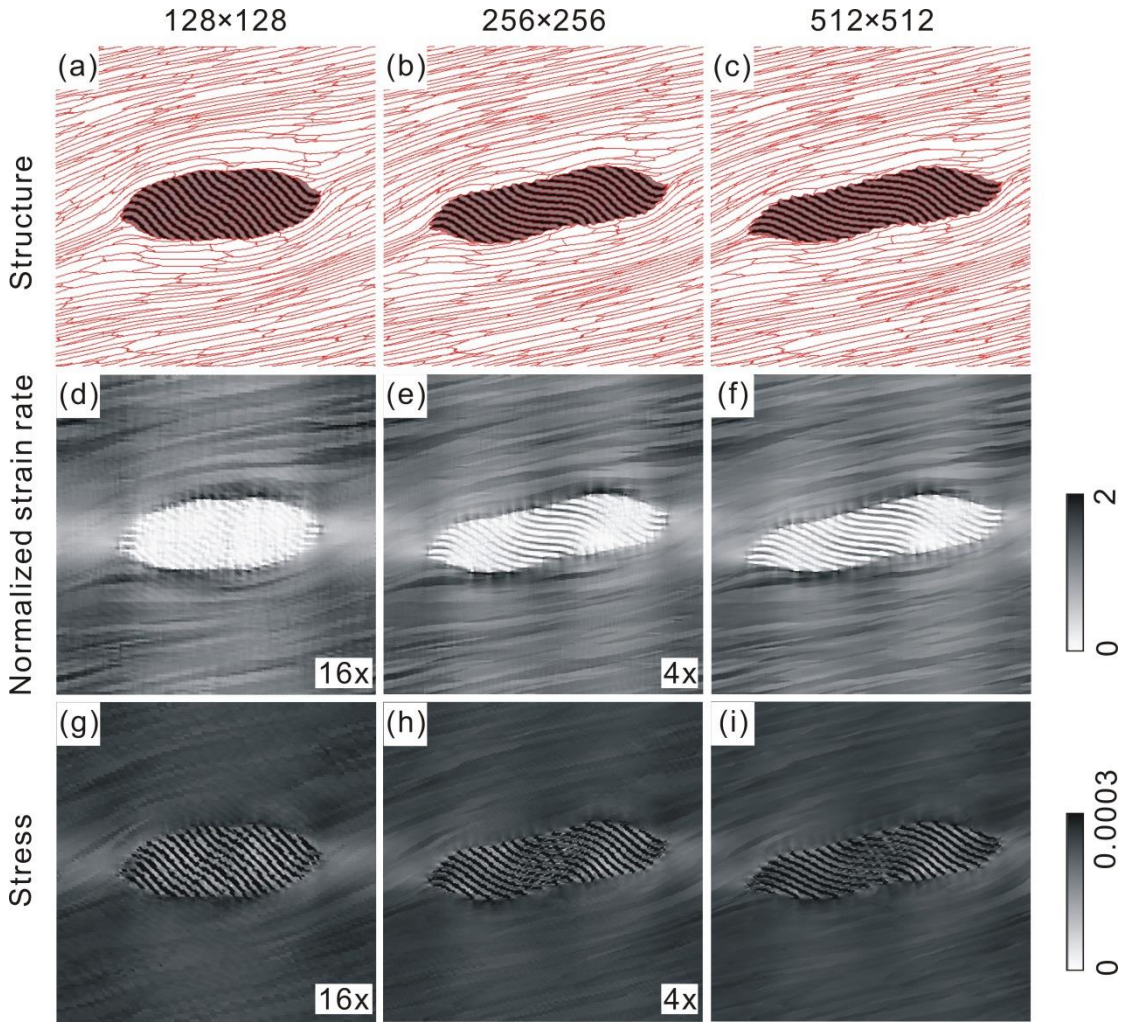

Fig.2. Structures **(a-c)**, normalized strain rate **(d-f)** and stress **(g-i)** in 128×128, 256×256 and 512×512 resolution models, at simple-shear deformation (top-to-right) to a finite strain of four. The models use same initial structure that consists of an inclusion with alternating viscosity layers embedded in an isotropic matrix.

3. Results

3.1 Folding of multiple layers

Layer thickening occurs more significantly in low viscosity ratio ($R\eta$=2) case than that in high viscosity ratio cases ($R\eta$=5 and 10), at 50% shortening in pure shear (Fig. 2b-d). The wavelength increases with increasing $R\eta$, as does the fold amplitude, as is expected from

Biot's (1961) theory. In the simulation with $R\eta$=2, the wavelength are much lower than that at high $R\eta$, but the amplitude is too low to identify the folds clearly. For folds to develop inside pebbles, the wavelength of these folds must be smaller than the pebble (blue ellipses in Fig. 3). However, to be able to see any folding, amplitudes must be significant as well. For the given layer widths relative to pebble size, folding inside pebbles is thus only expected at viscosity ratios from 5 to 10.

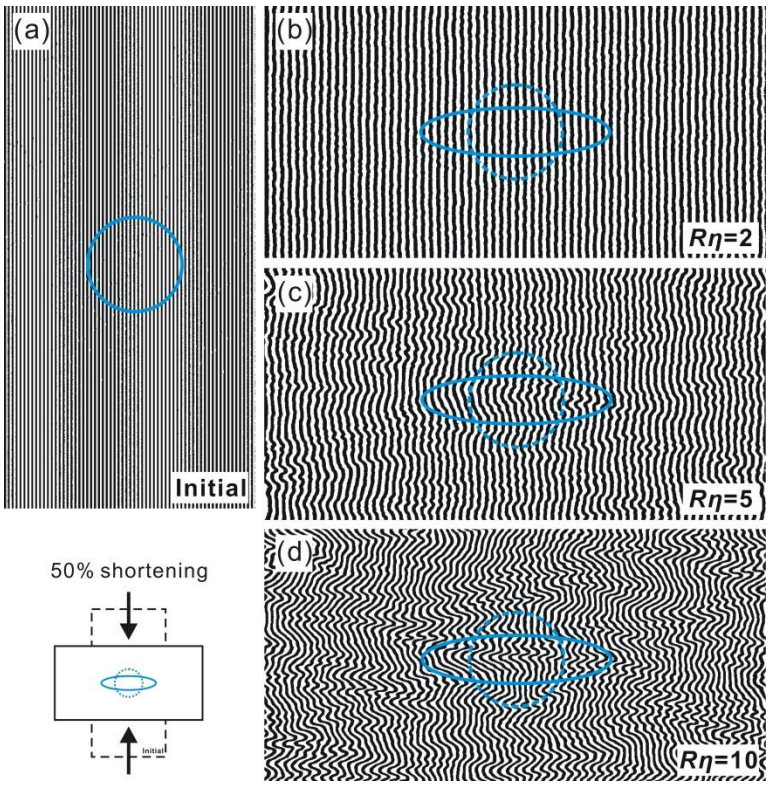

Fig. 3. Multi-layer initial structure **(a)** and folding after 50% vertical shortening, at viscosity ratio between competent (black) and soft (white) layers of $R\eta$=2 **(b)**, 5 **(c)** and 10 **(d)**. Dashed and solid blue outlines show initial pebble and deformed shape and size under passive deformation of 50% shortening.

3.2 Single-pebble simulations

At a viscosity ratio of η_{hard}=5 and η_{soft}=1, the behaviour of pebbles and their layers are significantly controlled by initial angles (α) between layers and the shear plan (Fig. 4). At low α

(0°, 45° and 90°), pebbles are extremely stretched and deform as if passive (Fig. 4a-c). The orientation of layers is close to that of pebble long axes. Layers are stretched along with the pebble, and are therefore not folded. At moderate α (135° and 170°), pebbles show pulsating deformation behaviour, with cyclical rotation and stretching (Ran et al. 2018a). Layers undergo limited stretching and bending. No folding can be observed in these cases. Foliations are wrapped around pebbles, which is visible by the deformed *flynns* in the matrix. At high α (174°, 175°, 176° and 178°), pebbles deform with deformable to passive behaviour. The orientation of layers is almost perpendicular to that of pebble long axes, and therefore undergoes significant shortening. Layer bending and folding can be observed from the center to margin. In our simulations, folding is only is observed when α=174°, 175°, 176° and 178°.

For a given initial angle of α=175°, pebbles can deform as passive, deformable and rigid, depending on the relative viscosities of the layers and matrix (Fig. 5; Ran et al., 2018a). Increasing the soft (η_{soft}) and/or hard (η_{hard}) layer viscosity can switch pebble behaviour from passive (Fig. 5a-c) to rigid (Fig. 5f,h). Folding within pebbles develops only in the simulations with viscosity settings of η_{hard}=3 and η_{soft}=1, η_{hard}=4 and η_{soft}=1, η_{hard}=5 and η_{soft}=1, η_{hard}=6 and η_{soft}=1.

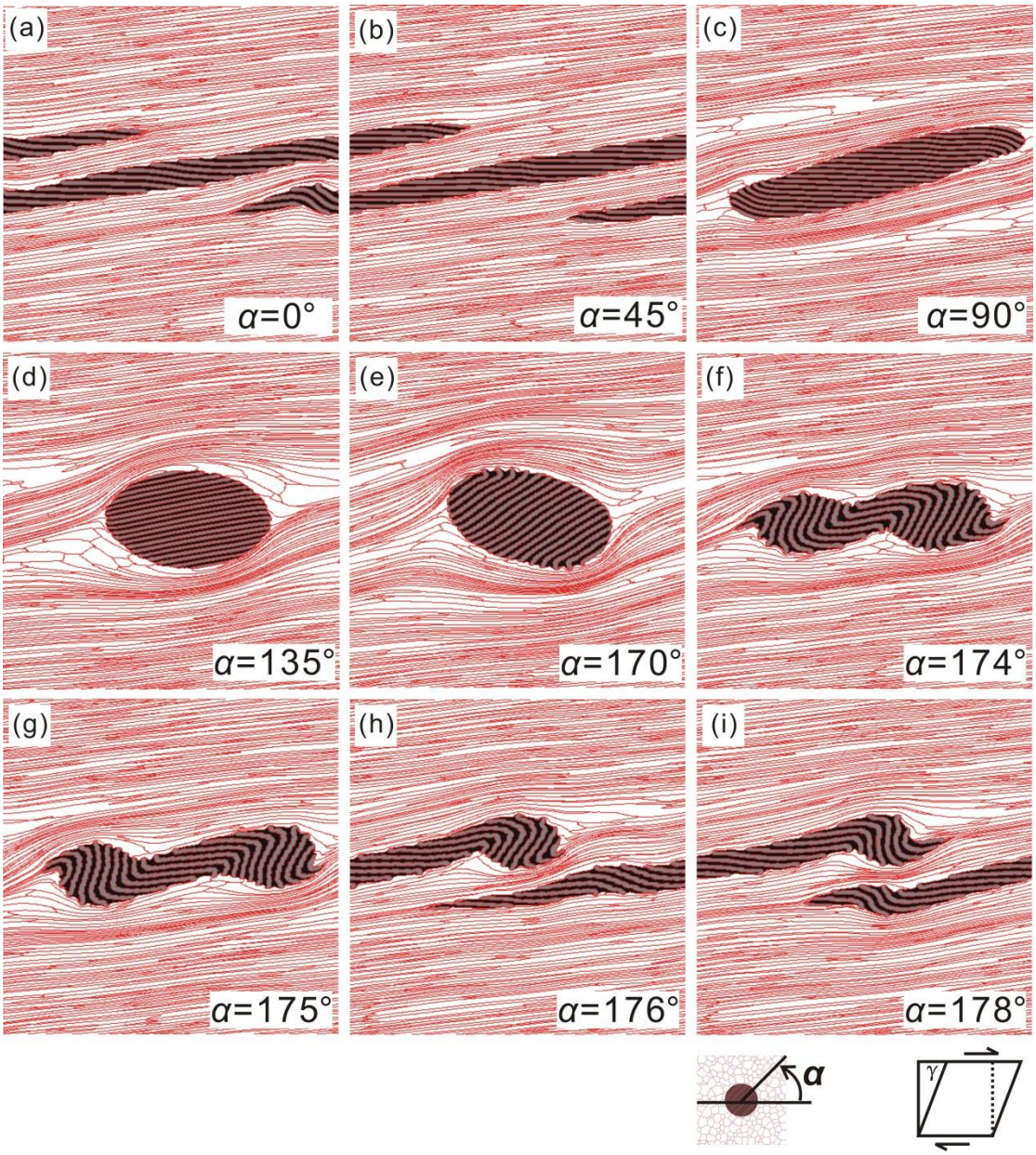

Fig. 4. Deforming layered pebble with initial angle (α) of 0 ° **(a)**, 45 ° **(b)**, 90 ° **(c)**, 135 ° **(d)**, 170 ° **(e)**, 174 ° **(f)**, 175 ° **(g)**, 176 ° **(h)** and 178 ° **(i)**, at a viscosity setting of η_{hard}=5 and η_{soft}=1, for simple-shear deformation (top to right) up to a shear strain of γ=8. Hard and soft layers are grey and black, and *flynn* boundaries red.

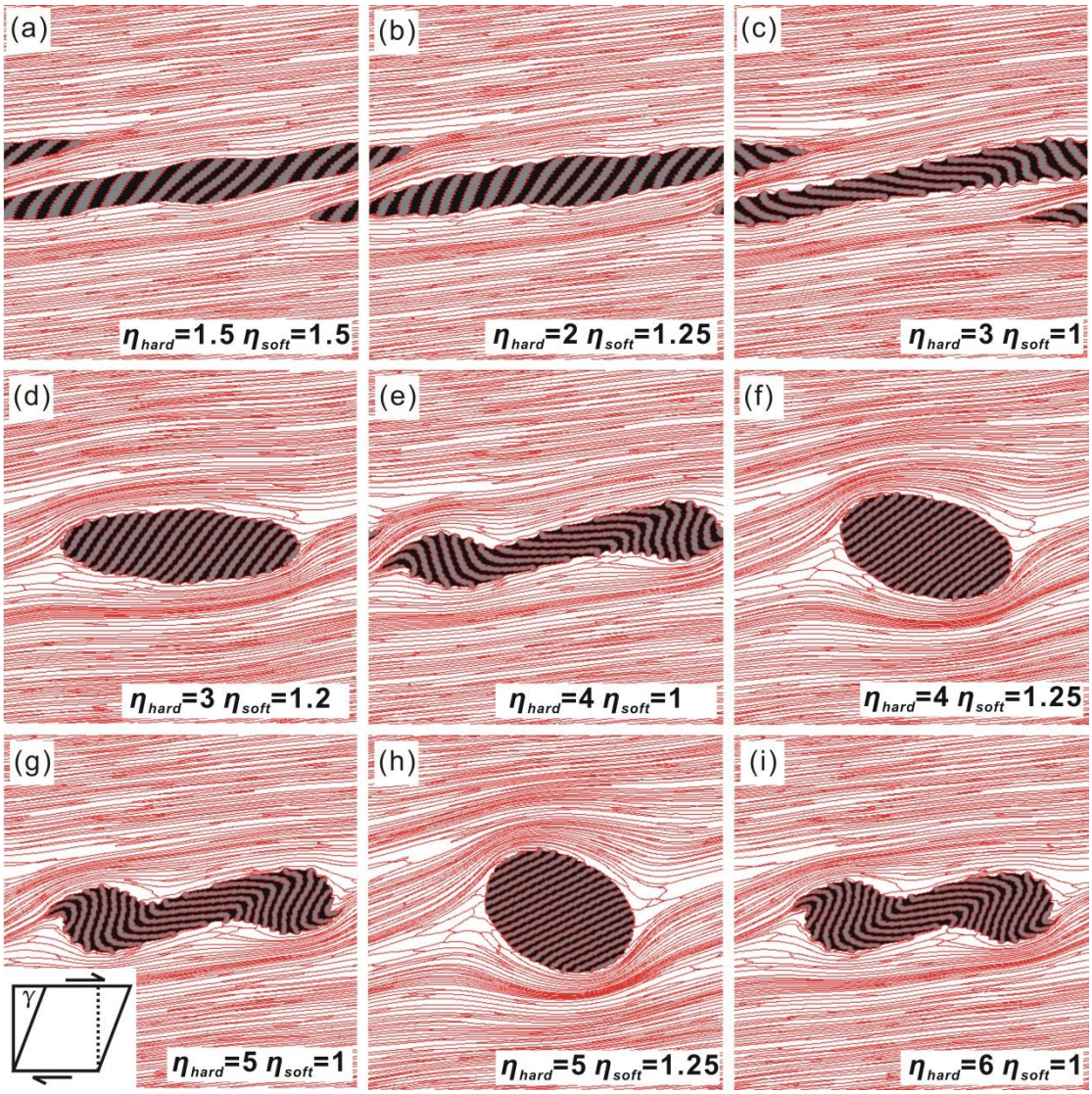

Fig. 5. Deforming layered pebble with initial layer orientation of α=175 °, at different layer viscosity settings of η_{hard}=1.5 and η_{soft}=1.5 **(a)**, η_{hard}=2 and η_{soft}=1.25 **(b)**, η_{hard}=3 and η_{soft}=1 **(c)**, η_{hard}=3 and η_{soft}=1.2 **(d)**, η_{hard}=4 and η_{soft}=1 **(e)**, η_{hard}=4 and η_{soft}=1.25 **(f)**, η_{hard}=5 and η_{soft}=1 **(g)**, η_{hard}=5 and η_{soft}=1.25 **(h)** and η_{hard}=6 and η_{soft}=1 **(i)**, for simple-shear deformation (top to right) up to a shear strain of γ=8. Hard and soft layers are grey and black, and *flynn* boundaries red.

3.3 Multiple pebbles

A decrease in layer viscosity enhances pebble deformation, and *vice versa*, for a given pebble concentration (Fig. 6). Pebbles in single simulation show very different deformation behaviour.

They deform as both deformable and passive at same viscosity setting and shear sense, depending on the initial orientation of layers inside a pebble and relative positions of pebbles (Fig. 6). Folding is observed in low-concentration (C=18%) simulations under top-to-right shearing, but in all simulations with a high concentration of pebbles (C=47%).

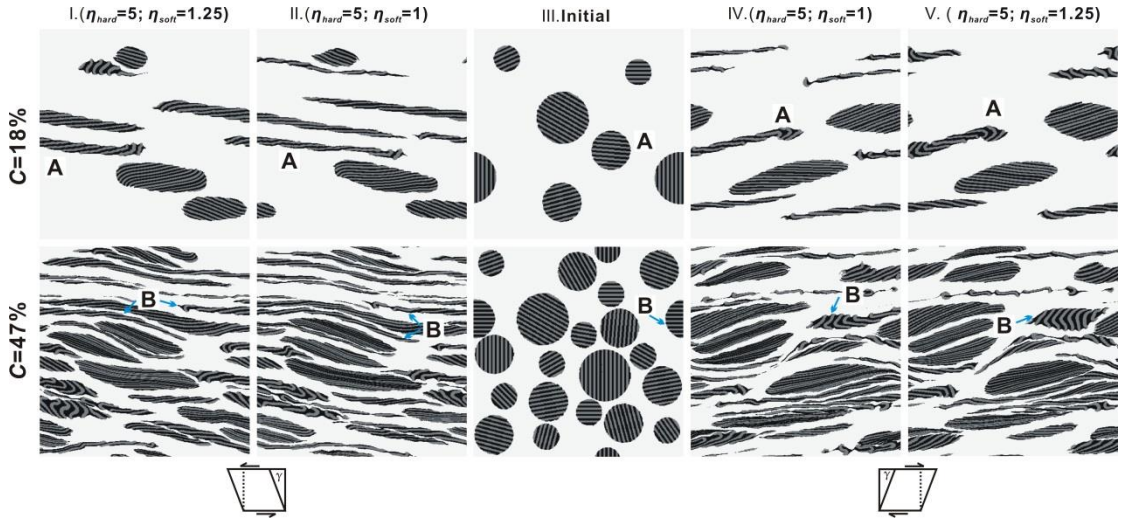

Fig. 6. Deformation of conglomerates with pebble concentration of C=18% (first row) and 47% (second row), at different viscosity settings of η_{hard}=5 and η_{soft}=1 (**Colum II** and **IV**) or η_{hard}=5 and η_{soft}=1.25 (**Colum I** and **V**), under top-to-left (Colum I and II) and top-to-right (Colum IV and V) simple-shear. Initial structures are shown in **Colum III**.

4. Discussion

4.1 Single pebble: initial orientation and viscosity of layers

Pebbles can deform as effectively passive, deformable and rigid depending on viscosity contrast between pebble and matrix, pebble concentrations and other factors (Ran et al., 2018a). From low to moderate initial angles ($0°\leq\alpha\leq\sim90°$), pebbles are significantly stretched and show passive deformation behaviour (Fig. 7). Layers within pebbles are stretched with pebble deformation. Only layer thinning and bending along with the pebble is observed. At high initial angles ($\sim135°\leq\alpha\leq\sim170°$), pebbles are deformable, and layers are shortening or thinning (Fig. 7).

Deformation of the pebbles is very limited, and thus there is not enough shortening to develop folding within pebbles. In the case with α=170 °, layer bending is recognized, but does not develop into folds. Folding within pebbles only develops at very high initial angles (~174°≤α≤~178 °) (Fig. 7). Pebbles are deformable and passive. Folding develops with suitable wavelengths and amplitudes that make folds recognizable. When α increases to ~180 ° (identical to 0 ° that shows horizontal orientation), the situation goes back to that of low α. At 0°≤α≤~135 °, layers within pebbles are stretching (Fig. 7). Otherwise, they are shortening at ~135 °＜α＜180 °. Our results suggest that folds within pebbles only develop in a quite narrow window of initial layer orientations (~174°≤α≤~178 °), for a given viscosity setting. In natural conglomerates, the distribution and orientation of pebbles can be expected to be random, and thus the initial angle α to range from 0 ° to 180 ° randomly. It allows us to infer that only few per cent of all pebbles is expected to develop folds.

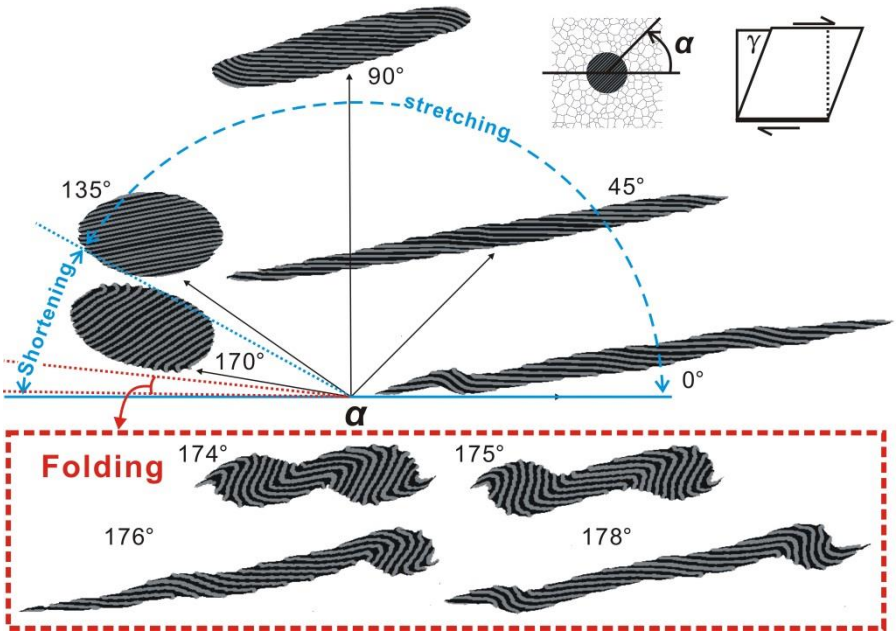

Fig. 7. Distribution of pebble deformation with different initial angles (α) between pebble layers and shear plane, at a viscosity setting of η_{hard}=5 and η_{soft}=1. Initial angle α of ~135 ° divide two types of behaviour: stretching and shortening. Folds within pebbles only develop at ~174°≤α≤~178 °.

Our simulations with different viscosity settings of pebble layers also show a quite narrow

window of conditions that lead to folding (Fig. 8). An increase in viscosity ratio between hard and soft layers within pebbles inhibits deformation of pebbles at a certain initial orientation of layers. It is identical to an increase in bulk viscosity of pebbles, i.e. increasing both layer viscosities, in our simulations, as well as in previous studies (Treagus and Treagus, 2001; Mandal et al., 2003; Vitale and Mazzoli, 2005; Takeda and Griera, 2006; Ran et al., 2018a). Increasing the viscosity of hard or/and soft layers reduces pebble flattening, and thus decreases layer shortening and bending. An excessive decrease in viscosity, however, leads to passive deformation: both pebble and layer get stretching and no folds develop. The simulations suggest two end member regimes of too "hard" to deform and too "soft" for folding. There is only a narrow widow of initial layer orientations and viscosity conditions at which folds within pebbles can form. In natural conglomerates, it is not easy to achieve the conditions of orientation and viscosity of layers, and thus it is not common that folding within pebbles develop with conglomerate deformation.

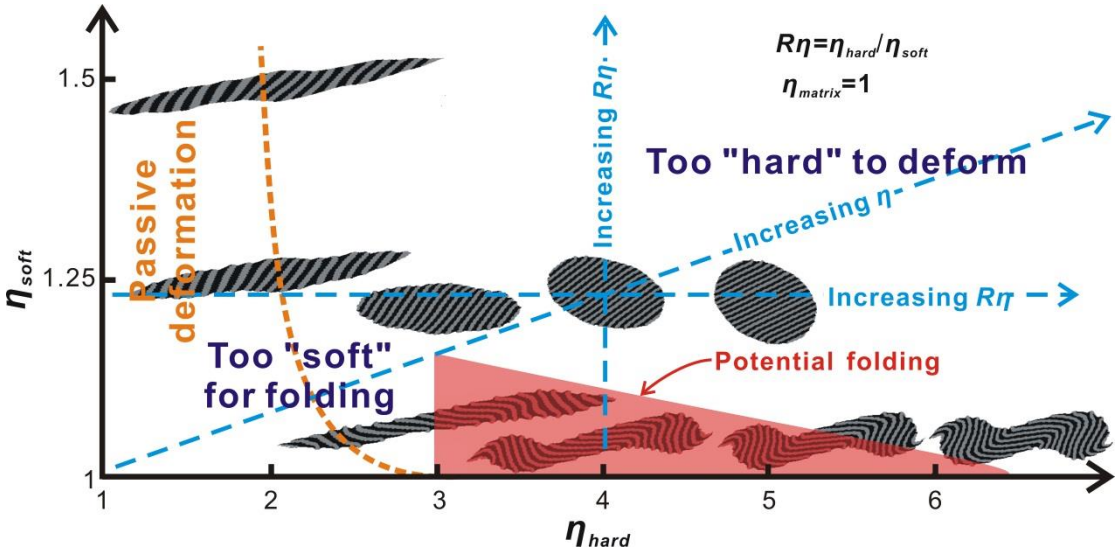

Fig. 8. Distribution of pebble deformation with an initial layer orientation of α=175 °, at different layer viscosity settings from Fig. 5. An increase of layer viscosity reduces pebble deformation and inhibits folding development (i.e. too "hard" to deform). A decrease of layer viscosity enhances pebble deformation (i.e. too "soft" for folding), and results in passive deformation. Folding in pebbles only occurs in a narrow range of conditions.

4.2 Interaction effects

In simulations with a low pebble concentration (C=18%), pebble A with α=176° behaves more passively than that in the single pebble simulation with same α, at layer viscosity of η_{hard}=5 and η_{soft}=1, under dextral shear. Pebble A at viscosity of η_{hard}=5 and η_{soft}=1.25 is similar to the single pebble simulation. In high concentration cases, pebble B with α=0° and a given viscosity set deforms differently in sinistral and dextral shear simulations. In dextral simulations, folding is observed in pebble B. In contrast, pebble B stretches extremely in sinistral shear. It is also different from the observation of the single pebble simulation. Previous studies have addressed the effect of interactions and reveal that an increase in pebble concentration enhances pebble deformation (Mandal et al., 2003; Vitale and Mazzoli, 2005; Jessell et al., 2009; Ran et al., 2018a). Our results suggest that the interactions between neighboring pebbles can not only affect the bulk deformation of pebbles but also the internal structures within pebbles.

4.3 Natural example

Our simulation results are compared with deformed conglomerates in the Yangjiaogou area, which lie at base of the Proterozoic Hutuo Group, North China Craton, already discussed above (Du et al., 2012 and Zhang et al., 2012). Ran et al. (2018a) suggest the deformed conglomerates with pebble concentration of 7% had a viscosity ratio of 5 to 8 for a linear rheology (n=1) and 2 to 5 for a power-law rheology (n=3) and underwent an approximately simple shear strain of about six. The low pebble concentration in this conglomerate allows it to be compared with our simulations of single pebbles in a power-law rheology (n=3) matrix.

The North China Craton is divided into three parts: the Eastern and Western blocks, and the Trans-North China Orogen (TNCO) where two blocks collided at ~2.5 or ~1.85 Ga (e.g., Zhao et al., 2001; Li and Kusky, 2007; Li et al., 2010). The Hutuo group is located in the Wutai Mountains area, the TNCO. There are three subgroups in the Hutuo Group from base to top: the Doucun, Dongye and Guojiazhai subgroups (e.g., Bai, 1986). The Hutuo Group consists of subgreenschist-facies to greenschist-facies sedimentary rocks and minor volcanic rocks that were

deposited after ~ 2.2 or ~1.9 Ga (e.g., Wilde et al., 2004; Li and Kusky, 2007; Liu et al., 2011). Previous studies interpret the deformed conglomerates as basal conglomerates at the base of the Doucun Subgroups, and suggest a uncomfortable contact between the Hutuo Group and the lower Neoarchean granitoids and the Wutai Group composed of metamagmatites and metasedimentary rocks from subgreenschist-facies to amphibolite-facies, intercalated with banded-iron formation (BIF) units (e.g., Bai, 1986; Wilde et al., 2004; Du et al., 2012). Pebbles in the Hutuo Group conglomerates consist mostly of the Wutai Group lithologies. BIF pebbles are dominating in the Yangjiaogou area, the Wutai Mountains. In the Yangjiaogou area, BIF pebbles are significantly deformed, and the foliation in the matrix wraps around stretched and rotated pebbles. Layer folding can be identified within BIF pebbles that occur only in a few amounts. The folding within pebbles and foliation patterns are identical to our simulations.

As we discussed in Introduction, it is not understood well when pebble-layer folding develops in the Hutuo Group conglomerates: before or after conglomerate deposition (Zhang et al., 2012; Du et al., 2012). If BIFs from the Wutai Group underwent a significant deformation leading to folding before conglomerate deposition, folds within pebbles should be common. It is different from our field observations in the Yangjiaogou area, where such folds do occur, but only in a small fraction of all pebbles. Our simulations indicate that the development of folding within pebbles requires a narrow range of initial orientations of pebble layers and viscosity contrasts between pebble layers and matrix. Folds within pebbles are therefore scarce, which is conformed to our field observations in the Yangjiaogou area. We suggest that the layer folding within pebbles formed after the conglomerate sedimentation. This indicates that there was no major tectonic event between formation of the Wutai and Hutuo Groups. The underlying Wutai Group would not have undergone a full cycle of burial, deformation and erosion before deposition of the Hutuo Group. Therefore, our simulations, together with field observations in the Yangjiaogou area, suggest that it is necessary to reconsider the relationship between the Hutuo and Wutai Groups and the tectonic processes in the TNCO.

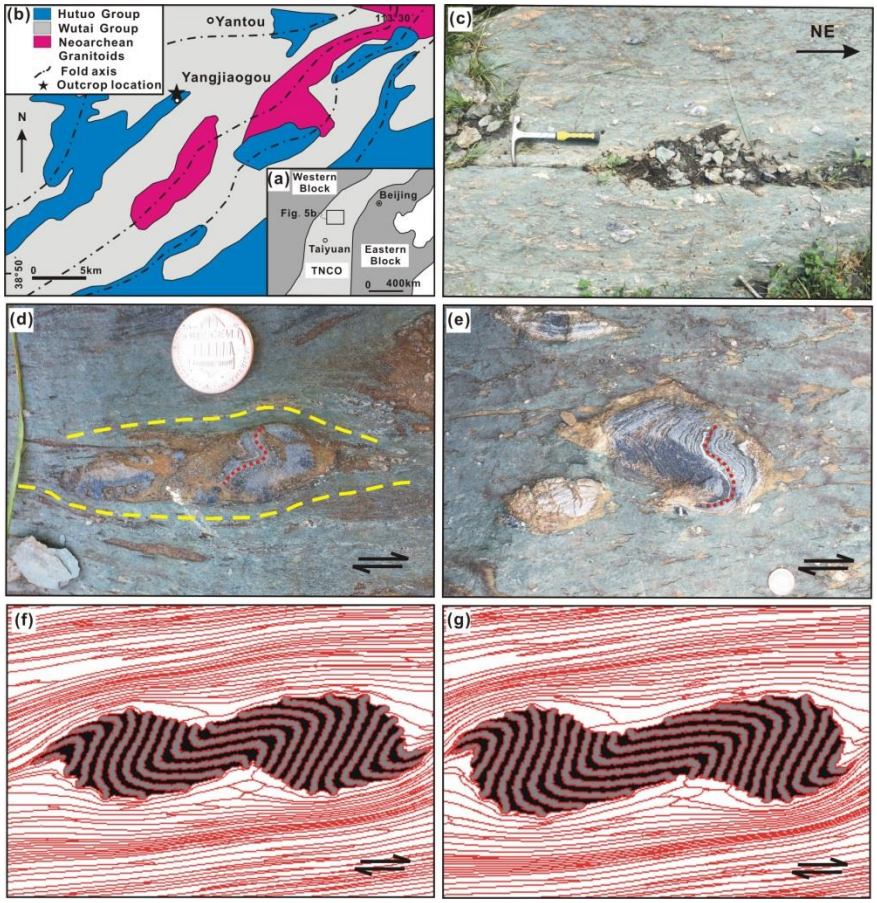

Fig. 9. Deformed conglomerates with BIF pebbles in the Wutai Mountains, North China Craton and selected comparable simulations. **(a)** Tectonic subdivision of the North China Craton (modified after Zhao et al., 2005). TNCO-Trans-North China Orogen. **(b)** Simplified geological map of the Yangjiaogou area and location of the outcrop of deformed conglomerates with BIF pebbles (from Ran et al., 2018b). **(c-e)** Deformed conglomerates with BIFs pebbles in the Yangjiaogou area. Folding within BIFs pebbles can identified in (d) and (e). The diameter of the 1 dollar-cent coin is 19mm. **(f-g)** Simulation results with single pebble of α174 (f) and η9 (g) at simple-shear strain of eight, compared with deformed conglomerates in the Yangjiaogou area.

5. Conclusions

We use the VPFFT+ELLE method to numerically model the development of folding within layered pebbles during ductile simple-shear deformation, varying the initial orientation and

viscosity settings of layers, in power-law rheology, up to finite strain of eight. Additionally, multi-layer folding is simulated to investigate the effect of viscosity contrast between hard and soft layers, under ductile pure shear of 50% shortening. Our numerical modelling results lead to the following conclusions:

1. Layers within pebbles can stretch, shorten and/or bend, depending on the initial orientation of layers relative to the shear plane, for a given viscosity setting, under ductile simple shear. Only a quite narrow range of initial orientations (with our settings from ~174° to ~178°) can result the development of folds within pebbles.

2. Deformation of layers within pebbles and pebbles is significantly affected by the viscosity of hard and soft layers, for a given initial orientation of layers. A high viscosity ratio between layers and matrix leads to rigid deformation of pebbles. At the other end of the spectrum, a low viscosity ratio results in passive deformation. Only a narrow range of viscosity ratios between them can lead to folding within pebbles.

3. Deformation of conglomerates with multi-pebble show that the concentration of pebble enhances pebble deformation, and the interactions between neighboring pebbles affect layer deformation.

4. Folding development within pebbles requires quite limited conditions of the initial orientation of layers and viscosity ratios between layers and matrix. The difficulty in developing folds within pebbles suggests that BIF pebbles with rare folds in deformed conglomerates of the Hutuo Group in the Wutai Mountains, China, developed during conglomerate deformation. This may remove a major tectonic event between formation of the Hutuo Group and the underlying Wutai Group.

Acknowledgments

Fieldwork in the Wutai Mountains area, China was supported by the China Geological Survey

grant (12120114076401). We appreciate the help for the fieldwork from Zhongbao Zhao, Changshun Wen, Chao Li and Gongyao Xu and the constructive suggestions from Guoli Yuan, Zhongbao Zhao and Changshun Wen. HR thanks the financially support by the China Scholarship Council (CSC; No. 201506400014).

References

Bai, J., 1986. The early Precambrian geology of Wutaishan. Tianjin Science and Technology Press, Tianjin.

Biot, M.A., 1961. Theory of folding of stratified viscoelastic media and its implication in tectonics and orogenesis. Geological Society of America Bulletin 72, 1595-1632.

Bons, P.D., Koehn, D., Jessell, M.W.(Eds), 2008. Microdynamics Simulation. In: Lecture Notes in Earth Sciences 106. Springer, Berlin.

Czeck, D.M., Fissler, D.A., Horsman, E., Tikoff, B., 2009. Strain analysis and theology contrasts in polymictic conglomerates: An example from the Seine metaconglomerates, Superior Province, Canada. Journal of Structural Geology 31, 1365-1376.

Dabrowski, M., Schmid, D.W., Podladchikov, Y.Y., 2012. A two-phase composite in simple shear: Effective mechanical anisotropy development and localization potential. Journal of Geophysical Research 117, B08406, doi:10.1029/2012JB009183.

Druguet, E., Hutton, D.H.W., 1998. Syntectonic anatexis and magmatism in a mid-crustal transpressional shear zone: an example from the Hercynian rocks of the eastern Pyrenees. Journal of Structural Geology, 20(7), 905-916.

Du, L., Yang, C., Wang, W., Ren, L., Wan, Y., Song, H., Gao, L., Geng, Y., Hou, K., 2012. Provenance of the Paleoproterozoic Hutuo Group basal conglomerates and Neoarchean crustal growth in the Wutai Mountains, North China Craton: Evidence from granite and quartzite pebble zircon U-Pb ages and Hf isotopes. Science China Earth Sciences, 55(11), 1796-1814.

Flinn, D., 1956. On the deformation of the Funzie conglomerate, Fetlar, Shetland. The Journal of Geology 64, 480-505.

Fossen, H., 2016. Structural geology. Cambridge University Press.

Gardner, R., Piazolo, S., Evans, L., Daczko, N., 2017. Patterns of strain localization in heterogeneous, polycrystalline rocks–a numerical perspective. Earth and Planetary Science Letters 463, 253-265.

Gomez-Rivas, E., Griera, A., Llorens, M.-G., Bons, P. D., Lebensohn, R. A., Piazolo, S., 2017. Subgrain rotation recrystallization during shearing: Insights from full-field numerical

simulations of halite polycrystals. Journal of Geophysical Research: Solid Earth 122, doi:10.1002/2017JB014508.

Griera, A., Bons, P. D., Jessell, M. W., Lebensohn, R. A., Evans, L., Gomez-Rivas, E., 2011. Strain localization and porphyrocalst rotation. Geology 39, 275-278.

Griera, A., Llorens, M.-G., Gomez-Rivas, E., Bons, P. D., Jessell, M. W., Evans, L. A., Lebensohn, R., 2013. Numerical modelling of porphyroclast and porphyroblast rotation in anisotropic rocks. Tectonophysics 587, 4-29.

Hobbs, B., Regenauer-Lieb, K., Ord, A., 2008. Folding with thermal-mechanical feedback. Journal of Structural Geology 30, 1572-1592.

Jansen, D., Llorens Verde, M.-G., Westhoff, J., Steinbach, F., Kipfstuhl, S., Bons, P.D., Griera, A., Weikusat, I., 2016. Small-scale disturbances in the stratigraphy of the NEEM ice core: observations and numerical model simulations. The Cryosphere 10, 359-370.

Jeffery, J.B., 1922. The motion of ellipsoidal particles immersed in viscous fluid. Proceedings of Royal Society London A102, 161-179.

Jessell, M., Bons, P.D., Evans, L., Barr, T., Stüwe, K., 2001. Elle: the numerical simulation of metamorphic and deformation microstructures, Computers and Geosciences 27, 17-30.

Jessell, M.W., Bons, P.D., Griera, A., Evans, L.A., Wilson, C.J.L., 2009. A tale of two viscosities. Journal of Structural Geology 31, 719-736.

Jessell, M.W., Siebert, E., Bons, P.D., Evans, L., Piazolo, S., 2005. A new type of numerical experiment on the spatial and temporal patterns of localization of deformation in a material with a coupling of grain size and rheology. Earth and Planetary Science Letters 239, 309-326.

Jiang, D., 2007a. Numerical modeling of the motion of deformable ellipsoidal objects in slow viscous flows. Journal of Structural Geology 29, 435-452.

Jiang, D., 2007b. Numerical modeling of the motion of rigid ellipsoidal objects in slow viscous flows: A new approach. Journal of Structural Geology 29, 189-200.

Jiang, D., 2013. The motion of deformable ellipsoids in power-law viscous materials: Formulation and numerical implementation of a micromechanical approach applicable to flow partitioning and heterogeneous deformation in Earth's lithosphere. Journal of Structural Geology 50, 22-34.

Jiang, D., Bentley, C., 2012. A micromechanical approach for simulating multiscale fabrics in large-scale high-strain zones: Theory and application. Journal of Geophysical Research 117, B12201, doi:10.1029/2012JB009327.

Johnson, S.E., Lenferink, H.J., Marsh, J.H., Price, N.A., Koons, P.O., West Jr., D.P., 2009a. Kinematic vorticity analysis and evolving strength of mylonitic shear zones: New data and numerical results. Geology 37, 1075-1078.

Johnson, S.E., Lenferink, H.J., Price, N.A., Marsh, J.H., Koons, P.O., West Jr., D.P., Beane, R., 2009b. Clast-based kinematic vorticity gauges: the effects of slip at matrix/clast interfaces.

Journal of Structural Geology 31, 1322-1339.

Lebensohn, R.A., 2001. N-site modeling of a 3D viscoplastic polycrystal using Fast Fourier Transform. Acta Materialia 49, 2723-2737.

Lebensohn, R.A., Idiart, M., Castañeda, P.P., Vincent, P.-G., 2011. Dilatational viscoplasticity of polycrystalline solids with inter-granular cavities. Philos. Maga. 91, 3038-3067.

Lebensohn, R.A., Montagnat, M., Mansuy, P., Duval, P., Meysonnier, J., Philip, A., 2009. Modeling viscoplastic behavior and heterogeneous intracrystalline deformation of columnar ice polycrystals. Acta Materialia 57, 1405-1415.

Li, J.H., Kusky, T.M., 2007. A late Archean foreland fold and thrust belt in the North China Craton: Implications for early collisional tectonics. Gondwana Research 12, 47-66.

Li, S., Zhao, G., Wilde, S.A., Zhang, J., Sun, M., Zhang, G. and Dai, L., 2010. Deformation history of the Hengshan–Wutai–Fuping Complexes: implications for the evolution of the Trans-North China Orogen. Gondwana Research 18, 611-631.

Lisle, R.J., 1979. Strain analysis using deformed pebbles: the influence of initial pebble shape. Tectonophysics 60, 263-277.

Lisle, R.J., 1985. The use of the orientation tensor for the description and statistical testing of fabric. Journal of Structural Geology 7, 115-117.

Liu C.H., Zhao G.C., Sun M., Zhang J., He Y.H., Yin C.Q., Wu F.Y., Yang J.H., 2011. U–Pb and Hf isotopic study of detrital zircons from the Hutuo group in the Trans-North China Orogen and tectonic implications. Gondwana Research 20, 106–121.

Llorens, M.-G., Bons, P. D., Griera, A., Gomez-Rivas, E., 2013a. When do folds unfold during progressive shear?. Geology 41, 563-566.

Llorens, M.-G., Bons, P. D., Griera, A., Gomez-Rivas, E., Evans, L. A., 2013b. Single layer folding in simple shear. Journal of Structural Geology 50, 209-220.

Llorens, M.-G., Griera, A., Bons, P. D., Lebensohn, R., Evans, L., Jansen, D., Weikusat, I, 2016a. Full-field prediction of ice dynamic recrystallisation under simple shear conditions, Earth and Planetary Science Letters 450, 233-242.

Llorens, M.-G., Griera, A., Bons, P.D., Roessiger, J., Lebensohn, R., Evans, L., Weikusat, I., 2016b. Dynamic recrystallisation of ice aggregates during co-axial viscoplastic deformation: a numerical approach. Journal of Glaciology 62, 359-377.

Llorens, M.-G., Griera, A., Steinbach, F., Bons, P.D., Gomez-Rivas, E., Jansen, D., Roessiger, J., Lebensohn, R.A., Weikusat, I., 2017. Dynamic recrystallization during deformation of polycrystalline ice: insights from numerical simulations. Philosophical Transactions Series A: Mathematical, physical, and engineering sciences 375, 2086, doi:10.1098/rsta.2015.0346.

Mancktelow, N.S., 2002. Finite-element modelling of shear zone development in viscoelastic materials and its implications for localisation of partial melting. Journal of Structural Geology 24, 1045-1053.

Mancktelow, N.S., 2011. Deformation of an elliptical inclusion in two-dimensional incompressible power-law viscous flow. Journal of Structural Geology 33, 1378-1393.

Mandal, N., Samanta, S.K., Bhattacharyya, G., Chakraborty, C., 2003. Deformation of ductile inclusions in a multiple inclusion system in pure shear. Journal of Structural Geology 25, 1359-1370.

Mandal, N., Samanta, S.K., Bhattacharyya, G., Chakraborty, C., 2005. Rotation behaviour of rigid inclusions in multiple association: insights from experimental and theoretical models. Journal of Structural Geology 27, 679-692.

March, A., 1932. Mathematische Theorie der Regelung nach der Korngestah bei affiner Deformation. Zeitschrift für Kristallographie - Crystalline Materials 81, 285-297.

Marques, F.O., Bose, S., 2004. Influence of a permanent low-friction boundary on rotation and flow in rigid inclusion/viscous matrix systems from an an-alogue perspective. Tectonophysics 382, 229-245.

Piazolo, S., Jessell, M.W., Bons, P.D., Evans, L., Becker, J.K. 2010. Numerical simulations of microstructures using the Elle platform: A modern research and teaching tool. Journal of the Geological Society of India 75, 110-127.

Piazolo, S., Passchier, C.W., 2002. Experimental modeling of vicous inclusions in a circular high strain shear rig: Implications for the interpretation of shape fabrics and deformed enclaves. Journal of Geophysical Research 107, B10242, doi: 10.1029/2000JB000030.

Ramsay and Huber, 1983. The techniques of modern structural geology, Volume 1: Strain Analysis. Academic Press, London.

Ramsay, L.J., 1967. Folding and Fracturing of Rocks. McGraw-Hill, New York.

Ran, H., Bons, P.D., Wang, G., Steinbach, F., Finch, M. Griera, A., Gomez-Rivas, E., Llorens, M.-G., Ran, S., Liang, X., Zhou, J. 2018a. High-strain deformation of conglomerates: numerical modelling, strain analysis, and an example from the Wutai Mountains, North China Craton. Journal of Structural Geology, accepted.

Ran, H., de Riese, T., Llorens, M.-G., Finch, M., Evans, L.A., Gomez-Rivas, E., Griera, A., Jessell, M.W., Lebensohn, R.A., Piazolo, S., Bons, P.D., 2018b. Time for anisotropy: The significance of mechanical anisotropy for the development of deformation structures. Journal of Structural Geology, doi: 10.1016/j.jsg.2018.04.019

Räss, L., Duretz, T., Podladchikov Y. Y., Schmalholz S. M., 2016. M2Di: Concise and efficient MATLAB 2-D Stokes solvers using the Finite Difference Method. Geochemistry, Geophysics and Geosystems 18, 755-768.

Rosenberg, C.L., 2001. Deformation of partially molten granite: a review and comparison of experimental and natural case studies. International Journal of Earth Sciences 90, 60-76.

Schmalholz, S.M., Podladchikov, Y.Y., Schmid, D.W., 2001. A spectral/finite difference method for simulating large deformations of heterogeneous, viscoelastic materials. Geophysical

Journal International 145, 199–208.

Steinbach F., Bons, P.D., Griera A., Jansen, D., Llorens M.-G., Roessiger, J., Weikusat I., 2016. Strain localization and dynamics recrystallisation in the ice-air aggregate: A numerical study. The Cryosphere 10, 3071-3089.

Steinbach, F., Kuiper, E.-J.N., Eichler, J., Bons, P.D., Drury, M.R., Griera, A., Pennock, G.M., Weikusat, I., 2017. The relevance of grain dissection for grain size reduction in polar ice: insights from numerical models and ice core microstructure analysis. Frontiers in Earth Science 5, doi: 10.3389/feart.2017.00066.

Takeda, Y.T., Griera, A., 2006. Rheological and kinematical responses to flow of two-phase rocks. Tectonophysics 427, 95-113.

Treagus, S.H., 1973. Buckling stability of a viscous single-layer system, oblique to the principal compression. Tectonophysics, 19(3), 271-289.

Treagus, S.H., 2002. Modelling the bulk viscosity of two-phase mixtures in terms of clast shape. Journal of Structural Geology 24, 57-76.

Treagus, S.H., Treagus, J.E., 2001. Effects of object ellipticity on strain, and implications for clast-matrix rocks. Journal of Structural Geology 23, 601-608.

Treagus, S.H., Treagus, J.E., 2002. Studies of strain and rheology of conglomerates. Journal of Structural Geology 24, 1541-1567.

Twiss, R.J., Moores, E.M., 1992. Structural geology. Macmillan.

Viola, G., Mancktelow, N.S., 2005. From XY tracking to buckling: axial plane cleavage fanning and folding during progressive deformation. Journal of Structural Geology 27, 409-417.

Vitale, S., Mazzoli, S., 2005. Influence of object concentration on finite strain and effective viscosity contrast: insights from naturally deformed packstones. Journal of Structural Geology 27, 2135-2149.

Wilde S.A., Zhao G.C., Wang K.Y., Sun M., 2004. First precise SHRIMP U–Pb zircon ages for the Hutuo Group, Wutaishan: further evidence for the Palaeoproterozoic amalgamation of the North China Craton. Chinese Science Bulletin, 49, 83–90.

Xu, X.W., Ma, T.L., Sun, L.Q., Cai, X.P., 2003. Characteristics and dynamic origin of the large-scale Jiaoluotage ductile compressional zone in the eastern Tianshan Mountains, China. Journal of Structural Geology, 25(11), 1901-1915.

Zhang, J., Zhao, G., Li, S., Sun, M., Chan, L. S., Shen, W., Liu, S., 2012. Structural pattern of the Wutai Complex and its constraints on the tectonic framework of the Trans-North China Orogen. Precambrian Research 222, 212-229.

Zhao, G.C., Wilde, S.A., Cawood, P.A., Sun, M., 2001. Archean blocks and their boundaries in the North China Craton: lithological, geochemical, structural and P–T path constraints and tectonic evolution. Precambrian Research 107, 45-73.

Chapter 4

Time for anisotropy: The significance of mechanical anisotropy for the development of deformation structures

Hao Ran[1,2], Tamara de Riese[1], Maria-Gema Llorens[1,3], Melanie A. Finch[1], Lynn A. Evans[4], Enrique Gomez-Rivas[5,6], Albert Griera[3], Mark W. Jessell[7], Ricardo A. Lebensohn[8], Sandra Piazolo[9], Paul D. Bons[1,*]

[1]Department of Geosciences, Eberhard Karls University Tübingen, Germany

[2]School of Earth Sciences and Resources, China University of Geosciences, Beijing, China

[3]Departament de Geologia, Universitat Autònoma de Barcelona, Spain

[4]School of Earth, Atmosphere and Environmental Sciences, Monash University, Clayton, Victoria, Australia

[5]Department of Mineralogy, Petrology and Applied Geology, University of Barcelona, Barcelona, Spain

[6]School of Geosciences, King's College, University of Aberdeen, Aberdeen, UK

[7]Centre for Exploration Targeting, School of Earth Sciences, The University of Western Australia, Crawley, Western Australia, Australia

[8]Material Science and Technology Division, Los Alamos National Laboratory, USA

[9]School of Earth and Environment, University of Leeds, Leeds, UK

Available online in *Journal of Structural Geology*, 20 May 2018, doi: 10.1016/j.jsg.2018.04.019.

Abstract

The forty-year history of the Journal of Structural Geology has recorded an enormous increase in the description, interpretation and modelling of deformation structures. Amongst factors that control deformation and the resulting structures, mechanical anisotropy has proven difficult to tackle. Using a Fast Fourier Transform-based numerical solver for viscoplastic deformation of crystalline materials, we illustrate how mechanical anisotropy has a profound effect on developing structures, such as crenulation cleavages, porphyroclast geometry and the initiation of shear bands and shear zones.

Keywords: Mechanical anisotropy; porphyroclasts; strain localisation; folds; shear zones

1. Introduction

Structural geologists have used a range of structures to determine deformation histories of rocks (e.g. Treagus, 1982; Ramsay and Huber, 1987; Hudleston and Lan, 1993; Passchier and Trouw, 2005). Many of these structures, such as folds and structures around rigid objects (i.e. porphyroclasts and porphyroblasts) are controlled by contrasts in the mechanical properties of the different minerals involved. These structures are therefore typically treated as inclusion-matrix (IM) systems, with typically a stronger inclusion phase (porphyroclasts, boudins, folding layers) embedded in a softer matrix.

To improve and quantify the interpretation of structures observed in the field, geologists have developed increasingly complex models for IM systems. Initially these were based on pioneering analytical models, such as those by Jeffery (1922), Eshelby (1957) and Ramberg (1962) for rotation of elliptical inclusions and Biot (1961) for folding of a single layer in a softer matrix. Taylor (1938) recognised the importance of the anisotropy of crystal plasticity to the development of crystallographic preferred orientations, and Kamb (1972) first explained how this could modify dynamic recrystallization in ice. The 40-year history of the Journal of Structural Geology has seen the advent and blossoming of numerical modelling to simulate a range of IM structures, thus helping geologists to understand how they form. Since the earliest computer simulations, models have steadily increased in sophistication and resolution. Early computers were usually restricted to linear, Newtonian rheology (e.g. Dieterich, 1970). Non-linear rheology, assumed common in rocks (Kirby, 1983; Carter and Tsenn, 1987), has now become a standard ingredient in models (Huddleston and Lan, 1994; Bons et al., 1997; Jessell et al., 2009; Mancktelow, 1999; 2011; Schmalholz and Maeder, 2012; Llorens et al., 2013a; Gardner et al. 2017). Boundary conditions in early models were usually restricted to pure shear conditions. However, many natural high-strain structures of interest typically develop in mylonites that deform close to simple shear (e.g. Passchier and Trouw, 2005; Gomez-Rivas et al., 2007). Simple shear deformation was therefore already applied to these IM systems early on (Jezek, 1994; Bons et al. 1997), but, for example, systematic modelling of folding in simple shear started much later (Viola and Mancktelow, 2005; Llorens et al., 2013a,b). The steadily increasing calculation speed of computers has allowed modellers to reach ever-higher finite strains (e.g. Schmalholz et al., 2001; Jessell et al., 2009; Dabrowski and Schmid, 2011; Dabrowski et al., 2012; Grasemann and Dabrowski, 2015). Additional factors and processes, such as shear heating, strain softening, slipping phase boundaries, grain-size effects, etc. have also been incorporated in models (Schmalholz and Podladchikov,

1999; Marques et al., 2005a,b, 2014; Schmalholz, 2006; Hobbs et al., 2008; Mancktelow, 2013; Montagnat et al., 2014; Gardner et al., 2017, among others).

Despite the enormous progress in IM-system modelling, there seems to be one elephant left in the room that is still commonly overlooked or ignored in these numerical models: anisotropy. Many material properties are known to be highly anisotropic in rocks and minerals, including magnetism, thermal expansion, elasticity, surface energy and mineral slip system activity. Early numerical simulations studies recognised the importance of mechanical anisotropy to the production of crystallographic preferred orientations in rocks (Taylor, 1938; Kröner, 1961; Etchecopar, 1977; Lister et al., 1978), and these have also been shown to be significant in the formation of larger-scale geological structures. For example, a field geologist would probably interpret the structure in Fig. 1a as follows (Druguet et al., 1997): the rock is a foliated biotite schist with a first foliation S_1 formed by aligned biotite grains. The foliated schist and a younger quartz vein were then deformed in a second event (D_2), which led to buckle folds in the vein and the formation of an axial-planar crenulation cleavage (S_2) in the schist. The quartz vein folds are comparable with those in numerical simulations and these folds from Cap de Creus (Spain) have indeed been used to compare with and validate numerical models (Llorens et al., 2013a,b). However, folds in the matrix look completely different. Whereas the quartz vein forms approximately parallel buckle folds, the crenulations in the schist are closer to similar folds (Fig. 1a). Structural geologists are aware that this is because the schist already has a distinct S_1-foliation, and is, therefore, strongly anisotropic. Although the importance of anisotropy for folding is known for decades (e.g. Bayly, 1970; Cobbold et al., 1971; Fletcher, 1974; Watkinson, 1983; Weijermars, 1992; Zhang et al., 1993), most numerical simulations have been of buckle folds in isotropic matrices (see Hudleston and Treagus (2010) for a review), with relatively few exceptions, mostly dealing with chevron folds (Mühlhaus et al., 2002; Kocher et al., 2006, 2008; Jansen et al., 2016; Schmalholz and Mancktelow, 2016). This example illustrates clearly that mechanical anisotropy needs to be taken into account when realistically modelling geological structures. Below we give examples of incorporating the effect of mechanical anisotropy in simulations of folding, σ-/δ-clast formation and shear localisation.

In the following section, we present a numerical method that allows geologists to assess the influence of anisotropy in the development of geological structures. This is followed by a number of examples of models highlighting the fact that anisotropy of material properties may be one of the "missing" keys to understand geological structures, holding much promise for future investigations.

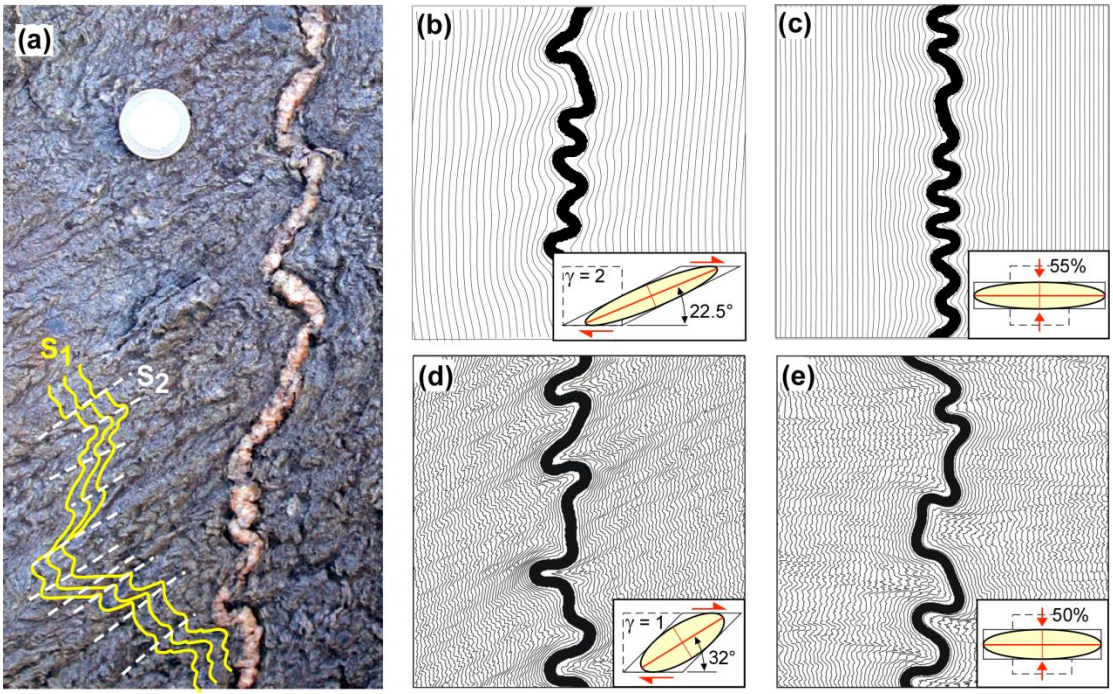

Fig. 1. (a) Folded quartz vein in biotite-schist matrix at Puig Culip (Cap de Creus, Eastern Pyrenees, Spain). The matrix has a first cleavage (S_1, solid yellow lines) that is crenulated to develop an S_2-cleavage (white dashed lines), axial planar to the vein folds. One Euro coin for scale, Ø=23 mm. **(b-c)** Finite-element simulations of folding of a single competent layer embedded in a weaker, isotropic matrix (same as presented in Llorens et al., 2013a,b). (b) dextral simple shear up to a shear strain of 2, and (c) vertical pure shear up to 55% shortening. **(d-e)** VPFFT-ELLE simulations of single layer folding in an anisotropic matrix (*A*=20) in (d) dextral simple shear up to a shear strain of 1, and (e) vertical pure shear up to 50% shortening. Note that the anisotropy in the matrix results in an axial planar crenulation cleavage, comparable to the one shown in (a). Grey area in insets is area of model shown.

2. The full-field crystal plasticity approach

At the grain scale, the crystal structure results in anisotropic behaviour of many physical properties. This is particularly relevant for viscous deformation accommodated by dislocation glide along particular slip systems (Frost and Ashby, 1983). Montagnat et al. (2014) provide an example of the many approaches that have been applied to model single- and polycrystal deformation of the mechanically highly anisotropic mineral ice Ih. Here, our simulations of polycrystalline aggregates with intrinsic anisotropy (i.e. anisotropy well developed at all scales) are based on the full-field VPFFT crystal plasticity code (Lebensohn, 2001), which

calculates the viscoplastic deformation for a polycrystalline aggregate using a Fast Fourier Transform-based numerical solver. The VPFFT code solves the micromechanical problem by finding the strain rate and stress fields that minimize the average local work-rate satisfying the constitutive relation at local level, under the constraints of strain compatibility and stress equilibrium (see Lebensohn (2001), Lebensohn et al. (2008; 2009) and Montagnat et al. (2014) for a more detailed description of the theoretical framework and the numerical algorithm, and Griera et al. (2013) and Llorens et al. (2016a,b) for the coupling with the ELLE microstructural simulation platform).

In geology the coupling of the full-field crystal plasticity VPFFT (Viscoplastic Full-Field Transform) method by Lebensohn (2001), Lebensohn et al. (2008) and the ELLE microstructural simulation platform (Jessell et al., 2001; Bons et al., 2008; Piazolo et al. 2010; http://www.elle.ws) has allowed the systematic simulation of deformation and recrystallization of polycrystalline rocks (such as ice and halite, e.g. Griera et al., 2011; 2013; Llorens et al., 2016a,b; 2017; Steinbach et al., 2016; 2017; Gomez-Rivas et al., 2017). In these cases, the polycrystalline aggregate is discretised into a periodic, regular mesh of nodes that store properties such as lattice orientation and dislocation density. These nodes act as Fourier Points in the VPFFT code and as unconnected nodes (*unodes)* in ELLE routines. Therefore, the integration between VPFFT and ELLE is based on the direct one-to-one mapping between the data structures of the two approaches. It is important to note that the VPFFT method is essentially scale independent and can therefore be used to simulate geological structures that have an inherent mechanical anisotropy ranging from small-scale (e.g. shear sense indicators, grain scale stress heterogeneities) to large-scale features (e.g. layers with contrasting rheology).

Here, we present a number of examples utilizing the VPFFT-ELLE method. In these examples the mechanical properties of the polycrystal are simulated assuming a "numerical mineral" with hexagonal symmetry, as was used by Griera et al. (2011; 2013) to model porphyroclast/-blast systems. With this symmetry, deformation is allowed to be accommodated by glide on the basal plane (basal slip) and along non-basal planes (pyramidal and prismatic slip). In this approach the grain anisotropy parameter (*A*) that accounts for the degree of anisotropy is defined as the ratio of the critical resolved stresses (τ_{cr}) of the non-basal basal and basal slip systems (e.g. Lebensohn et al., 2009). *A* is comparable to the ratio between normal and shear viscosity as employed by e.g. Mühlhaus et al. (2002) and Kocher et al. (2006, 2008). For all examples, a stress exponent of n=3 is assumed for all slip systems.

3. Examples

In the following, examples we contrast the effect of different material behaviour in terms of anisotropy on the characteristics of developing geological structures during deformation.

3.1. Single layer folding: The effect of matrix anisotropy

In our example, we first show deformation of a layer embedded in an isotropic matrix, using a non-linear viscous finite element method (BASIL, Houseman et al., 2008) within ELLE (Fig. 1b-c). BASIL is a finite element deformation module that simulates viscous deformation of a 2D sheet in plane-strain. BASIL can be coupled within ELLE in order to calculate the viscous strain rates and the associated stress field for different boundary conditions (i.e. from pure to simple shear). The grid of regularly spaced unconnected nodes (*unodes*) is used to track the deformation history and deformation field through passive lines initially parallel to the folding layer. ELLE uses both horizontally and vertically wrapping boundaries, allowing the model to be periodic in all directions. This approach reduces detrimental boundary effects and simplifies visualisation of the model at very high strains. See Jessell et al. (2005), Bons et al. (2008), and Jessell et al. (2009) for details about BASIL and ELLE.

In our simulations, we assigned homogeneous rheological properties to the polygons (Fig. 1b-c) that define the layer and matrix. With no variation in properties within the material, perturbations in the layer surface are critical for the resulting folds (Mancktelow, 1999; Zhang et al., 2000). Small variations in layer thickness were therefore introduced to initiate folding, as in Llorens et al. (2013a,b).

Figures 1b and 1c show the results for folding a single layer in simple and in pure shear, respectively. In BASIL, the rheology is defined by a power-law of the type:

$$\dot{\varepsilon} = \sigma^n / B, \qquad (1)$$

with $\dot{\varepsilon}$ the strain rate and σ the differential stress. The competence contrast between layer and matrix is defined here by the ratio of B_{layer}/B_{matrix}, set to 50 here (Table 1). Passive grid lines, originally parallel to the competent layer, show the deformation within the matrix. Folding decreases in intensity away from the "zone of contact strain" (Ramberg, 1962) near the layer, and strain is approximately homogeneous at the lateral edges of the model.

In Fig. 1d-e, we present two numerical simulations of single competent layer folding in an

anisotropic matrix using the VPFFT-ELLE code with power-law rheology. Initially, the basal slip plane of grains (individual square elements in the 256×256 element model) in the matrix were aligned approximately parallel to the layer. Therefore, starting models can be regarded as representing a foliated or mica-rich rock with anisotropy. The noise to initiate folding now derives from the small random variations in lattice orientation in the layer and matrix. The competent layer was set to be isotropic, with a τ_{cr} five times higher than the non-basal slip systems of the matrix. Their τ_{cr} in turn was set at 20 times that of the basal slip system, giving an anisotropy factor *A* of 20 (Table 1). Under pure and simple shear, the geometry of the folded single layer in the anisotropic matrix is similar to that in isotropic matrix (Fig. 1b-c). However, the geometry of microfolds represented by passive gridlines in the anisotropic matrix is very different from those in isotropic cases. The grid lines are folded in similar-type folds or crenulations that do not decay away from the competent layer (similar to results obtained by Kocher et al., 2006). Fold hinges align to form an axial-planar crenulation cleavage. The resulting geometry is similar to that of the natural example (Fig. 1a), with the passive gridlines representing S_1 and the crenulation cleavage S_2.

Table 1. Summary of method, deformation and properties of the models described in the text. All models were run using the ELLE platform.

Figure	**Method**[a]	**Deformation**	**Properties**		
			Layer	Matrix	
Fig. 1b	FEM	simple shear	*B*=50	*B*=1	
Fig. 1c	FEM	pure shear	*B*=50	*B*=1	
Fig. 1d	VPFFT	simple shear	τ_{cr}(all)=100	τ_{cr}(basal)=1 τ_{cr}(other)=20	
Fig. 1e	VPFFT	pure shear	τ_{cr}(all)=100	τ_{cr}(basal)=1 τ_{cr}(other)=20	
			Core object	Mantle	Matrix
Fig. 2a	VPFFT	simple shear	τ_{cr}(all)=50	τ_{cr}(all)=0.8	τ_{cr}(all)=1
Fig. 2b	VPFFT	simple shear	τ_{cr}(all)=50	τ_{cr}(all)=4	τ_{cr}(basal)= 1 τ_{cr}(other)=10
			Strong phase	Intermediate	Weak phase
Fig. 3b	VPFFT	simple shear	τ_{cr}(all)=30	τ_{cr}(all)=15	τ_{cr}(basal)= 1 τ_{cr}(other)=10
			Whole model		
Fig. 4	VPFFT	simple shear	τ_{cr}(basal)= 1 τ_{cr}(other)=1, 5, 20		

[a] FEM=finite element method with BASIL (Houseman et al., 2008). VPFFT= Viscoplastic Full-Field Transform method (Lebensohn, 2001), using 256×256elements.

3.2. Mantled porphyroclasts: δ- or σ-clasts?

σ- and δ-clasts, or more general mantled porphyroclasts are extremely useful shear-sense indicators (Passchier and Simpson, 1986; Hanmer and Passchier, 1991; Grasemann and

Dabrowski, 2015). These typically consist of a core porphyroclast with wings or tails of recrystallised material. Most studies addressed the rotation rate of isolated competent inclusions during deformation as a function of factors such as the object shape, stress exponent, and slipping object-matrix boundaries (e.g. Ghosh and Ramberg, 1976; Bons et al., 1997; Mandal et al., 2000; ten Grotenhuis et al., 2002; Schmid and Podladchikov, 2005; Fay et al., 2008; Dabrowski and Schmid, 2011; Griera et al., 2011, 2013; Mancktelow, 2011, 2013; Jiang, 2016). Although the role of anisotropy was recognised early on (e.g. Passchier et al., 1992), only Dabrowski and Schmid (2011) and Griera et al. (2011; 2013) actually included anisotropic flow properties in their numerical models. Main outcomes of these studies are that the rotation rate and the strain field around an object are affected by anisotropy.

With a strong emphasis on the ongoing rotation versus non-rotation of porphyroblats debate (Bell et al., 1992; Passchier et al., 1992), little attention has been given to the question what causes mantles porphyroclasts to either form δ or σ geometries. The main model is that this depends on the weakness of the mantle (or slipping interface) and its thickness relative to the size of the central object, with thick mantles forming σ-clasts and thin ones δ-clasts (Passchier and Sokoutis, 1993; and review of Marques et al., 2014). Bons et al. (1997) already suggested that anisotropy of the matrix would inhibit rotation, leading to the formation of σ-clasts. Here we show an example of the effect of anisotropy on the developing shape of a mantled porphyroclast, again using the VPFFT-ELLE code.

In the isotropic case (all slip systems of one phase have the same τ_{cr}; Table 1), the core object's τ_{cr} was set at 50x that of the matrix, while that of the mantle was 0.8x that of the matrix. Deformation is homogeneous in case of an isotropic mantle and the central object rotates at a rate close to the analytical solution of Jeffery (1922) (Griera et al., 2011; 2013) (Fig. 2a). Wings develop by smearing out of the mantle and as the points where the wings attach to the object rotate along with the object, a δ-clast develops (Fig. 2a). When the mantle is distinctly softer (τ_{cr}=4) than the object (τ_{cr}=50), and the matrix is anisotropic (A=10, with τ_{cr}=1 for the basal slip system and τ_{cr}=10 for non-basal slip systems), deformation in the matrix is highly heterogeneous and folds and shear bands develop (Griera et al., 2011; 2013). Rotation of the object is now inhibited (contrary to the analytical model of Fletcher, 2009) and the attachment points of the wings do not rotate enough to develop the distinct embayments of δ-clasts (Fig. 2b). Instead, a σ-clast forms.

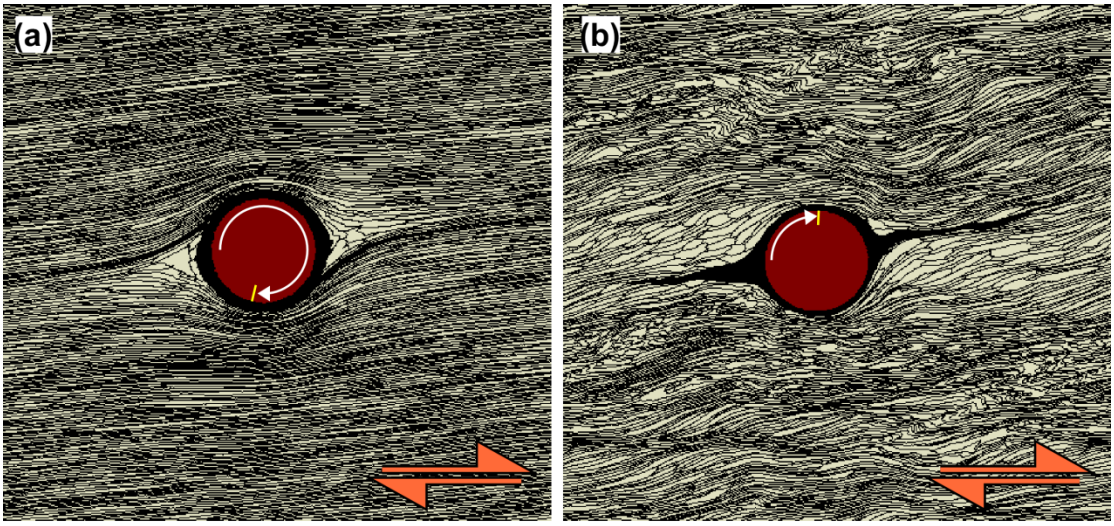

Fig. 2. VPFFT-ELLE-simulations of a circular hard object (dark red), deformed to a dextral simple shear strain of ten, with a softer mantle (black), embedded in an **(a)** isotropic or **(b)** anisotropic matrix (A=10). Strain distribution is illustrated by the boundaries of the originally equidimensional elements. White arrows show the total amount of rotation of the objects. Ongoing rotation of the object in the isotropic matrix leads to the development of a δ-clast, while an anisotropic matrix leads to strongly heterogeneous matrix deformation, reduced object rotation and, hence, development of a σ-clast.

These results confirm the observations of Griera et al (2013) that the incorporation of anisotropy provides an elegant way to explain controversies in structural geology regarding the duality between rotation or non-rotation of porphyroblasts (Bell et al., 1992; Passchier et al., 1992). Spiral geometries of inclusions preferentially develop in isotropic conditions, while an increase in anisotropy tends to reduce rotation of porphyroblasts of which the inclusion trails then indicate growth over a crenulated matrix.

3.3. Shear bands in composite materials

Structures in natural and modelled shear zones are determined in part by the strength contrast between minerals and slip systems within minerals. Weak minerals define the foliation (S-surface) at 45 ° from the shear zone boundary, and planes progressively rotate into parallelism with the shear zone boundary and the C-surface (Fig. 3a). Less well understood is the development of C' shear bands (Fig. 3a), despite their ubiquity in shear zones in nature, experiments, and models (White, 1979; Platt and Vissers, 1980; Platt, 1984; Dennis and Secor, 1987). C' shear bands dip at an angle of ~15–35 ° from the shear zone boundary, in the opposite direction to the main foliation (or S plane; White, 1979; Platt and Vissers, 1980) and show synthetic, normal shear sense (Fig. 3a). They are most common in well-foliated rocks

such as schists and phyllites (Passchier, 1991; Delle Piane et al., 2009) and so it has been suggested that anisotropy is required for their development (Wilson, 1984; Goodwin and Tikoff, 2002).

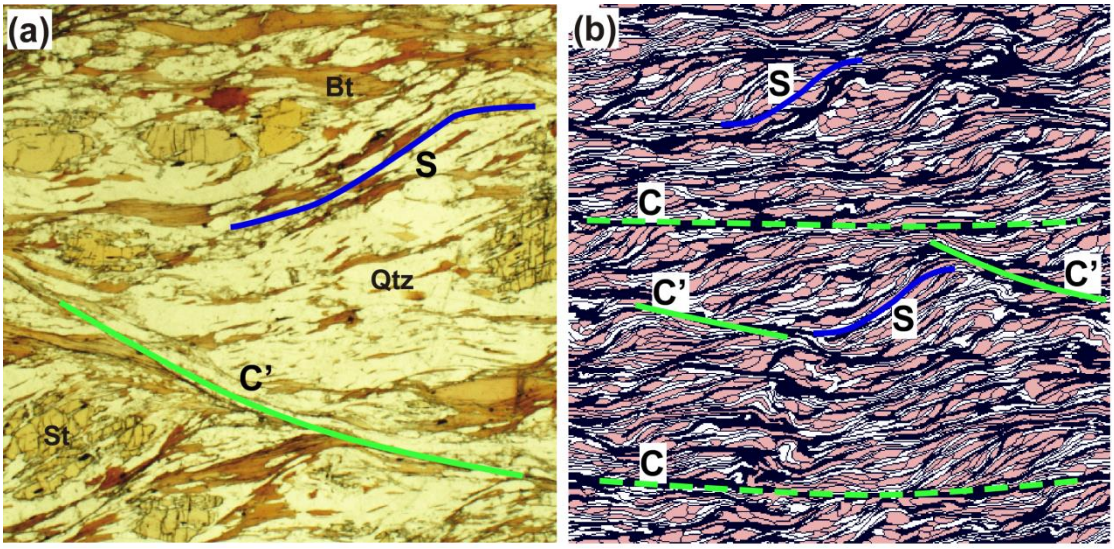

Fig. 3. C' shear bands in **(a)** a naturally deformed rock and **(b)** an VPFFT-ELLE simulation with a weak (black), intermediate (white) and strong (pink) phase. St = staurolite, Qtz = quartz, Bt = biotite. The S-foliation is highlighted with blue lines, C-planes with green lines and C'-planes with dashed green lines.

We used VPFFT-ELLE to model the development of C' shear bands in anisotropic materials, building on the work of Jessell et al. (2009) by testing the proportion of weak phase required for the development of C' shear bands in three-phase models and by introducing anisotropy to the crystallography of the weakest phase. The model shown (Fig. 3b) included a strong, intermediate, and a weak phase, the latter of which had a basal plane ten times weaker than prismatic and pyramidal planes (i.e. A=10). We found that C' shear bands formed in all models with >1% weak phase and were more abundant in models with a higher proportion of weak phase. In nature (Fig. 3a) and in models (Fig. 3b) C' shear bands are dominantly defined by the weakest phase.

3.4. Shear localisation

Shear localisation develops at almost all scales in ductile rocks. For example, the shear zones in Cap de Creus (NE Spain) are linked in an anastomosing framework with self-similar properties, where a pre-existing foliation in the metasediments have led to instabilities, forming shear zones at a wide range of scales (Druguet et al., 1997; Carreras, 2001; Fusseis et

al., 2006; Schrank et al., 2008). In polar ice sheet dynamics, the behaviour of large ice masses is strongly influenced by visco-plastic anisotropy of grains and their ability to form a lattice preferred orientation (LPO) by lattice rotation (Azuma and Higashi, 1985; Alley, 1988). The flow of glaciers and polar ice sheets is controlled by the highly anisotropic rheology of Ice Ih crystals (Azuma, 1994; Bons et al., 2016; Llorens et al., 2016a,b; Llorens et al., 2017), which may lead to high strain zones in the glaciers and polar ice sheets (Marmo and Wilson, 1998) and folding (Bons et al., 2016; Jansen et al., 2016).

To show how anisotropy (defined by the parameter *A*) affects localisation, we simulate the deformation of a pure, single-phase polycrystal in dextral simple shear (Fig. 4) up to a shear strain of 1.5 with VPFFT-ELLE described above. Basal planes were initially randomly oriented. Strain localisation occurs only in anisotropic cases ($A>1$), as can be seen by the passive deformation of the polygon boundaries that originally had a foam texture (Fig. 4a) and the map of the normalised Von Mises strain rate field (Fig. 4b). High strain-rate rate bands oriented at a low angle to the horizontal shear plane are clearly visible (Fig.4a and b), especially at high anisotropy values ($A>>1$).

The frequency distribution of normalised strain rates, at a shear strain of three, in the isotropic material ($A=1$) is approximately normal (Fig. 4c). Simulations with $A>1$ show frequency distribution that deviate from normal distribution (Fig. 4c) and are closer to log-normal. However, they are not exactly log-normal, as they become heavy tailed for large strain-rate values. Higher strain rate values become overrepresented with values up to 20 times the mean for $A=20$. Therefore, a material with a higher degree of anisotropy will reach significantly higher strain rate values due to strain localisation. As a result, most of the material deforms at a significantly lower rate than the mean strain rate, as can be seen by the leftward shift of the frequency peak in Fig. 4c.

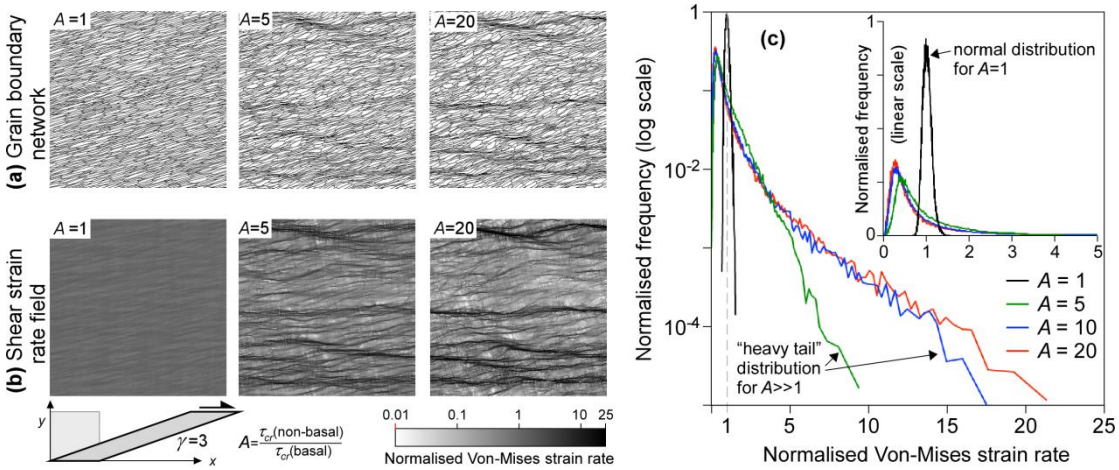

Fig. 4. VPFFT-ELLE simulations of polycrystals deformed in dextral simple shear up to a shear strain of 3 and with increasing degree of grain anisotropy (*A*) from 1 to 20. Anisotropy is defined as the ratio between the critical resolved shear stress (τ_{cr}) required to activate the non-basal and basal slip systems. **(a)** Grain boundary network and **(b)** Von-Mises shear strain rate field, normalized with respect to the bulk value. For better visibility figures of Von Mises strain rate field have been enlarged two times, only showing the lower right quarter of the model. **(c)** Frequency distribution of normalised Von-Mises strain rates for different anisotropy values. Whereas the distribution for *A*=1 is approximately normal with a mean of one, higher *A*-values lead to a frequency peak below the mean and a "heavy tail" of high strain rate values. Inset shows the same data, but with a linear vertical scale.

4. Discussion and conclusions

The examples described in previous sections provide a brief glimpse into the effect of intrinsic mechanical anisotropy (Griera et al. 2013) on deformation structures in rocks. In all cases, anisotropy caused heterogeneous strain: expressed in the axial planar crenulation cleavage in Fig. 1d-e; folds and shear bands in the matrix of the σ-clast in Fig. 2b; and shear bands in shearing multiphase (Fig. 3) and single-phase (Fig. 4) models. The strain localisation may be the most interesting aspect here. Processes such as shear heating and grain-size reduction have been considered in detail as causes for strain localisation (Tullis and Yund, 1985; Braun et al., 1999; de Bresser et al., 2001; Bercovici, 2003; Jessell et al., 2005; Kaus and Podladchikov, 2006; Platt and Behr, 2011; Montési 2013). Mechanical anisotropy may be of equal importance, leading to shear zones from the grain scale (Fig. 3) to possibly continental sutures, similar to the damage model of Bercovici (2014).

In this paper we have used to VPFFT+ELLE numerical code to illustrate the effect of intrinsic mechanical anisotropy. We do not claim that this is the only available approach. We use this anniversary issue to encourage structural geologists to develop more analytical and numerical models to finally elucidate the role of mechanical anisotropy on all scales.

Acknowledgments

HR acknowledges financial support by the China Scholarship Council (CSC; grant nr. 201506400014). EGR acknowledges the support of the Beatriu de Pinós programme of the Government of Catalonia's Secretariat for Universities and Research of the Department of Economy and Knowledge (2016 BP 00208). We thank Bruce Hobbs and an anonymous reviewer for their suggestions to improve this article.

References

Alley, R.B., 1988. Fabrics in polar ice sheets: development and prediction. Science 240, 493-495.

Azuma, N., 1994. A flow law for anisotropic ice and its application to ice sheets. Earth and Planetary Science Letters 128, 601-614.

Azuma, N. Higashi, A., 1985. Formation processes of ice fabric pattern in ice sheets. Annals of Glaciology 6, 130-134.

Bayly, M.B., 1970. Viscosity and anisotropy estimates from measurements on chevron folds. Tectonophysics 9, 459-474.

Bell, T.H., Johnson, S.E., Davis, B., Forde, A., Hayward, N., Wilkins, C., 1992. Porphyroblast inclusion-trail orientation data: eppure-non-son-girate. Journal of Metamorphic Geology 10, 295-307.

Bercovici, D., 2003. The generation of plate tectonics from mantle convection. Earth and Planetary Science Letters 205, 107-121.

Bercovici, D., 2014. Plate tectonics, damage and inheritance. Nature 508, 513–516.

Biot, M.A., 1961. Theory of folding of stratified viscoelastic media and its implication in tectonics and orogenesis. Geological Society of America Bulletin 72, 1595-1632.

Bons, P.D., Barr, T.D., ten Brink, C.E., 1997. The development of delta-clasts in non-linear viscous materials: a numerical approach. Tectonophysics 270, 29-41.

Bons, P.D., Koehn, D., Jessell, M.W. (Eds.), 2008. Microdynamics simulation. In: Lecture Notes in Earth Science 106. Springer, Berlin.

Bons, P.D., Jansen, D., Mundel, F., Bauer, C.C., Binder, T., Eisen, O., Jessell, M.W., Llorens, M.-G., Steinbach, F., Steinhage, D., Weikusat, I., 2016. Converging flow and anisotropy cause large-scale folding in Greenland ice sheet. Nature Communications 7, doi: 10.1038/ncomms11427.

Braun, J., Chery, J., Poliakov, A., Mainprice, D., Vauchez, A., Tommasi, A., Daignieres, M., 1999. A simple paramaterization of strain localization in the ductile regime due to grain size reduction: a case study for olivine. Journal of Geophysical Research 104, 25167-25181.

Carreras, J., 2001. Zooming on Northern Cap de Creus shear zones. Journal of Structural Geology 23, 1457-1486.

Carter, N.L., Tsenn, M.C., 1987. Flow properties of the continental lithosphere. Tectonophysics 136, 27-63.

Cobbold, P.R., Cosgrove, J.W., Summers, J.M., 1971. Development of internal structures in

deformed anisotropic rocks. Tectonophysics 12, 23-53.

Dabrowski, M., Schmid, D.W., 2011. A rigid circular inclusion in an anisotropic host subject to simple shear. Journal of Structural Geology 33, 1169-1177.

Dabrowski, M., Schmid, D.W., Podladchikov, Y.Y., 2012. A two-phase composite in simple shear: Effective mechanical anisotropy development and localization potential. Journal of Geophysical Research 117, B08406, doi: 10.1029/2012JB009183.

de Bresser, J.H.P., ter Heege, J.H., Spiers, C.J., 2001. Grain size reduction by dynamic recrystallization: can it result in major rheological weakening? International Journal of Earth Sciences 90, 28-45.

Delle Piane, C., Wilson, C.J.L., Burlini, L., 2009. Dilatant plasticity in high-strain experiments on calcite–muscovite aggregates. Journal of Structural Geology 31, 1084-1099.

Dennis, A.J., Secor, D.T., 1987. A model for the development of crenulations in shear zones with applications from the Southern Appalachian Piedmont. Journal of Structural Geology 9, 809-817.

Dieterich, J.H., 1970. Computer experiments on mechanics of finite-amplitude folds. Canadian Journal of Earth Sciences 7, 467-476.

Druguet, E., Passchier, C.W., Carreras, J., Victor, P., den Brok, S.W.J., 1997. Analysis of a complex high-strain zone at Cap de Creus, Spain. Tectonophysics 280, 31–45.

Eshelby, J.D., 1957. The determination of the elastic field of an ellipsoidal inclusion and related problems. Proceedings of the Royal Society of London Series A 241, 376-396.

Etchecopar, A., 1977. A plane kinematic model of progressive deformation in a polycrystalline aggregate. Tectonophysics 39, 121-139.

Fay, C., Bell, T.H., Hobbs, B.E., 2008, Porphyroblast rotation versus nonrotation: Conflict resolution! Geology 36, 307–310.

Fletcher, R.C., 1974. Wavelength selection in the folding of a single layer with power-law rheology. American Journal of Science 274, 1029-1043.

Fletcher, R.C., 2009. Deformable, rigid, and inviscid elliptical inclusions in a homogeneous incompressible anisotropic viscous fluid. Journal of Structural Geology 31, 382-387.

Frost, H.J., Ashby, M.F., 1983. Deformation-Mechanism Maps: the Plasticity and Creep of Metals and Ceramics. Pergamon, Oxford.

Fusseis, F., Handy, M. R., Schrank, C., 2006. Networking of shear zones at the brittle-to-viscous transition (Cap de Creus, NE Spain). Journal of Structural Geology 28, 1228-1243.

Gardner, R., Piazolo, S., Evans, L., Daczko, N., 2017. Patterns of strain localization in

heterogeneous, polycrystalline rocks – a numerical perspective. Earth and Planetary Science Letters 463, 253-265.

Ghosh, S.K., Ramberg, H., 1976. Reorientation of inclusions by combination of pure and simple shear. Tectonophysics 34, 1-70.

Gomez-Rivas, E., Bons, P.D., Griera, A., Carreras, J., Druguet, E. Evans, L., 2007. Strain and vorticity analysis using small-scale faults and associated drag folds. Journal of Structural Geology 29, 1882-1899.

Gomez-Rivas, E., Griera, A., Llorens, M.-G., Bons, P. D., Lebensohn, R. A., Piazolo, S., 2017. Subgrain rotation recrystallization during shearing: Insights from full-field numerical simulations of halite polycrystals. Journal of Geophysical Research: Solid Earth 122, doi: 10.1002/2017JB014508.

Goodwin, L.B., Tikoff, B., 2002. Competency contrast, kinematics, and the development of foliations and lineations in the crust. Journal of Structural Geology 24, 1065-1085.

Grasemann, B., Dabrowski, M., 2015. Winged inclusions: Pinch-and-swell objects during high-strain simple shear. Journal of Structural Geology 70, 78-94.

Griera, A., Bons, P.D., Jessell, M.W., Lebensohn, R.A., Evans, L., Gomez-Rivas, E., 2011. Strain localization and porphyroclast rotation. Geology 39, 275-278.

Griera, A., Llorens, M.-G., Gomez-Rivas, E., Bons, P.D., Jessell, M.W., Evans, L.A., Lebensohn, R., 2013. Numerical modelling of porphyroclast and porphyroblast rotation in anisotropic rocks. Tectonpophysics 587, 4-29.

Hanmer, S., Passchier, C.W., 1991. Shear sense indicators: a review. Geological Survey of Canada 90, 1–71.

Hobbs, B., Regenauer-Lieb, K., Ord, A., 2008. Folding with thermal-mechanical feedback. Journal of Structural Geology 30, 1572-1592.

Houseman, G., Barr, T., Evans, L., 2008. Basil: stress and deformation in a viscous material. In: Bons, P.D., Koehn, D., Jessell, M.W. (Eds.), Microdynamics Simulation. In: Lecture Notes in Earth Sciences 106. Springer, Berlin.

Hudleston, P.J., Lan, L., 1993. Information from fold shapes. Journal of Structural Geology 15, 253-264.

Hudleston, P.J., Lan, L.B., 1994. Rheological control on the shapes of single-layer folds. Journal of Structural Geology 16, 1007-1021.

Hudleston, P.J., Treagus, S.H., 2010. Information from folds: A review. Journal of Structural Geology 32, 2042-2071.

Jansen, D., Llorens, M.-G, Westhoff, J., Steinbach, F., Kipfstuhl, S., Bons, P.D., Griera, A., Weikusat, I., 2016. Small-scale disturbances in the stratigraphy of the NEEM ice core:

observations and numerical model simulations. The Cryosphere 10, 359-370.

Jeffery, G.B., 1922. The motion of ellipsoidal particles immersed in a viscous fluid. Proceedings of the Royal Society of London Series A 102, 161-179.

Jessell, M., Bons, P.D., Evans, L., Barr, T., Stüwe, K., 2001. Elle: the numerical simulation of metamorphic and deformation microstructures. Computers & Geosciences 27, 17-30.

Jessell, M.W., Siebert, E., Bons, P.D., Evans, L., Piazolo, S., 2005. A new type of numerical experiment on the spatial and temporal patterns of localization of deformation in a material with a coupling of grain size and rheology. Earth and Planetary Science Letters 239, 309-326.

Jessell, M.W., Bons, P.D., Griera, A., Evans, L.A., Wilson, C.J.L., 2009. A tale of two viscosities. Journal of Structural Geology 31, 719-736.

Jezek, J., 1994. Software for modeling the motion of rigid triaxial ellipsoidal particles in viscous-flow. Computers & Geosciences 20, 409-424.

Jiang, D. 2016. Viscous inclusions in anisotropic materials: Theoretical development and perspective applications. Tectonophysics 693, 116–142.

Kamb, W. B. 1972. Experimental recrystallization of ice under stress. American Geophysical Union Monograph 16, 221-241.

Kaus, B.K.P., Podladchikov, Y.Y., 2006. Initiation of localized shear zones in viscoplastic rocks. Journal of Geophysical Research 111, B04412, doi : 10.1029/2005JB003652.

Kirby, S.H., 1983. Rheology of the lithosphere. Reviews of Geophysics and Space Physics 21, 1458-1487.

Kocher, T., Schmalholz, S.M., Mancktelow, N.S., 2006. Impact of mechanical anisotropy and power-law rheology on single layer folding. Tectonophysics 421, 71–87.

Kocher, T., Mancktelow, N.S., Schmalholz, S.M., 2008. Numerical modelling of the effect of matrix anisotropy orientation on single layer fold development. Journal of Structural Geology 30, 1013-1023.

Kröner, E. 1961. On the plastic deformation of polycrystals. Acta Metallurgica 9, 155-161.

Lebensohn, R.A., 2001. N-site modelling of a 3D viscoplastic polycrystal using fast Fourier transform. Acta Materialia 49, 2723–2737.

Lebensohn, R.A., Brenner, R., Castelnau, O., Rollett, A.D., 2008. Orientation image-based micromechanical modelling of subgrain texture evolution in polycrystalline copper. Acta Materialia 56, 3914–3926.

Lebensohn, R.A., Montagnat, M., Mansuy, P., Duval, P., Meysonnier, J., Philip, A., 2009. Modeling viscoplastic behavior and heterogenous intracrystalline deformation of columnar ice polycrystals. Acta Materialia 57, 1405-1415.

Lister, G.S., Paterson, M.S., Hobbs, B.E., 1978. The simulation of fabric development during plastic deformation and its application to quartzite: the model. Tectonophysics 45, 107-158.

Llorens, M.-G., Bons, P.D., Griera, A., Gomez-Rivas, E., 2013a. When do folds unfold during progressive shearing? Geology 41, 563-566.

Llorens, M.-G., Bons, P.D., Griera, A., Gomez-Rivas, E., 2013b. Single layer folding in simple shear. Journal of Structural Geology 50, 209-220.

Llorens, G.-M., Griera, A., Bons, P.D., Lebensohn, R.A., Evans, L.A., Jansen, D., Weikusat, I. 2016a. Full-field predictions of ice dynamic recrystallisation under simple shear conditions. Earth and Planetary Science Letters 450, 233-242.

Llorens, G.-M., Griera, A., Weikusat, I., Bons, P.D., Roessiger, J., Lebensohn, R.A. 2016b. Dynamic recrystallisation of ice aggregates during co-axial viscoplastic deformation: a numerical approach. Journal of Glaciology 62, 359-377.

Llorens, M.-G., Griera, A., Steinbach, F., Bons, P.D., Gomez-Rivas, E., Jansen, D., Roessiger, J., Lebensohn, R.A., Weikusat, I., 2017. Dynamic recrystallization during deformation of polycrystalline ice: insights from numerical simulations. Philosophical Transactions Series A: Mathematical, physical, and engineering sciences 375, 2086, doi: 10.1098/rsta.2015.0346.

Mancktelow, N.S., 1999. Finite-element modelling of single-layer folding in elastoviscous materials; the effect of initial perturbation geometry. Journal of Structural Geology 21, 161-177.

Mancktelow, N.S., 2011. Deformation of an elliptical inclusion in two-dimensional incompressible power-law viscous flow. Journal of Structural Geology 33, 1378-1393.

Mancktelow, N.S., 2013. Behaviour of an isolated rimmed elliptical inclusion in 2D slow incompressible viscous flow. Journal of Structural Geology 46, 235-254.

Mandal, N., Samanta, S.K., Chakraborty, C., 2000. Progressive development of mantle structures around elongate porphyroclasts: insights from numerical models. Journal of Structural Geology 22, 993-1008.

Marmo, B.A., Wilson, C.J., 1998. Strain localisation and incremental deformation within ice masses, Framnes Mountains, east Antarctica. Journal of Structural Geology 20, 149-162.

Marques, F.O., Taborda, R., Antunes, J., 2005a. Influence of a low-viscosity layer between rigid inclusion and viscous matrix on inclusion rotation and matrix flow: a numerical study. Tectonophysics 407, 101-115.

Marques, F.O., Taborda, R., Bose, S., Antunes, J., 2005b. Effects of confinement on matrix

flow around a rigid inclusion in viscous simple shear: insights from analogue and numerical modelling. Journal of Structural Geology 27, 379-396.

Marques, F.O., Mandal, N., Taborda, R., Antunes, J.V., Bose, S., 2014. The behaviour of deformable and non-deformable inculsions in viscous flow. Earth-Science Reviews 134, 16-69.

Montagnat, M., Castelnau, O., Bons, P.D., Faria, S.H., Gagliardini, O., Gillet-Chaulet, F., Grennerat, F., Griera, A., Lebensohn, R.A., Moulinec, H., Roessiger, J., Suquet, P., 2014. Multiscale modeling of ice deformation behavior. Journal of Structural Geology 61, 78-108.

Montési, L.G.J., 2013. Fabric development as the key for forming ductile shear zones and enabling plate tectonics. Journal of Structural Geology 50, 254-266.

Mühlhaus, H.-B., Moresi, L., Hobbs, B., Dufour, F., 2002. Large amplitude folding in finely layered viscoelastic rock structures. Pure and Applied Geophysics 159, 2311–2333.

Passchier, C. W., 1991. The classification of dilatant flow types. Journal of Structural Geology 13, 101-104.

Passchier, C.W., Simpson, C., 1986. Porphyroclast systems as kinematic indicators. Journal of Structural Geology 8, 831–843.

Passchier, C.W., Sokoutis, D., 1993. Experimental modelling of mantle porphyroclasts. Journal of Structural Geology 15, 895-909.

Passchier, C.W., Trouw, R.A.J., 2005. Deformation mechanisms. Microtectonics, Springer, Berlin.

Passchier, C.W., Trouw, R.A.J., Zwart, H.J., Vissers, R.L.M., 1992. Porphyroblast rotation - Eppur-Si-Muove. Journal of Metamorphic Geology 10, 283-294.

Piazolo, S., Jessell, M.W., Bons, P.D., Evans, L., Becker, J.K., 2010. Numerical simulations of microstructures using the Elle platform: A modern research and teaching tool. Journal of the Geological Society of India 75, 110-127.

Platt, J.P., 1984. Secondary cleavages in ductile shear zones. Journal of Structural Geology 6, 439-442.

Platt, J.P., Vissers, R.L.M., 1980. Extensional structures in anisotropic rocks. Journal of Structural Geology 2, 397-410.

Platt, J.P., Behr, W.M., 2011. Grainsize evolution in ductile shear zones: Implications for strain localization and the strength of the lithosphere. Journal of Structural Geology 33, 537-550.

Ramberg, H., 1962. Contact strain and folding instability of a multilayered body under compression. Geologische Rundschau 51, 405-439.

Ramsay, J.G., Huber, M.I., 1987. The Techniques of modern structural geology, vol. 2: Folds and Fractures. Academic Press, London.

Schmalholz, S.M., 2006. Finite amplitude folding of single layers: elastica, bifurcation and structural softening. Philosophical Magazine 86, 3393-3407.

Schmalholz, S.M., Maeder, X., 2012. Pinch-and-swell structure and shear zones in viscoplastic layers. Journal of Structural Geology 37, 75-88.

Schmalholz, S.M., Mancktelow, N.S., 2016. Folding and necking across the scales: a review of theoretical and experimental results and their applications. Solid Earth 7, 1417-1465.

Schmalholz, S.M., Podladchikov, Y., 1999. Buckling versus folding: Importance of viscoelasticity. Geophysical Research Letters 26, 2641–2644.

Schmalholz, S.M., Podladchikov, Y.Y., Schmid, D.W., 2001. A spectral/finite difference method for simulating large deformations of heterogeneous, viscoelastic materials. Geophysical Journal International 145, 199–208.

Schmid, D.W., Podladchikov, Y.Y., 2005. Mantled porphyroclast gauges. Journal of Structural Geology 27, 571-585.

Schrank, C.E., Handy, M.R., Fusseis, F., 2008. Multiscaling of shear zones and the evolution of the brittle-to-viscous transition in continental crust. Journal of Geophysical Research: Solid Earth 113, doi: 10.1029/2006JB004833.

Steinbach, F., Bons, P.D., Griera, A., Jansen, D., Llorens, M.-G., Roessiger, J., Weikusat, I., 2016. Strain localisation and dynamic recrystallisation in the ice-air aggregate: A numerical study. The Cryosphere 10, 3071-3089.

Steinbach, F., Kuiper, E.J.N., Eichler, J., Bons, P.D., Drury, M.R., Griera, A., Pennock, G.M., Weikusat, I., 2017. The Relevance of Grain Dissection for Grain Size Reduction in Polar Ice: Insights from Numerical Models and Ice Core Microstructure Analysis. Frontiers in Earth Science 5, 66, doi: 10.3389/feart.2017.00066.

Taylor, G.I., 1938. Plastic strain in metals. J. Inst. Metals, 62, 307-324.

ten Grotenhuis, S.M., Passchier, C.W., Bons, P.D,. 2002. The influence of strain localisation on the rotation behaviour of rigid objects in experimental shear zones. Journal of Structural Geology 24, 485-499.

Treagus, S.H., 1982. A new isogon-cleavage classification and its application to natural and model fold studies. Geological Journal 17, 49-64.

Tullis, J., Yund, R.A., 1985. Dynamic recrystallization of feldspar: a mechanism for ductile shear zone formation. Geology 13, 238-241.

Viola, G., Mancktelow, N.S., 2005. From XY tracking to buckling: axial plane cleavage fanning and folding during progressive deformation. Journal of Structural Geology 27,

409-417.

Watkinson, A.J., 1983. Patterns of folding and strain influenced by linearly anisotropic bands. Journal of Structural Geology 5, 449-454.

Weijermars, R., 1992. Progressive deformation in anisotropic rocks. Journal of Structural Geology 14, 723-742.

White, S., 1979. Large strain deformation: report on a tectonic studies group discussion meeting held at Imperial College, London on 14 November 1979. Journal of Structural Geology 1, 333-339.

Wilson, C.J.L., 1984. Shear bands, crenulations and differentiated layering in ice-mica models. Journal of Structural Geology 6, 303-319.

Zhang, Y., Hobbs, B.E. Jessell, M.W., 1993. Crystallographic preferred orientation development in a buckled single layer: a computer simulation. Journal of Structural Geology 15, 265-276.

Zhang, Y., Mancktelow, N.S., Hobbs, B.E., Ord, A., Mühlhaus, H.B., 2000. Numerical modelling of single-layer folding: clarification of an issue regarding the possible effects of computer codes and the influence of initial irregularities. Journal of Structural Geology 22, 1511-1522.

Chapter 5

Shear localisation in anisotropic materials: a numerical study

Tamara de Riese[1], Lynn Evans[2], Enrique Gomez-Rivas[3,4], Albert Griera[5], Ricardo A. Lebensohn[6], Maria-Gema Llorens[5], **Hao Ran**[1,7], Till Sachau[1], Ilka Weikusat[8], Paul D. Bons[1]

[1]Department of Geosciences, Eberhard Karls University Tübingen, Tübingen, Germany

[2]School of Earth, Atmosphere and Environmental Sciences, Monash University, Clayton, Victoria, Australia

[3]Department of Mineralogy, Petrology and Applied Geology, University of Barcelona, Barcelona, Spain

[4]School of Geosciences, King's College, University of Aberdeen, Aberdeen, UK

[5]Departament de Geologia, Universitat Autònoma de Barcelona, Barcelona, Spain

[6]Theoretical Division, Los Alamos National Laboratory, USA

[7]School of Earth Sciences and Resources, China University of Geosciences, Beijing, China

[8]Alfred Wegener Institute for Polar and Marine Research, Bremerhaven, Germany

Submitted to *Journal of Structural Geology*, 21 June 2018.

Abstract

Localisation of ductile deformation in rocks is commonly found at all scales from crustal shear zones down to grain scale shear bands. Of the various mechanisms for localisation, mechanical anisotropy has received relatively little attention, especially in numerical modelling. Mechanical anisotropy can be due to dislocation slip-system activity of minerals (e.g. ice or mica) and/or layering in rocks (e.g. bedding, cleavage). We simulated simple-shear deformation of a locally anisotropic, single power-law rheology material up to shear strain of five. Localisation of shear rate in narrow shear bands occurs, depending on the magnitude of anisotropy and the stress exponent. At high anisotropy values, strain-rate frequency distributions become approximately log-normal with heavy, exponential tails. Localisation due to anisotropy is scale-independent and thus provides a single mechanism for a self-organised hierarchy shear bands and zones from the mm- to km-scale. The numerical simulations are compared with the natural case of the Northern Shear Belt at Cap de Creus, NE Spain.

Keywords: shear zones, strain localisation, anisotropy, self-organisation, strain-rate distribution

1. Introduction

Shear localisation is the concentration of deformation in part of the deforming material, usually in planar "shear zones" or, in the case of discrete planes, brittle faults. Here we only address localisation of ductile deformation (i.e. without loss of cohesion), which is a common phenomenon and develops at almost all scales in ductile rocks (Fig. 1), from small-scale shear bands to crustal-scale shear zones (e.g. Berthé et al., 1979; Hanmer and Passchier, 1991; Carreras, 2001; Carreras et al., 2010; Bak et al., 1975; Sørensen, 1983). Shear localisation is variable, from isolated shear zones to anastomosing networks of them (Arbaret et al., 2000; Mitra, 1979; Bell, 1981; Passchier, 1984; Gapais et al., 1987; Fusseis et al., 2006; Schrank et al., 2008; Ponce et al., 2013). The formation of such networks in rocks has been simulated experimentally (e.g. Herwegh and Handy, 1996; Bons and Jessell, 1999; Gomez-Rivas and Griera, 2011; 2012; Gomez-Rivas et al., 2015) and numerically (e.g. Gardner et al., 2017; Meyer et al., 2017).

Despite decades of research, there is on going debate on the mechanisms of shear localisation. Strain softening associated with dynamic recrystallisation can lead to shear localisation (White et al., 1980). For example, by nucleation of new grains with relatively low dislocation densities (Tullis and Yund, 1985; Hirth and Tullis, 1992; Stipp et al., 2002; Fossen and Cavalcante, 2017), by grain boundary migration that lowers dislocation density (Shimizu, 2008; Fossen and Cavalcante, 2017), or by grain-size reduction in the case of grain-size sensitive creep (White et al., 1980; Tullis and Yund, 1985; Behrmann and Mainprice, 1987; Warren and Hirth, 2006). However, questions remain whether grain-size reduction can actually lead to shear localisation (de Bresser et al., 1998, 2001; Platt and Behr, 2011).

Deformation by dislocation-creep mechanisms can soften the rock due to the formation of a lattice-preferred orientation (LPO) if deformation rotates slip planes into favourable orientations (Poirier, 1980; Mainprice et al., 1986; Ji et al., 2004; Passchier and Trouw, 2005; Warren et al., 2008; Oliot et al., 2014; Fossen and Cavalcante, 2017; Llorens et al., 2016a,b; 2017). This is a form of geometric weakening, in which the internal geometry of the material changes with strain. Geometric weakening also includes the development of a shape-preferred orientation, the re-orientation or redistribution of phases, e.g. alignment of planar minerals (e.g. micas), elongated grains or other components that make up a fabric (Jordan, 1988; Handy, 1990, Shea and Kronenberg, 1993; Johnson et al., 2004). Softening can further be induced by a change of composition, by introduction of a weak phase, such as melt (Brown

and Solar, 1998; Rosenberg and Handy, 2000; Handy et al., 2001) or by reaction softening during metamorphism in which new and, possibly, weaker minerals grow (Poirier, 1980; Mainprice et al., 1986; Ji et al., 2004; Passchier and Trouw, 2005; Regenauer-Lieb et al., 2009; Warren et al., 2008; Oliot et al., 2014; Fossen and Cavalcante, 2017). Introduction of (aqueous) fluids can induce softening by water weakening, enhancing dynamic recrystallization (e.g. fluid-assisted grain boundary migration; Urai, 1983) or enabling dissolution-precipitation creep (Hirth and Tullis, 1992; Mancktelow and Pennacchioni, 2004; Menegon et al., 2008; Oliot et al., 2014; Finch et al., 2015).

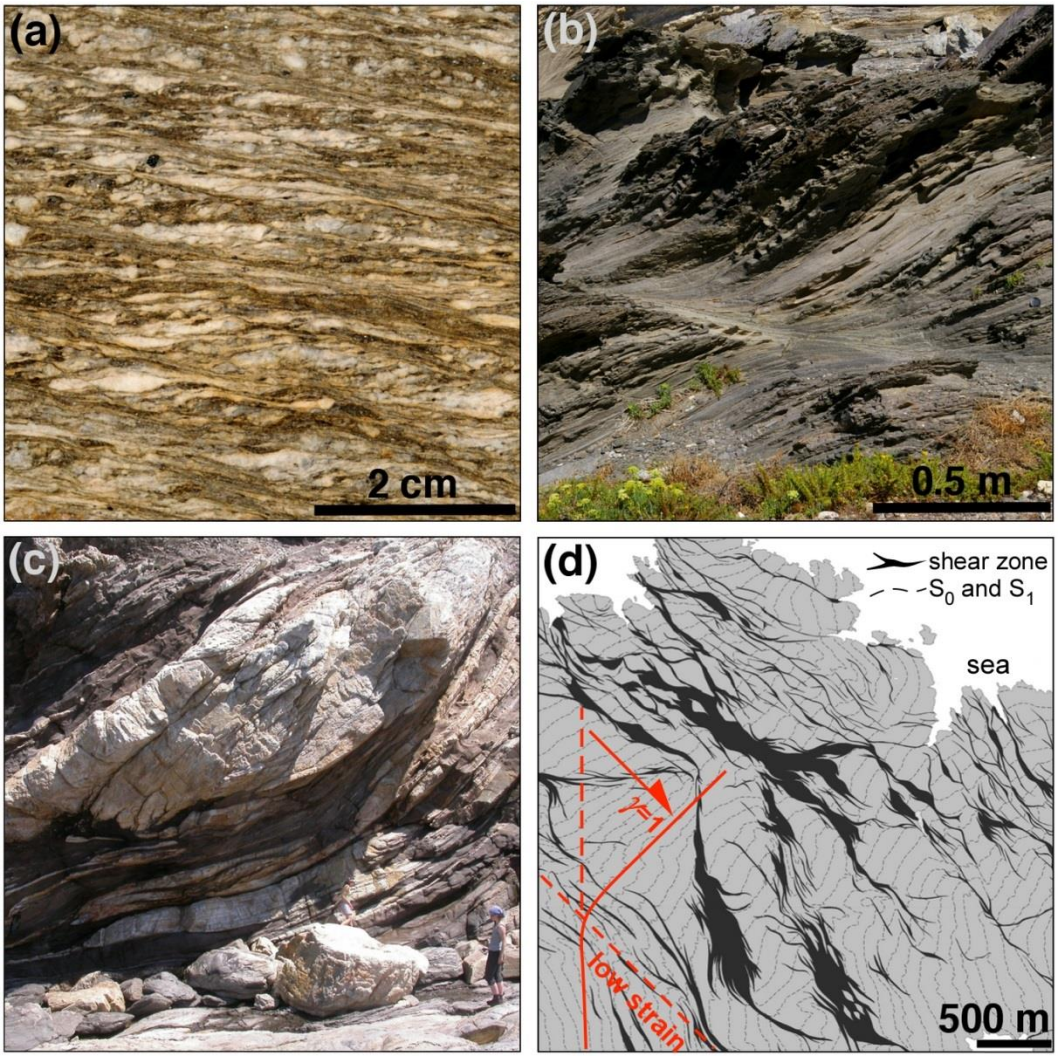

Fig.1. Shear localisation on all scales at Cap de Creus, Eastern Pyrenees, Spain (**a**) Shear bands in deformed granodiorite at the Roses lighthouse (Carreras et al. 2004). (**b**) Shear zone in meta-turbidites at Tudela (Druguet, 1997). **(c)** Large shear zone (note the person in the lower right for scale) at Punta

dels Farallons (Druguet and Hutton, 1998). **(d)** Shear zones (black) in the Northern Cap de Creus shear belt forming an anastomosing pattern. Modified after Carreras (2001). Dashed red line shows the deflection of the bedding and bedding-parallel S_1 cleavage by approximately NW-SE-directed dextral shearing.

Shear heating is an additional mechanism that can soften a deforming rock with a temperature-dependent rheology, leading to shear localisation (Hobbs and Ord, 1988; Thielmann and Kaus, 2012; Thielmann et al., 2015; Thielmann, 2017; Brun and Cobbold, 1980; Bercovici, 1993).

For shear localisation to occur, instabilities must develop that inhibit a homogeneous distribution of deformation. Such instabilities can result from the above-mentioned strain-softening mechanisms, but also from strain hardening (Hobbs et al., 1990). In general, strain-softening processes are able to narrow shear zones (Ben-Zion and Sammis, 2003), whereas strain-hardening processes can widen them (Means, 1984; Hull, 1988; Fusseis et al., 2006; Schrank et al., 2008). Most of the above shear localisation mechanisms assume a localisation of ductile shear with progressive strain. However, the opposite has also been proposed: shear zone initiation on brittle fractures (the extreme end member of localisation) that subsequently widen into ductile shear zones (Segall and Simpson, 1986; Fusseis et al., 2006; Pennacchioni and Mancktelow, 2007; Goncalves et al., 2016).

Shear zones are often arranged in anastomosing networks (Ramsay and Allison, 1979; Bell, 1981; Hudleston, 1999), formed by linking of segments due to accumulated strain and displacement (Schrank et al., 2008; Fossen and Cavalcante, 2017). The Cap de Creus peninsula of the easternmost Pyrenees (Spain) provides an excellent example of such networks (Fig. 1d) (Druguet et al., 1997; Carreras, 2001; Carreras et al., 2004; Fusseis et al., 2006; Schrank et al., 2008). The shear zones developed in medium to high metamorphic-grade biotite schists under retrograde metamorphic conditions (Druguet et al., 1997, 1998). A progressive non-coaxial deformation regime is assumed to be responsible for their development (Carreras, 2001). The shear zones form a complex pattern, as they are linked in an anastomosing framework with self-similar properties (Carreras, 2001). In Cap de Creus one finds localisation structures and anisotropies from the grain scale to the scale of the entire, ca. 4 km wide, Northern Shear Belt (Schrank et al., 2008).

Many studies have addressed scale invariance in geological media (Gutenberg and Richter,

1956; Turcotte, 1990; Turcotte, 1992; Bonnet et al., 2001). Nonlinearity is an essential condition for self-similar (fractal) statistics, which supports the system to be highly dynamical (Turcotte, 1997). Even tectonic plates display fractal distributions up to the largest plates (Bird, 2003; Sornette and Pisarenko, 2003), which can be explained with a dynamical model of plates with creation, fragmentation and destruction acting on all scales (Sornette and Pisarenko, 2003). Shear zone networks often develop over several orders of magnitude (Sammis and Steacy, 1995; Hippertt, 1999; Carreras, 2001; Carreras et al., 2010). Tchalenko (1970) identified similarities between shear zones at different magnitudes (microscopic scale in shear box test, intermediate scale in Riedel experiment, regional scale in earthquake fault), interpreting these in terms of mechanical properties of the material, the failure criterion and deformation kinematics. Fractal analysis of shear bands indicates that shear rates values are multifractal (Poliakov et al., 1994; Poliakov and Herrmann, 1994; Herrmann et al., 1995). Fractal distributions of shear bands that evolve spontaneously from a rather homogeneous strain distribution suggest the existence of some kind of self-organisation (Bak et al., 1987; Turcotte, 1992; Poliakov and Herrmann, 1994), where each shear band may be seen as a single internal "avalanche" on which the system releases stresses through larger displacements (Poliakov and Herrmann, 1994; Herrmann et al., 1995). In numerical simulations and in experiments, shear bands develop without tuning of external control parameters, which is a necessary condition for self-organization (Poliakov and Herrmann, 1994; Poliakov et al., 1994; Ran et al., 2018).

Many properties are known to be highly anisotropic in rocks and materials. When a material deforms anisotropy originates through the development of LPOs and/or SPOs (Mainprice and Nicolas, 1989; Passchier and Trouw, 2005), which can trigger the development of foliations, which in term can result in internal instabilities. During deformation, anisotropic rocks develop internal structures whose geometry depends on the degree and type of anisotropy, from intrinsic to composite (Cobbold et al., 1971; Cosgrove, 1976; Griera et al., 2013; Ran et al., 2018). The lower crust develops a mechanical anisotropy as the result of intrinsic layering, which is enhanced by the anisotropy induced by stretching (Cosgrove, 1997). The shear zones at Cap de Creus (Fig. 1a) could be a result of anisotropy-induced shear localisation, as these have been interpreted as resulting from inherited anisotropies such as meta-turbidite layering, the axial planar S1-foliation, and pegmatite bodies (Druguet et al., 1997; Carreras, 2001; Schrank et al., 2008; Ponce et al., 2013). Furthermore, the degree of anisotropy impacts on, for instance, the geometry of deformed single layers (Toimil and Griera, 2007; Kocher et al., 2008; Llorens et al., 2013a), the reactivation of fault and shear zones (Tommasi et al., 2009)

and on shear zone formation over pre-existing fabrics (Michibayashi and Mainprice, 2004).

Although anisotropy has been recognised as an important factor in the formation of geological structures, relatively few numerical studies have included it (see discussion by Ran et al., 2018). Most distinct exceptions are models of folding in anisotropic media (Cobbold, 1976; Latham, 1979; Mühlhaus et al., 2002; Llorens et al., 2013a; 2013b), and the influence of anisotropy on rigid object behaviour (Fletcher, 2004; Fletcher, 2009; Griera et al., 2011, 2013). In most numerical studies anisotropy has been implemented as a composite anisotropy, where the anisotropy results from stacking layers with different, but isotropic rheologies (see Hudleston and Treagus (2010), and references therein; Dabrowsky and Schmid, 2011). Few studies have utilized an intrinsic anisotropy, where the rheology of the material itself is anisotropic (Lebensohn, 2001; Griera et al., 2013). Here we present a series of numerical simulations to investigate strain (rate) localisation due to mechanical anisotropy. We aim to quantify the amount of localisation, which can emerge in a single-phase material as a function of degree of anisotropy. We use the same approach to model an intrinsically anisotropic material as in Griera et al. (2013), with the parameter defining anisotropy comparable to the ratio between normal and shear viscosity, as defined in Kocher et al. (2006; 2008). The simulations aim to quantify the amount of localisation as a function of the degree of anisotropy and allow making predictions on the expected volume fraction of material that experiences high strains, recognisable as shear zones, in deforming rocks and ice sheets.

2. Methods

In order to determine how mechanical anisotropy affects the amount of localisation, we simulate the deformation of a material with an intrinsic mechanical anisotropy. The crystallographic orientation can evolve with progressive deformation and vary within the model.

2.1 The VPFFT-ELLE modelling platform

We use the viscoplastic full-field formulation (VPFFT) based on the Fast Fourier Transforms coupled with the modelling platform ELLE (Lebensohn, 2001; Lebensohn et al., 2008; Griera et al., 2011, 2013; Llorens et al., 2016a; Steinbach et al., 2016) to calculate the stress and strain rate distribution during progressive simple shear. ELLE is an open-source modelling platform (http://www.elle.ws; Jessell et al., 2001; Bons et al., 2008) and aims to provide a generalized framework for the numerical simulation of the evolution of microstructures during

deformation and metamorphism. The VPFFT+ELLE code has recently been used to simulate recrystallisation in deforming ice and halite (Llorens et al., 2016a,b; Llorens et al. 2017; Gomez-Rivas et al., 2017; Steinbach, 2016, 2017), viscoplastic deformation of hard inclusions (Griera et al., 2011, 2013; Ran et al., 2018) and folding in anisotropic materials (Bons et al., 2016; Jansen et al., 2016; Ran et al., 2018).

2.2 Definition of the model

Our 2D models consist of unconnected nodes (*unodes*), which provide a high-resolution regular grid for storing physical properties such as lattice orientation (defined by three Euler angles), stresses and strain rates. The *unodes* effectively represent crystallites or single grains with a constant internal lattice orientation. We use a second, non-regular, layer of *unodes* as a passive marker grid to visualise the finite deformation field. The passive marker grid is initially oriented vertical in all cases.

2.3 Viscoplastic deformation using the full-field approach

The VPFFT approach calculates a strain rate and stress field that minimize the average local work rate and satisfies the constitutive relation at local level, under the constraints of strain compatibility and stress equilibrium (see Lebensohn (2001), Lebensohn et al. (2008; 2009) and Montagnat et al. (2014) for a more detailed description of the theoretical framework and numerical algorithm, and Griera et al. (2013) and Llorens et al. (2016a,b) for the coupling with ELLE). The "full field" designation indicates that the approach explicitly resolves velocity and stress fields with a resolution that is defined by the size, *S*x*S*, of the *unode* or Fourier grid.

We simulate the anisotropic behaviour using a nonlinear viscous rate-dependent approach, where deformation is assumed to be accommodated by dislocation glide only, taking into account the different available slip systems and their critical resolved shear stresses (τ) (Lebensohn, 2001). The constitutive equation for the relation between strain rate $\dot{\varepsilon}_{ij(x)}$ and the deviatoric stress $\sigma'(x)$ at position *x* of the Fourier grid is given by

$$\dot{\varepsilon}_{ij}(x) = \sum_{s=1}^{N_s} m_{ij}^s(x)\dot{\gamma}^s(x) = \dot{\gamma}_0 \sum_{s=1}^{N_s} m_{ij}^s(x)\left|\frac{m^s(x):\sigma'(x)}{\tau^s(x)}\right|^n \operatorname{sgn}\left\{m^s(x):\sigma'(x)\right\}, \quad (1)$$

where the sum runs over all (N_s) slip systems (*s*) in the crystal, m^s is the symmetric Schmid tensor, τ^s is the critical resolved shear stress, $\dot{\gamma}^s$ is the shear strain rate, $\dot{\gamma}_0$ is the reference strain rate and n is the stress exponent. We use the same hexagonal crystal symmetry of ice 1h as in Llorens et al. (2016a, 2016b, 2017), Griera et al. (2011; 2013) and Ran et al. (2018) for our single-phase material, in which deformation is allowed to be accommodated by glide along the basal plane and non-basal, pyramidal and prismatic planes (Griera et al., 2013). The degree of anisotropy, *A*, is defined as the ratio between the critical resolved shear stresses of the basal and non-basal slip systems:

$$A = \frac{\tau^{(non-basal)}}{\tau^{(basal)}}. \quad (2)$$

Each deformation step, the VPFFT code calculates the stress and velocity field for the whole model. Velocities are applied for a shear-strain increment of $\Delta\gamma$=0.02. Since the VPFFT code requires a rectangular grid of *unodes*, the ELLE-code subsequently maps the translated material states of the shifted *unodes* (here the Euler angles) back on the original square grid. This routine employs the feature that the data structures of both the VPFFT and ELLE codes are fully wrapping. Therefore, a material point that moves across the right boundary enters the model on the left again. This way, the model can be represented by a square box at all times, which allows the modelling up to large strains without changing the outer shape of the model.

2.4 Experimental setup

We use square *S*x*S* models with *S* a power of two *unodes*. Each individual simulation considers a single material that is defined by its anisotropy, with $A \geq 1$, and τ^{basal} is always set to unity. Each *unode* in the model is initially assigned a random lattice orientation. We simulate the deformation of the material in dextral simple shear up to a shear strain of five in strain increments of $\Delta\gamma$=0.02. Boundary conditions are such that the velocities at the boundaries are on average simple shear. Three series of simulations are presented here: In series I we varied the anisotropy parameter *A*. With series II we investigate the impact of different model sizes *S* on strain rate localisation. In series III we varied *n* from one to four,

and set *A* such that the effective viscosity ratio for non-basal and basal slip is 4096.

Table 1. Simulation parameter

Series name	Anisotropy (*A*)	Stress exponent (*n*)	Size (*SxS*)
Series I	1, 4, 16. 64	3	512
Series II	16	3	128, 256, 512
Series III	8, 16, 64, 4096	1, 2, 3, 4	256

2.5 Data visualisation

Stress and strain rate distributions are visualised by mapping the normalised Von Mises strain rates ($\dot{\varepsilon}_{vm}$) and Von Mises stresses (σ_{vm}) (Fig. 2a-c), which are the second invariants of the symmetric strain rate and stress tensors respectively:

$$\dot{\varepsilon}_{VM} = \sqrt{\tfrac{2}{3}\dot{\varepsilon}_{ij}\dot{\varepsilon}_{ij}} \quad \text{and} \quad \sigma_{VM} = \sqrt{\frac{2}{3}\sigma_{ij}\sigma_{ij}}. \qquad (3)$$

To visualise the finite-strain field, we use a passive marker grid (Fig. 2d). This passive marker grid tracks the position of *unodes*, treated as passive material markers, which were initially arranged on an orthogonal grid. The bulk stress is calculated by averaging all stresses of individual *unodes*. Lattice orientations are visualised by mapping the Euler-ϕ angles, i.e. the azimuth of the c-axis relative to the vertical axis (Fig. 2e). Frequency distributions of Euler-ϕ angles show the preferred orientation of c-axis (Fig. 2f).

2.6 Strain Localisation

We quantify the strain-rate localisation (*L*) in our model with a localisation factor defined by Sornette et al. (1993) and Davy et al. (1995), and modified by Gomez-Rivas (2008), Steinbach et al., (2016) and Llorens et al. (2017):

$$L = 1 - \frac{\left(\sum_{n_i}^{n_t} \dot{\varepsilon}_{VM}\right)^2}{n_t \sum_{n_i}^{n_t} \left(\dot{\varepsilon}_{VM}\right)^2}, \qquad (3)$$

where n_t denotes the total number of *unode*s. The strain localisation factor ranges from 0 to 1, where 0 means homogeneous deformation and 1 maximum localisation, where all strain is

accommodated by a single *unode*.

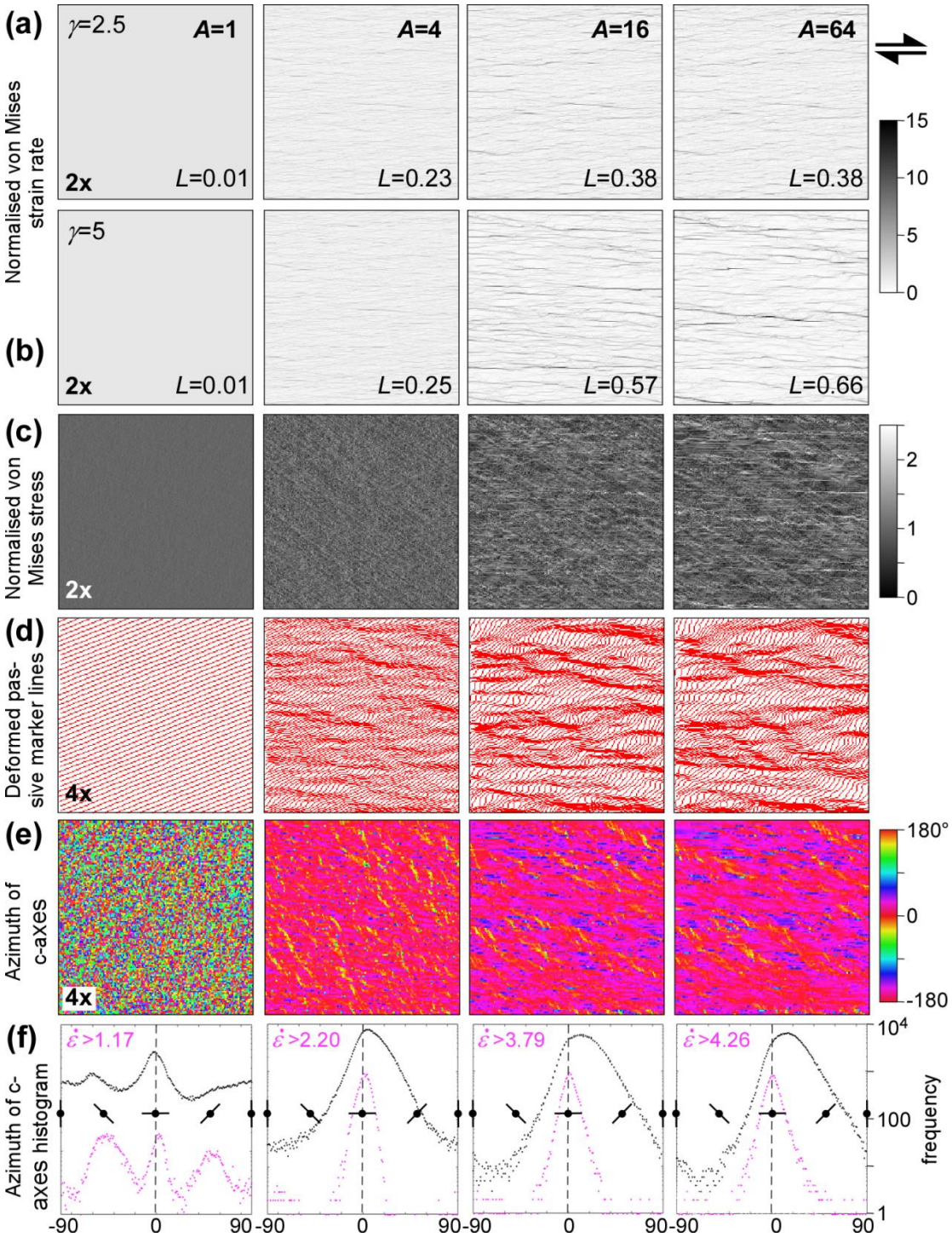

Fig. 2. VPFFT-ELLE simulations (series I) of dextral simple shear up to a shear strain of γ=5. The degree of mechanical anisotropy (*A*) increases from 1 (quasi-isotropic) to 64 (highly anisotropic). Evolution of Von Mises strain-rate field, normalized to the bulk value, at a shear strain of **(a)** γ=2.5 and

(b) γ=5. In both (a) and (b) images have been enlarged 2x only showing the upper left quarter of the model. In the isotropic case (A=1) no strain localisation occurs. In all anisotropic cases sub-horizontal shear bands develop. **(c)** Von Mises stress field at a shear strain rate of γ=5. Highest stress values are within high strain zones. Stripes in the images are attributed to imperfect solutions for the stress field in the iterative VPFFT code. **(d)** Passive marker grid at a shear strain of γ=5 to illustrate the distribution of finite-strain. Images have been enlarged 4x, only showing the upper left part of the model box. **(e)** Orientation of c-axes azimuths (Euler ϕ, or azimuth angle relative to the vertical) at γ=5. This images have been enlarged 4x, only showing the upper left part of the model box. (**f**) Frequency distributions of c-axes azimuths. When separating the high-strain values from the entire model (highest 5% of normalised Von Mises strain rate values) and analyse c-axis orientation within it at γ=5 it becomes apparent that c-axis azimuths are close to perpendicular to the shear plane, but oriented with a broad maximum of 80 ° to the shear plane in the entire model. A linear bin width of 1.8 ° has been used to generate the frequency distributions.

3. Results

Results of Series I show that distinct strain and strain-rate localisation occurs in all cases where A>1 (Fig. 2a-c). Although the material with A=1 is strictly speaking not isotropic, it behaves as an effectively isotropic material (Griera et al., 2011). Stress and strain rates (L<0.01) show very little variation and the finite strain grid consists of straight lines (Fig. 2d). However, Euler-ϕ distributions indicate a maximum in c-axes perpendicular to the shear plane (Fig. 2e,f).

For A>1, the normalised Von Mises strain-rate ($\dot{\varepsilon}_{VM}$) field becomes increasingly heterogeneous with progressive strain (Fig. 2a,b). High strain rate bands oriented at a low angle to the horizontal shear plane are clearly visible (Fig. 2a,b). Localisation of finite strain can be identified in the passive marker grid (Fig. 2d), which shows distinct shear bands for A=16 and A=64, and less localisation for A=4. This reveals that the heterogeneity in strain rate is not averaged out with progressive strain. For all anisotropic cases (A>1), c-axes become preferentially oriented with a broad maximum at about 80 ° to the shear plane (Fig. 2e,f). Within the high strain-rate zones (highest 5% of strain-rate values) the c-axes preferred orientation is stronger with the azimuths of c-axes closer to perpendicular to the shear plane

(Fig. 2f). Material within the shear zones thus has its basal plane well-oriented for the applied bulk simple shear. The strength of the c-axes preferred orientation within the shear zones decreases slightly from A=4 to A=64.

The frequency distribution of strain rates (Fig. 3a,b) for an effectively isotropic material (A=1) at a shear strain of γ=5 is approximately normal. For A>1, the frequency distributions deviate from a normal distribution and shift towards log-normal distributions. Frequency distributions for A=16 and A=64 are almost identical up to a normalised strain rate of about five. However, the frequency distributions become heavy tailed and are therefore not exactly log-normal (Fig. 3b). High strain rate values become overrepresented and have values that are up to ca. 20 times higher than the mean for A=64 (Fig. 3a,b). Therefore, a material with a higher degree of anisotropy reaches significantly higher strain-rate values due to strain localisation. As a result, a major part of the material deforms at a significantly lower rate than the mean strain rate, as can be seen by the leftward shift of the frequency peak (Fig. 3a,b). The inset in figure 3b shows the localisation factor (L) plotted against the anisotropy parameter, and illustrates that localisation increases from A=1 to A=16, although localisation increases very little from A=16 to A=64.

When comparing the frequency distributions of Von Mises strain rate for different model sizes (S) in Series II, we observe that the shape of the $\dot{\varepsilon}_{VM}$ frequency distribution is largely independent of S (Fig. 3c). For example, the probability to reach a particular strain rate $f(\dot{\varepsilon}_{VM})$, for a 512x512 model is four times higher than that for a simulation with 256x256 *unodes*, and 16 times higher than that for a simulation with 128x128 *unodes*. The ratio R, defined as

$$R = \frac{f_{\left(\dot{\varepsilon}_{VM},S_1\right)} / f_{\left(\dot{\varepsilon}_{VM},S_2\right)}}{\left(S_1 / S_2\right)^2}, \qquad (5)$$

is approximately unity (inset in Fig. 3c). The highest strain rates that are achieved in a simulation do, however, depend on S. The frequency of $\dot{\varepsilon}_{VM}$ =15 is about one per 512x512 *unodes* (i.e. =262,144 unodes) for A=16 and γ=5. This means that the chance that one *unode* with $\dot{\varepsilon}_{VM}$ =15 occurs in a 128x128 *unode* model is only 1/16 or about 6%.

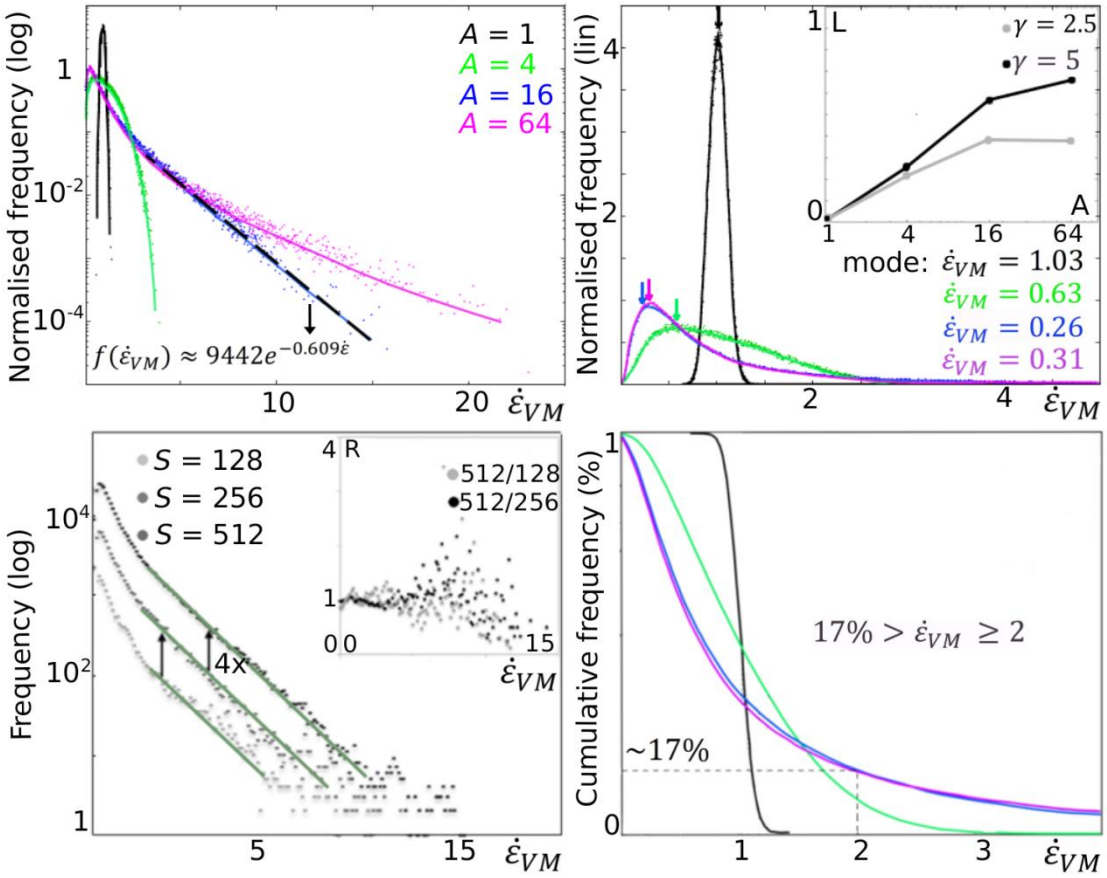

Fig. 3. Frequency distributions of normalised Von Mises strain rates at a shear strain rate of γ=5. Normalised frequency distributions of normalised Von Mises strain rate in **(a)** log-linear and **(b)** linear scaling, for anisotropy parameters of A = 1, 4, 16 and 64 (series I). Frequency distributions have been processed with linear bin widths of 0.002 (for A=1), 0.008 (A=4), 0.031 (A=16) and 0.048 (A=64). For the isotropic material (A=1) the frequency distribution is approximately normal with the mode slightly above one. Modes are indicates by arrows. Higher anisotropy leads to data peaks which are below the mean, whereas the high strain rate values develop a heavy tail, which becomes more pronounced with increasing A. Inset in **(b)** shows the localisation factor L plotted against A *(*for γ = 2.5 and γ = 5*)*, illustrating an increase of localisation from A=1 to A=16, though the intensity of localisation increases very little from A=16 to A=64. **(c)** Frequency distribution for different model sizes (Series II; 128x128, 256x256, 512x512 *unodes*). To be able to compare the different data sets, a linear bin size of 0.1 has been used to calculate the frequency distributions. As one can see, for a system size of 512 by 512 *unodes* the frequency of Von Mises strain rate values appears four times more often than for a systems with a size of 256 by 256 *unodes*, and 16 times more often than for a system with 128 by 128 *unodes*.

Inset in (c) shows the ratio *R*, which compares frequency distributions of Von Mises strain rate for different model sizes. **(d)** Cumulative frequency distribution of the same data set as in (a) and (b).

Plots of Von Mises stresses (σ_{VM}) against normalised Von Mises strain rates ($\dot{\varepsilon}_{VM}$) (for each *unode*, at γ=5) show a large scatter that increases with *A* (Fig. 4). This means that both $\dot{\varepsilon}_{VM}$ (Fig. 3) and σ_{VM} values become increasingly variable with increasing *A*. The scatter for each simulation has a lower bound, with an exponent *n*=3, that is defined by $\tau^{(non\text{-}basal)}$. Material points on this bound deform by non-basal glide. The upper bound is defined by $\tau^{(basal)}$ and material points that plot here deform by basal glide. With increasing *A*, the cloud moves to the right, because $\tau^{(basal)}$ is always one, while $\tau^{(non\text{-}basal)}$ corresponds to *A*.. One also sees that fewer points reach the upper basal-glide-only bound with increasing *A*. Figure 4 shows that $\dot{\varepsilon}_{VM}$ and σ_{VM} do correlate, but rather poorly. High-σ_{VM} zones are visible in the σ_{VM} distribution at high *A* (Fig. 2c) and correlate to some extent with high $\dot{\varepsilon}_{VM}$ zones.

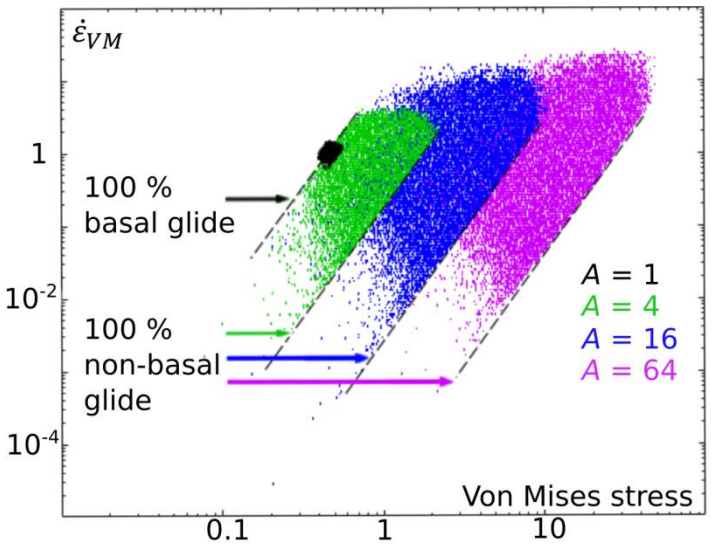

Fig. 4. Normalised Von Mises strain rate (normalised to bulk value) plotted against Von Mises stress at a shear strain rate of γ=5 for series I. Data plot in the form of a cloud, that spreads with increasing *A*. The bottom right side of each cloud plots as straight line with a slope of *n*=3. For *A*=4 the top left bound is a straight line as well. Points on the upper straight line are those with 100% basal glide, points on the lower bound are those with 100% non-basal glide. Since basal glide is set to unity for all cases, the bound for basal glide is the same for all *A*. Non-basal glide is set to 1, 4, 16 and 64, resulting in a

rightward shift of the lower bound. For *A*=16 and *A*=64 the upper left 100% basal glide is not reached. This can be explained by the fact that 100% basal glide means is effectively an extremely soft *unode*, which, however, cannot deform freely, since it is constrained by its surroundings.

Results of Series III (Fig. 5) show distinct strain localisation for *n*>1 at γ=5 (Fig. 5a). The localisation factor increases with *n*, from *L*=0.22 for *n*=1 to *L*=0.56 for *n*=4, with only minor increase from *n*=3 to *n*=4 (Fig. 5a). The plot of Von Mises stresses (σ_{VM}) against normalised Von Mises strain rates ($\dot{\varepsilon}_{VM}$) (Fig. 5b) (for each *unode*, at γ=5) show largest scatter for runs with *n*=3 and *n*=4. With decreasing *n* and increasing *A* the scatter becomes less wide in the direction of strain rate, but reaches higher stress values (Fig. 5b). The non-basal bound is reached in all cases, but the basal bound never. When comparing normalised frequency distributions of normalised Von Mises strain rate for Series III (Fig. 5c), we observe that the mode shifts to the left for higher *n*. For *n*=1 and *A*=4096 the frequency plots as a shifted log-normal distribution. For *n*=2 to *n*=4 the frequency distribution plots approximately exponential, with a slightly higher tendency to evolve a heavy tail for higher *n* values.

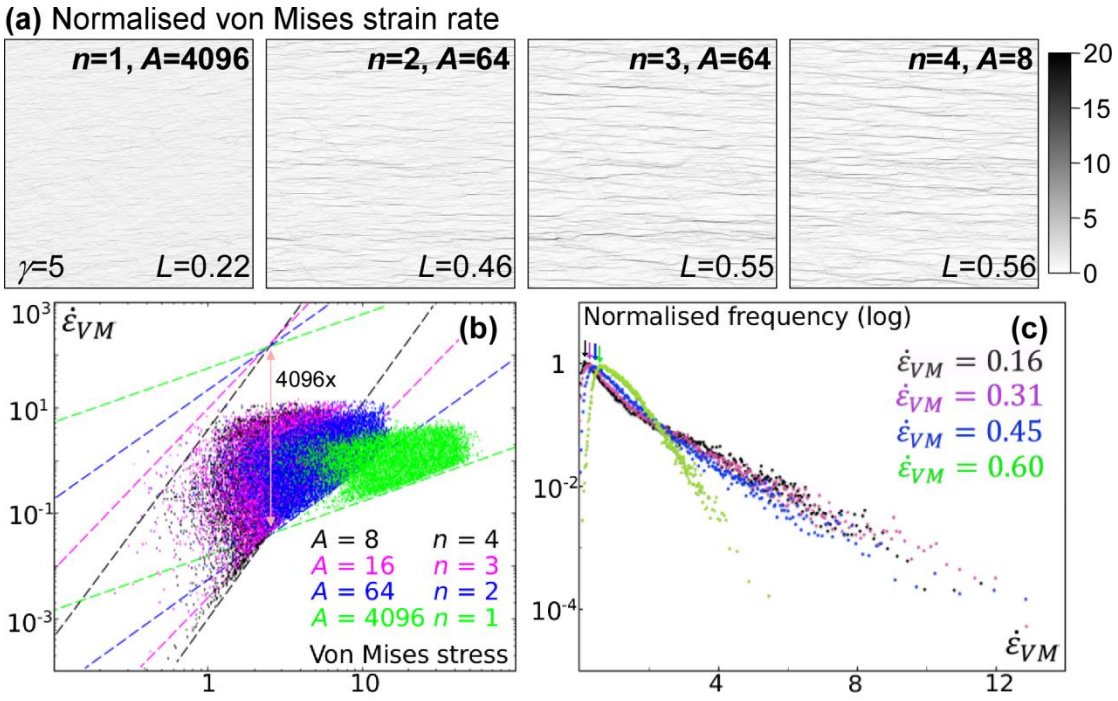

Fig. 5. Results for series III **(a)** Distribution of Von Mises shear strain rates, normalized to the bulk value, at a shear strain of γ=5. For *n*=1 and *A*=4096 only minor localisation is visible. For *n*>1 and A<4096 the localisation factor increases with increasing *n* and decreasing *A*, with most strain

localisation for n=4 and A=8, with only a minor difference to n=3. **(b)** Von Mises strain rate (normalised to bulk value) plotted against Von Mises stress at a shear strain rate of γ=5. The bottom right side of each cloud plots as straight line in log-log with a slope of n is 1 to 4, where the dashed lines indicate the stress exponents of n=1 to 4 in corresponding colours respectively. The upper bound is a straight line with the same slope, but is never reached in any of the simulations. The pink arrow indicates maximum range of possibly reachable Von Mises strain rate values, which is always A^n=4096. **(c)** Normalised frequency distribution of normalised Von Mises strain rates at a shear strain rate of γ=5 in a log-linear plot. Arrows indicate mode of normalised Von Mises strain rate for different configurations, which shift to the left with increasing n and decreasing A. For n=1 the frequencies have a shifted log-normal distribution. For n=2 to 4 the frequency distribution are approximately exponential, with a slightly higher tendency for a heavy tail at higher n values. Normalised frequency distributions have been calculated with linear bins of 0.022 for n=1, 0.052 for n=2, 0.056 for n=3 and 0.046 for n=4.

4. Discussion

The simulations indicate that mechanical anisotropy leads to distinct strain and strain-rate localisation into networks of sub-parallel shear bands, with the intensity depending on the degree of anisotropy and the stress exponent. Frequency distributions of Von Mises strain rates show heavy tails for high A, with an approximately exponential decrease in frequency of high $\dot{\varepsilon}_{VM}$ values (Fig. 3). These distributions emphasise the continuous nature of the $\dot{\varepsilon}_{VM}$ distributions, only cut off by the model resolution. Although a visual inspection of strain-rate and finite strain distributions (Fig. 1,2) suggests the presence of distinct shear zones or bands, the results indicate there is actually no sharp distinction between low and high strain (rate), but, instead, a continuum.

Llorens et al. (2017) used the same VPFFT+ELLE approach as in this study to simulate the deformation of ice. A_{ice} is assumed to range between 60 and 100 for n=3 for basal slip system and n=2 for non-basal slip systems (Duval et al., 1983), but Llorens et al used A_{ice}=20 to speed up calculation time and n=3 for all slip systems. This appears permissible if determining the amount of localisation is not the main aim of the study, as our A=16 and A=64 results are quite similar. In our simulations, each *unode* can be regarded as representing a single grain with a single, homogeneous lattice orientation. Llorens et al. (2017) modelled

grains composed of many *unodes* and incorporated dynamic recrystallisation. Yet, they also observed strong strain (rate) localisation. When comparing our results with those from Llorens et al. (2017) one observes that although we use no dynamic recrystallisation we get a localisation factor ($L \approx 0.38$ at $\gamma = 2.5$) that is similar to that of a polycrystalline material with minor recrystallisation. Our results (without recrystallisation and substructures within grains) would thus overestimate the amount of localisation (for a given A) in very pure ductily deforming materials that flow at slow rates (such as ice sheets). When, however, the contribution of recrystallisation is suppressed by high strain rates, impurities and/or the presence of multiple minerals (as is common in rocks), our simulations may give an indication of the amount of strain localisation that can be expected.

Heavy tailed frequency distributions are often assumed to indicate underlying self-similar (fractal) processes (e.g. Bons and van Milligen, 2001; Brunetti, 2009). Such distributions are usually approximately log-normal, with or without a power-law or exponential tail, depending on small changes in model assumptions (Hähner et al., 1996; 1998; Mandelbrot, 1997; Mandelbrot, 2001; Mitzenmacher, 2004). The frequency distributions of strain rates (Fig. 3) as well as their spatial distributions (Fig. 2a,b) support the notion that strain (rate) localisation is self-similar. Between the most conspicuous shear zones, one can discern less distinct shear zones as well. The same was proposed for the pattern of shear localisation at Cap de Creus (Fig. 1, and Carreras, 2001). Shear localisation happens on all scales, making cm-scale shear bands (Fig. 2d) small versions of the larger shear zones that contain them (e.g. Hippertt, 1999; Carreras, 2001).

The scale-independence of the strain rate distributions (as a result of anisotropy; Fig. 3c) has a major advantage that the models can be used for predictions on scales well beyond the limited scales of our computer models (due to limited computing time and memory capacity). If we assume that $A=16$ is representative of the schists at Cap de Creus that have a strong layer-parallel foliation, defined by aligned biotite (Druguet et al., 1997; Carreras, 2001). 17% of the area shown in Fig. 1d is mapped as "shear zone" by Carreras et al. (2004), i.e. material with distinctly higher strain than the rest of the outcrops. The cumulative strain-rate distribution indicates that, at $A \geq 16$, 17% of the material has a strain rate of ≥ 2 times the average (Fig. 3d), which itself is about three to four times the mode (Fig. 3b). Deformation in the area shown in Fig. 1d is approximately NW-SE directed dextral simple shear with a transpressive component (Druguet et al., 1997; Carreras, 2001; Druguet, 2001; Bons et al., 2004). The general trend of the subvertical bedding and parallel S_1 foliation rotates about 45° relative to the low-strain area in the SW-corner. Shear strain in the most abundant (≈83%),

non-shear-zone areas (i.e. lozenges) is thus in the order of unity. Assuming that this $\gamma \approx 1$ is the mode, the 17% of the area that is mapped as shear zone would then have a shear strain of at least six to eight. Such shear strains would indeed warrant mapping them as shear zone. The average shear strain would be about three to four. The aim of this comparison with Cap de Creus here is not to exactly determine the amount of strain. This would require a more extensive analysis of the area, and consideration of other, additional localisation mechanisms. Future work also needs the address how the instantaneous strain-rate distribution relates to that of the finite strain (compare Fig. 2b and d).

Shear localisation due to anisotropy appears almost inevitable when A is large enough (here roughly $A \geq 4$ at $n \geq 3$). Localisation arises from the non-linear (both A and $n > 1$) constitutive law (Ord and Hobbs, 2018). Our results indicate that localisation is self-similar and does not average out over large scales or large strain increments. One reason for the lack of a characteristic scale is that the property anisotropy has no length scale. This sets localisation due to anisotropy apart from localisation mechanisms that do incorporate a length scale, such as shear heating (only effective at scales above the heat-diffusion length; e.g. Thielmann et al., 2015) and microstructural processes, such as grain-size reduction (e.g. de Bresser et al., 2001). Such mechanisms do not result in scale invariance and do not provide a single mechanism for the localisation of shear in small shear bands within larger shear zones.

Although the published range of strain localisation mechanisms can certainly all operate in rocks and ice, we show that mechanical anisotropy is a very effective additional mechanism. Self-similarity is a particular characteristic of this mechanism. This obviates the need to find individual mechanisms for strain localisation structures at different scales.

Acknowledgements

HR acknowledges financial support by the China Scholarship Council (CSC; grant nr. 201506400014). EGR acknowledges the support of the Beatriu de Pinós programme of the Government of Catalonia's Secretariat for Universities and Research of the Department of Economy and Knowledge (2016 BP 00208). M.-G.L acknowledges the support of the Juan de la Cierva programme of the Government of Spain's Ministry for Science, Innovation and Universities.

References

Arbaret, L., Burg, J.P., Zeilinger, G., Chaudhry, N., Hussain, S., Dawood, H., 2000. Pre-collisional anastomosing shear zones in the Kohistan arc, NW Pakistan. Geological Society, London, Special Publications, 170, 295-311.

Bak, J., Korstgård, J., Sørensen, K., 1975. A major shear zone within the Nagssugtoqidian of West Greenland. Tectonophysics, 27, 191-209.

Bak, P., Tang, C., Wiesenfeld, K., 1987. Self-organized criticality: An explanation of the 1/f noise. Physical review letters, 59, 381.

Behrmann, J.H., Mainprice, D., 1987. Deformation mechanisms in a high-temperature quartz-feldspar mylonite: evidence for superplastic flow in the lower continental crust. Tectonophysics, 140, 297-305.

Bell, T.H., 1981. Foliation development—the contribution, geometry and significance of progressive, bulk, inhomogeneous shortening. Tectonophysics, 75, 273-296.

Ben-Zion, Y., Sammis, C.G. 2003. Characterization of fault zones. Pure and Applied Geophysics, 160, 677-715.

Bercovici, D., 1993. A simple model of plate generation from mantle flow. Geophysical Journal International, 114, 635-650.

Berthé D., Choukroune, P., Jegouzo, P., 1979. Orthogneiss, mylonite and non-coaxial deformation of granites: the example from the South Armoricain shear zone. Journal of Structural Geology 1, 31-42.

Bird, P., 2003. An updated digital model of plate boundaries. Geochemistry, Geophysics, Geosystems, 4.

Bonnet, E., Bour, O., Odling, N.E., Davy, P., Main, I., Cowie, P., Berkowitz, B., 2001. Scaling of fracture systems in geological media. Reviews of geophysics, 39, 347-383.

Bons, P.D., Jessell, M.W., 1999. Micro-shear zones in experimentally deformed octachloropropane. Journal of Structural Geology, 21, 323-334.

Bons, P.D., van Milligen, B.P., 2001. New experiment to model self-organized critical transport and accumulation of melt and hydrocarbons from their source rocks. Geology, 29(10), 919-922.

Bons, P.D., Jessell, M.W., Evans, L., Barr, T., Stuwe, K., 2001. Modeling of anisotropic grain growth in minerals. Memoirs- Geological Society of America, 39-50.

Bons, P.D., Druguet, E., Hamann, I., Carreras, J., Passchier, C.W. 2004. Apparent boudinage in dykes. Journal of Structural Geology, 26, 625-636.

Bons, P.D., Koehn, D., Jessell, M.W., 2008. Microdynamics Simulation, Volume 106 of Lecture

Notes in Earth Sciences.

Bons, P.D., Jansen, D., Mundel, F., Bauer, C.C., Binder, T., Eisen, O., Jessell, M.W., Llorens, M.G., Steinbach, F., Steinhage, D., Weikusat, I., 2016. Converging flow and anisotropy cause large-scale folding in Greenland's ice sheet. Nature communications, 7, 11427.

Brown, M., Solar, G.S., 1998. Shear-zone systems and melts: feedback relations and self-organization in orogenic belts. Journal of Structural Geology, 20, 211-227.

Brun, J.P., Cobbold, P.R., 1980. Strain heating and thermal softening in continental shear zones: a review. Journal of Structural Geology, 2(1-2), 149-158.

Brunetti, M.T., Guzzetti, F., Rossi, M., 2009. Probability distributions of landslide volumes. Nonlinear Processes in Geophysics, 16, 179.

Carreras, J., 2001. Zooming on Northern Cap de Creus shear zones. Journal of Structural Geology, 23, 1457-1486.

Carreras, J., Druguet, E., Griera, A., Soldevila, J., 2004. Strain and deformation history in a syntectonic pluton. The case of the Roses granodiorite (Cap de Creus, Eastern Pyrenees). Geological Society, London, Special Publications, 224, 307-319.

Carreras, J., Czeck, D.M., Druguet, E., Hudleston, P.J., 2010. Structure and development of an anastomosing network of ductile shear zones. Journal of Structural Geology, 32, 656-666.

Cobbold, P., 1976. Mechanical effects of anisotropy during large finite deformations. Bulletin de la Soci ètè g èologique de France, 7, 1497-1510.

Cobbold, P.R., Cosgrove, J.W., Summers, J.M., 1971. Development of internal structures in deformed anisotropic rocks. Tectonophysics, 12, 23-53.

Cosgrove, J.W., 1976. The formation of crenulation cleavage. Journal of the Geological Society, 132, 155-178.

Cosgrove, J.W., 1997. The influence of mechanical anisotropy on the behaviour of the lower crust. Tectonophysics, 280, 1-14.

Dabrowski, M., Schmid, D.W., 2011. A rigid circular inclusion in an anisotropic host subject to simple shear. Journal of Structural Geology, 33(7), 1169-1177.

Davy, P., Hansen, A., Bonnet, E., Zhang, S.Z., 1995. Localization and fault growth in layered brittle‐ductile systems: Implications for deformations of the continental lithosphere. Journal of Geophysical Research: Solid Earth, 100, 6281-6294.

De Bresser, J.H.P., Peach, C.J., Reijs, J.P.J., Spiers, C.J., 1998. On dynamic recrystallization during solid state flow: Effects of stress and temperature. Geophysical Research Letters, 25, 3457-3460.

De Bresser, J., Ter Heege, J., Spiers, C., 2001. Grain size reduction by dynamic recrystallization:

can it result in major rheological weakening? International Journal of Earth Sciences, 90, 28-45.

Druguet, E., 2001. Development of high thermal gradients by coeval transpression and magmatism during the Variscan orogeny: insights from the Cap de Creus (Eastern Pyrenees). Tectonophysics, 332(1-2), 275-293.

Druguet, E., Hutton, D.H.W., 1998. Syntectonic anatexis and magmatism in a mid-crustal transpressional shear zone: an example from the Hercynian rocks of the eastern Pyrenees. Journal of Structural Geology, 20(7), 905-916.

Druguet, E., Passchier, C.W., Carreras, J., Victor, P., Den Brok, S., 1997. Analysis of a complex high-strain zone at Cap de Creus, Spain. Tectonophysics, 280, 31-45.

Duval, P., Ashby, M.F., Anderman, I., 1983. Rate-controlling processes in the creep of polycrystalline ice. The Journal of Physical Chemistry, 87, 4066-4074.

Finch, M.A., Weinberg, R.F., Hunter, N.J., 2016. Water loss and the origin of thick ultramylonites. Geology, 44, 599-602.

Fletcher, R.C., 2004. Anisotropic viscosity of a dispersion of aligned elliptical cylindrical clasts in viscous matrix. Journal of Structural Geology, 26, 1977-1987.

Fletcher, R.C., 2009. Deformable, rigid, and inviscid elliptical inclusions in a homogeneous incompressible anisotropic viscous fluid. Journal of Structural Geology, 31, 382-387.

Fossen, H., Cavalcante, G.C.G., 2017. Shear zones–A review. Earth-Science Reviews, 171, 434-455.

Fusseis, F., Handy, M.R., Schrank, C., 2006. Networking of shear zones at the brittle-to-viscous transition (Cap de Creus, NE Spain). Journal of Structural Geology, 28 1228-1243.

Gapais, D., Bale, P., Choukroune, P., Cobbold, P., Mahjoub, Y., Marquer, D., 1987. Bulk kinematics from shear zone patterns: some field examples. Journal of Structural Geology, 9, 635-646.

Gardner, R., Piazolo, S., Evans, L., Daczko, N., 2017. Patterns of strain localization in heterogeneous, polycrystalline rocks–a numerical perspective. Earth and Planetary Science Letters, 463, 253-265.

Gómez Rivas, E., 2008. Localización de deformación en medios dúctiles y anisótropos. Unpublished PhD-thesis, Universitat Autònoma de Barcelona.

Gomez-Rivas, E., Griera, A., 2011. Strain rate influence on fracture development in experimental ductile multilayers. Tectonophysics, 502, 351-363.

Gomez-Rivas, E., Griera, A., 2012. Shear fractures in anisotropic ductile materials: an experimental approach. Journal of Structural Geology, 34, 61-76.

Gomez-Rivas, E., Griera, A., Llorens, M.G., 2015. Fracturing of ductile anisotropic multilayers:

influence of material strength. Solid earth, 6(2), 497.

Gomez-Rivas, E., Griera, A., Llorens, M.G., Bons, P.D., Lebensohn, R.A., Piazolo, S., 2017. Subgrain Rotation Recrystallization During Shearing: Insights From Full-Field Numerical Simulations of Halite Polycrystals. Journal of Geophysical Research: Solid Earth, 122(11), 8810-8827.

Goncalves, P., Poilvet, J.-C., Oliot, E., Trap, P., Marquer, D., 2016. How does shear zone nucleate? An example from the Suretta nappe (Swiss Eastern Alps). J. Struct. Geol. 86, 166–180.

Griera, A., Bons, P.D., Jessell, M.W., Lebensohn, R.A., Evans, L., Gomez-Rivas, E., 2011. Strain localization and porphyroclast rotation. Geology, 39, 275-278.

Griera, A., Llorens, M.G., Gomez-Rivas, E., Bons, P.D., Jessell, M.W., Evans, L.A., Lebensohn, R., 2013. Numerical modelling of porphyroclast and porphyroblast rotation in anisotropic rocks. Tectonophysics, 587, 4-29.

Gutenberg, B., Richter, C.F., 1956. Earthquake magnitude, intensity, energy, and acceleration: (Second paper). Bulletin of the seismological society of America, 46, 105-145.

Hähner, P., 1996. On the foundations of stochastic dislocation dynamics. Applied Physics A, 62, 473-481.

Hähner, P., Bay, K., Zaiser, M., 1998. Fractal dislocation patterning during plastic deformation. Physical review letters, 81, 2470.

Handy, M.R., 1990. The solid-state flow of polymineralic rocks. Journal of Geophysical Research 95, 8647-8661.

Handy, M.R., Mulch, A., Rosenau, M., Rosenberg, C.L., 2001. The role of fault zones and melts as agents of weakening, hardening and differentiation of the continental crust: a synthesis. Geological Society, London, Special Publications, 186, 305-332.

Hanmer, S., Passchier, C.W., 1991. Shear sense indicators: a review. Geological Survey of Canada Paper 90, 1±71.

Herrmann, H.J., Poliakov, A.N., Tzschichholz, F., 1995. The deformation of rocks: fractals everywhere. Fractals, 3, 821-828.

Herwegh, M., Handy, M.R., 1996. The evolution of high-temperature mylonitic microfabrics: evidence from simple shearing of a quartz analogue (norcamphor). Journal of Structural Geology, 18, 689-710.

Hirth, G., Tullis, J., 1992. Dislocation creep regimes in quartz aggregates. Journal of Structural Geology, 14, 145-159.

Hippertt, J., 1999. Are S–C structures, duplexes and conjugate shear zones different manifestations of the same scale-invariant phenomenon?. Journal of Structural

Geology, 21, 975-984.

Hobbs, B.E., Ord, A., 1988. Plastic instabilities: implications for the origin of intermediate and deep focus earthquakes. Journal of Geophysical Research, 93, 10,521-10,540

Hobbs, B.E., Ord, A., Teyssier, C., 1986. Earthquakes in the ductile regime?. Pure and Applied Geophysics, 124, 309-336.

Hobbs, B.E., Mühlhaus, H.B., Ord, A., 1990. Instability, softening and localization of deformation. Geological Society, London, Special Publications, 54, 143-165.

Hudleston, P.J., 1999. Strain compatibility and shear zones: is there a problem?. Journal of Structural Geology, 21, 923-932.

Hudleston, P.J., Treagus, S.H., 2010. Information from folds: a review. Journal of Structural Geology, 32(12), 2042-2071.

Hull, J., 1988. Thickness-displacement relationships for deformation zones. Journal of Structural Geology, 10, 431-435.

Jansen, D., Llorens Verde, M.G., Westhoff, J., Steinbach, F., Kipfstuhl, S., Bons, P.D., Griera, A., Weikusat, I., 2016. Small-scale disturbances in the stratigraphy of the NEEM ice core: observations and numerical model simulations. The Cryosphere, 10, 359-370.

Jessell, M.W., Bons, P.D., Evans, L., Barr, T., Stüwe, K., 2001. Elle: the numerical simulation of metamorphic and deformation microstructures. Computers & Geosciences, 27, 17-30.

Ji, S., Jiang, Z., Rybacki, E., Wirth, R., Prior, D., Xia, B., 2004. Strain softening and microstructural evolution of anorthite aggregates and quartz–anorthite layered composites deformed in torsion. Earth and Planetary Science Letters, 222, 377-390.

Johnson, S.E., Vernon, R.H., Upton, P., 2004. Foliation development and progressive strain-rate partitioning in the crystallizing carapace of a tonalite pluton: microstructural evidence and numerical modeling. Journal of Structural Geology, 26, 1845-1865.

Jordan, P., 1988. The rheology of polymineralic rocks - an approach. Geologische Rundschau, 77, 285-294.

Kocher, T., Schmalholz, S.M., Mancktelow, N.S., 2006. Impact of mechanical anisotropy and power-law rheology on single layer folding. Tectonophysics, 421(1-2), 71-87.

Kocher, T., Mancktelow, N.S., Schmalholz, S.M., 2008. Numerical modelling of the effect of matrix anisotropy orientation on single layer fold development. Journal of Structural Geology, 30(8), 1013-1023.

Latham, J.P., 1979. Experimentally developed folds in a material with a plannar mineral fabric. Tectonophysics, 57, T1-T8.

Lebensohn, R.A., 2001. N-site modeling of a 3D viscoplastic polycrystal using fast Fourier

transform. Acta Materialia, 49, 2723-2737.

Lebensohn, R.A., Brenner, R., Castelnau, O., Rollett, A.D., 2008. Orientation image-based micromechanical modelling of subgrain texture evolution in polycrystalline copper. Acta Materialia, 56, 3914-3926.

Lebensohn, R.A., Montagnat, M., Mansuy, P., Duval, P., Meysonnier, J., Philip, A., 2009. Modeling viscoplastic behavior and heterogeneous intracrystalline deformation of columnar ice polycrystals. Acta Materialia, 57(5), 1405-1415.

Llorens, M.G., Bons, P.D., Griera, A., Gomez-Rivas, E., Evans, L.A., 2013a. Single layer folding in simple shear. Journal of Structural Geology, 50, 209-220.

Llorens, M.G., Bons, P.D., Griera, A., Gomez-Rivas, E., 2013b. When do folds unfold during progressive shear? Geology, 41, 563-566.

Llorens, M.G., Griera, A., Bons, P.D., Roessiger, J., Lebensohn, R., Evans, L., Weikusat, I., 2016a. Dynamic recrystallisation of ice aggregates during co-axial viscoplastic deformation: a numerical approach. Journal of Glaciology, 62, 359-377.

Llorens, M.G., Griera, A., Bons, P.D., Lebensohn, R.A., Evans, L.A., Jansen, D., Weikusat, I., 2016b. Full-field predictions of ice dynamic recrystallisation under simple shear conditions. Earth and Planetary Science Letters, 450, 233-242.

Llorens, M.G., Griera, A., Steinbach, F., Bons, P.D., Gomez-Rivas, E., Jansen, D.,Weikusat, I., 2017. Dynamic recrystallization during deformation of polycrystalline ice: insights from numerical simulations. Phil. Trans. R. Soc. A, 375 20150346.

Mainprice, D., Nicolas, A., 1989. Development of shape and lattice preferred orientations: application to the seismic anisotropy of the lower crust. Journal of Structural Geology, 11(1-2), 175-189.

Mainprice, D., Bouchez, J.L., Blumenfeld, P., Tubià, J.M., 1986. Dominant c slip in naturally deformed quartz: implications for dramatic plastic softening at high temperature. Geology, 14(10), 819-822.

Mancktelow, N.S., Pennacchioni, G., 2004. The influence of grain boundary fluids on the microstructure of quartz-feldspar mylonites. Journal of Structural Geology, 26, 47-69.

Mandelbrot, B.B., 2001. Scaling in financial prices: I. Tails and dependence. Quantitative Finance. Volume 1 - Issue 1

Mandelbrot, B.B., Fisher, A., Calvet, L., 1997. A multifractal model of asset returns.

Means, W.D., 1984. Shear zones of types I and II and their significance for reconstruction of rock history. Geol. Soc. Am. Bull. Abstract Programs, 16, 50.

Menegon, L., Pennacchioni, G., Spiess, R., 2008. Dissolution-precipitation creep of K-feldspar in mid-crustal granite mylonites. Journal of Structural Geology, 30(5), 565-579.

Meyer, S.E., Kaus, B., Passchier, C., 2017. Development of branching brittle and ductile shear zones: A numerical study. Geochemistry, Geophysics, Geosystems.

Michibayashi, K., Mainprice, D., 2004. The role of pre-existing mechanical anisotropy on shear zone development within oceanic mantle lithosphere: an example from the Oman ophiolite. Journal of Petrology, 45(2), 405-414.

Mitra, G., 1979. Ductile deformation zones in Blue Ridge basement rocks and estimation of finite strains. Geological Society of America Bulletin, 90, 935-951.

Mitzenmacher, M., 2004. A brief history of generative models for power law and lognormal distributions. Internet mathematics, 1, 226-251.

Montagnat, M., Castelnau, O., Bons, P.D., Faria, S.H., Gagliardini, O., Gillet-Chaulet, F., Roessiger, J., 2014. Multiscale modeling of ice deformation behavior. Journal of Structural Geology, 61, 78-108.

Mühlhaus, H.B., Dufour, F., Moresi, L., Hobbs, B., 2002. A director theory for visco-elastic folding instabilities in multilayered rock. International Journal of Solids and Structures, 39, 3675-3691.

Oliot, E., Goncalves, P., Schulmann, K., Marquer, D., Lexa, O., 2014. Mid-crustal shear zone formation in granitic rocks: constraints from quantitative textural and crystallographic preferred orientations analyses. Tectonophysics, 612, 63-80.

Ord, A., Hobbs, B., 2018. Quantitative measures of deformed rocks: The links to dynamics. Journal of Structural Geology.

Passchier, C.W., 1984. The generation of ductile and brittle shear bands in a low-angle mylonite zone. Journal of Structural Geology, 6, 273-281.

Passchier, C.W., Trouw, R.A., 2005. Microtectonics. Springer Science & Business Media.

Pennacchioni, G., Mancktelow, N.S., 2007. Nucleation and initial growth of a shear zone network within compositionally and structurally heterogeneous granitoids under amphibolite facies conditions. J. Struct. Geol. 29, 1757–1780.

Platt, J.P., Behr, W.M., 2011. Grain size evolution in ductile shear zones: Implications for strain localization and the strength of the lithosphere. Journal of Structural Geology, 33, 537-550.

Platt, J.P., Behrmann, J.H., 1986. Structures and fabrics in a crustal-scale shear zone, Betic Cordillera, SE Spain. Journal of Structural Geology, 8, 15-33.

Poliakov, A.N.B., Herrmann, H.J., 1994. Self-organized criticality of plastic shear bands in rocks. Geophysical Research Letters, 21, 2143-2146.

Poliakov, A.N., Herrmann, H.J., Podladchikov, Y.Y., Roux, S., 1994. Fractal plastic shear bands. Fractals, 2, 567-581.

Poirier, J.P., 1980. Shear localization and shear instability in materials in the ductile field. Journal of Structural Geology, 2, 135-142.

Ponce, C., Druguet, E., Carreras, J., 2013. Development of shear zone-related lozenges in foliated rocks. Journal of Structural Geology, 50, 176-186.

Ran, H., de Riese, T., Llorens, M.G., Finch, M.A., Evans, L.A., Gomez-Rivas, E., Griera, A., Jessell, M.W., Lebensohn, R.A., Piazolo, S., Bons, P. D., 2018. Time for anisotropy: The significance of mechanical anisotropy for the development of deformation structures. Journal of Structural Geology.

Ramsay, J.G., Allison, I., 1979. Structural analysis of shear zones in an alpinised Hercynian granite (Maggia Lappen, Pennine Zone, Central Alps). Schweizerische mineralogische und petrographische Mitteilungen, 59, 251-279.

Regenauer-Lieb, K., Hobbs, B., Ord, A., Gaede, O., Vernon, R., 2009. Deformation with coupled chemical diffusion. Physics of the Earth and Planetary Interiors, 172, 43-54.

Rosenberg, C.L., Handy, M.R., 2000. Syntectonic melt pathways during simple shearing of a partially molten rock analogue (Norcamphor Benzamide). Journal of Geophysical Research: Solid Earth, 105, 3135-3149.

Sammis, C.G., Steacy, S.J., 1995. Fractal fragmentation in crustal shear zones. In Fractals in the Earth Sciences (pp. 179-204). Springer, Boston, MA.

Schrank, C. E., Handy, M. R., Fusseis, F., 2008. Multiscaling of shear zones and the evolution of the brittle-to-viscous transition in continental crust. Journal of Geophysical Research: Solid Earth, 113(B1).

Segall, P., Simpson, C., 1986. Nucleation of ductile shear zones on dilatant fractures. Geology, 14, 56–59.

Shea, W.T., Kronenberg, A.K. 1993. Strength and anisotropy of foliated rocks with varied mica contents. Journal of Structural Geology, 15, 1097-112.

Shimizu, I., 2008. Theories and applicability of grain size piezometers: The role of dynamic recrystallization mechanisms. Journal of Structural Geology, 30, 899-917.

Sørensen, K., 1983. Growth and dynamics of the Nordre Strømfjord shear zone. Journal of Geophysical Research: Solid Earth, 88, 3419-3437.

Sornette, D., Pisarenko, V., 2003. Fractal plate tectonics. Geophysical research letters, 30(3).

Sornette, A., Davy, P., Sornette, D., 1993. Fault growth in brittle-ductile experiments and the mechanics of continental collisions. Journal of Geophysical Research: Solid Earth, 98, 12111-12139.

Steinbach, F., Bons, P.D., Griera, A., Jansen, D., Llorens Verde, M.G., Roessiger, J.,Weikusat, I., 2016. Strain localization and dynamic recrystallization in the ice–air aggregate: a

numerical study. The Cryosphere, 10, 3071-3089.

Steinbach, F., Kuiper, E.J.N., Eichler, J., Bons, P.D., Drury, M.R., Griera, A., Pennock, G.M., Weikusat, I., 2017. The Relevance of Grain Dissection for Grain Size Reduction in Polar Ice: Insights from Numerical Models and Ice Core Microstructure Analysis. Frontiers in Earth Science, 5, 66.

Stipp, M., Stünitz, H., Heilbronner, R., Schmid, S.M., 2002. The eastern Tonale fault zone: a 'natural laboratory' for crystal plastic deformation of quartz over a temperature range from 250 to 700 C. Journal of Structural Geology, 24(12), 1861-1884.

Tchalenko, J. S., 1970. Similarities between shear zones of different magnitudes. Geological Society of America Bulletin, 81, 1625-1640.

Thielmann, M., 2017. Grain size assisted thermal runaway as a nucleation mechanism for continental mantle earthquakes: Impact of complex rheologies. Tectonophysics.

Thielmann, M., Kaus, B.J., 2012. Shear heating induced lithospheric-scale localization: Does it result in subduction?. Earth and Planetary Science Letters, 359, 1-13.

Thielmann, M., Rozel, A., Kaus, B.J.P., Ricard, Y., 2015. Intermediate-depth earthquake generation and shear zone formation caused by grain size reduction and shear heating. Geology, 43, 791-794.

Toimil, N.C., Griera, A., 2007. Influence of viscosity contrast and anisotropy on strain accommodation in competent layers. Journal of structural geology, 29(5), 787-801.

Tommasi, A., Knoll, M., Vauchez, A., Signorelli, J. W., Thoraval, C., Logé, R., 2009. Structural reactivation in plate tectonics controlled by olivine crystal anisotropy. Nature Geoscience, 2, 423.

Tullis, J., Yund, R. A., 1985. Dynamic recrystallization of feldspar: A mechanism for ductile shear zone formation. Geology, 13, 238-241.

Turcotte, D.L., 1990. Implications of chaos, scale-invariance, and fractal statistics in geology. Palaeogeography, Palaeoclimatology, Palaeoecology, 89, 301-308.

Turcotte, D.L., 1992. Fractals, chaos, self-organized criticality and tectonics. Terra Nova, 4, 4-12.

Turcotte, D.L., 1997. Fractals and chaos in geology and geophysics. Cambridge university press.

Urai, J.L., 1983. Water assisted dynamic recrystallization and weakening in polycrystalline bischofite. Tectonophysics, 96(1-2), 125-157.

Warren, J.M., Hirth, G., 2006. Grain size sensitive deformation mechanisms in naturally deformed peridotites. Earth and Planetary Science Letters, 248, 438-450.

Warren, J.M., Hirth, G., Kelemen, P.B., 2008. Evolution of olivine lattice preferred orientation

during simple shear in the mantle. Earth and Planetary Science Letters, 272(3-4), 501-512.

White, S.T., Knipe, R.J., 1978. Transformation-and reaction-enhanced ductility in rocks. Journal of the Geological Society, 135, 513-516.

White, S.H., Burrows, S.E., Carreras, J., Shaw, N. D., Humphreys, F.J., 1980. On mylonites in ductile shear zones. Journal of Structural Geology, 2, 175-187.

Zaiser, M., Bay, K., Hähner, P., 1999. Fractal analysis of deformation-induced dislocation patterns. Acta materialia, 47, 2463-2476.

Appendix

Numerical model setup

Descriptions of files used in model and detailed settings of numerical models in this thesis are presented here. There are two kinds of files required for simulation: initial ELLE file (*.elle*) and VPFFT files (*.sx* and *.in*). Initial ELLE file is used to define the initial structures.

1. The phase file (*.sx*)

It defines the phase properties including critical resolved shear stress (CRSS) and stress exponent (*n*) of each slip system.

```
SLIP SYSTEMS FOR ICE
HEX                icryst
   1.  1.  1.629   crystal axes (cdim(i))
   3               nmodesx (total # of modes listed in the file)
   3               nmodes  (# of modes to be used in the calculation)
   1  2  3         mode(i) (label of the modes to be used)
   BASAL SLIP
  1   3   3   1.0   0.0  0            modex,nsmx,nrsx,gamd0x,twshx,isectwx
  1.0   1.0   0.0   0.0  0.0           tau0xf,tau0xb,tau1x,thet0,thet1
  1.0   1.0   0.0   0.0               hselfx,hlatex
   0  0  0  1    1  1 -2  0
   0  0  0  1    1 -2  1  0
   0  0  0  1   -2  1  1  0
   PRISMATIC SLIP
  2   3   3   1.0   0.0  0           modex,nsmx,nrsx,gamd0x,twshx,isectwx
  1.0   1.0   0.0   0.0  0.0          tau0xf,tau0xb,tau1x,thet0,thet1
  1.0   1.0   0.0   0.0              hselfx,hlatex
   0  1 -1  0    2 -1 -1  0
   1  0 -1  0   -1  2 -1  0
   1 -1  0  0    1  1 -2  0
   PYRAMIDAL SLIP
  3   6   3   1.0   0.0   0          modex,nsmx,nrsx,gamd0x,twshx,isectwx
  1.0   1.0   0.0   0.0  0.0          tau0xf,tau0xb,tau1x,thet0,thet1
  1.0   1.0   0.0   0.0              hselfx,hlatex
   1  1 -2  2    1  1 -2 -3
  -1 -1  2  2   -1 -1  2 -3
   2 -1 -1  2    2 -1 -1 -3
  -2  1  1  2   -2  1  1 -3
   1 -2  1  2    1 -2  1 -3
  -1  2 -1  2   -1  2 -1 -3
```

Numbers in red circles define the stress exponent (*n*) of each slip plane. *n*=1 or 3 is used to simulate linear or power-law rheology in the thesis. Same *n* is set to all slip planes for single phase. Numbers in blue circle define the CRSS of each slip plane, i.e. viscosity. Two numbers are same in each plane. Mechanical anisotropy is defined by different CRSS on slip planes.

2. The *ppc.in* file

It defines amount of phases and *unodes* and boundary conditions.

```
3                          number of phases (nph)
0.7  0.2  0.1                  relative vol. fract. of phases (wph(i)) -- NOT USE
*INFORMATION ABOUT PHASE #1
65536                    number of grains to read in filetext  Amount of unodes
* name and path of texture file (filetext)
make.out
* name and path of single crystal file (filecrys)
phase1.sx
1.0       FACT_BOUND factor of CRSS for special fourier points
*INFORMATION ABOUT PHASE #2
65536                     number of grains to read in filetext
* name and path of texture file (filetext)
make.out
* name and path of single crystal file (filecrys)
phase2.sx
1.0       FACT_BOUND factor of CRSS for special fourier points
*INFORMATION ABOUT PHASE #3
65536                     number of grains to read in filetext
* name and path of texture file (filetext)
make.out
* name and path of single crystal file (filecrys)
phase3.sx
1.0       FACT_BOUND factor of CRSS for special fourier points
*INFORMATION ABOUT TEST CONDITIONS
1.  1.  1.                    RVE dimensions (delt)
* boundary conditions
    1       1       1           iudot     |    flag for vel.grad.
    1       1       1                     |    (0:unknown-1:known)
    1       1       1                     |
                                  |
    0.     2e-12    0.          udot      |    vel.grad
    0.      0.      0.                    |
    0.      0.      0.                    |
                                  |
    0       0       0           iscau     |    flag for Cauchy
            0       0                     |
                    0                     |
                                  |
    0.      0.      0.          scauchy   |    Cauchy stress
            0.      0.                    |
                    0.                  @
* other
1e10      eqincr (if ictrl>=0) or tdot (if ictrl=-1)
-1              ictrl (1-6: strain comp, 0: VM eq, -1: tdot)
*INFORMATION ABOUT RUN CONDITIONS
1             nsteps
0.000000001    err
400            itmax
0              IRECOVER read grain states from STRESS.IN  (1) or not (0)?
1.0  99.0      xlfac0 (dum if irecover=1),xlfac1 (dum if irecover=0)
0              ISAVE write grain states in  STRESS.OUT (1) or not (0)?
0              IWRITEG write G*.OUT files (1) or not (0)
1              IUPDATE update tex & RVE dim and write TEX.OUT (1) or not
*additional parameters to estimate dislocation
0.01            length scale, keep the same than in Elle file
4.5e-10         burgers vector length
```

Amount of phases
Two or three numbers for two or three phases, their sum should be 1

Velocity gradient used for top-to-right simple shear in power-law (*n*=3) rheology

```
0.      2e-7    0.
0.      0.      0.
0.      0.      0.
```

For top-to-right simple shear in linear (*n*=1) rheology

```
5e-11   0.      0.
0.      -5e-11  0.
0.      0.      0.
```

For vertical shortening in power-law (*n*=3) rheology

Time for single step used for simple shear in power-law (*n*=3) rheology

1e5 For single step used for simple shear in linear (*n*=1) rheology

2e8 For vertical shortening in power-law (*n*=3) rheology

More details of settings for models are presented in each chapter. More details of Preparations and post-processes of simulations follow descriptions of Steinbach (2017).

Reference

Steinbach F., 2017. Numerical modelling of deformation and recrystallisation mechanics in ice and ice-air aggregates. Unpublished Ph.D. thesis, Eberhard Karls University Tübingen.